School of Physics
and Astronomy

Waveform Modelling for Gravitational Wave Astrophysics

Panagiota Kolitsidou

A thesis submitted for the degree of
Doctor of Philosophy

June 2023

Summary of thesis

The advancing sensitivity of gravitational wave detectors not only broadens our knowledge of the universe but also calls for the refinement of the waveform models. The focus of this thesis is the study of the impact that the absence of the multipole asymmetry from the waveform models has on the measured binary black hole parameters and the development of more accurate `Phenom` waveform models by modelling this missing physics.

We conduct a systematics study to investigate the impact of the absence of this asymmetry using two versions of `NRSur7dq4` [1], the original `NRSur7dq4` and a "symmetric" `NRSur7dq4`, where the asymmetry is removed. Moreover, we show how the introduced biases are affected by the recoil velocity and other parameters. We also consider the highly precessing GW200129 signal [2, 3]. This study shows that the absence of the multipole asymmetry from the waveform models leads to significant biases in the spin measurements in the case of strongly precessing systems with high signal-to-noise ratio (SNR).

Based on these results, the inclusion of the multipole asymmetry in the waveform models will be essential for the correct measurement of these parameters in the next observational runs when we expect to observe similar to these events. Therefore, we developed the first phenomenological multipole asymmetry model. Our model is implemented into `PhenomPNR` [4] and will be available in $O4$. The amplitude and the phase of the asymmetry are modelled in the frequency-domain co-precessing frame. To model the amplitude, we use post-Newtonian (PN) expressions to compute a ratio of the anti-symmetric amplitude over the symmetric amplitude. This PN ratio is our starting point for the modelling of the corresponding numerical relativity ratio. The asymmetry amplitude model is obtained by multiplying this ratio model with one of the existing symmetrized waveform models. To model the phase, we construct the asymmetry phase derivative using the phase derivative of the symmetric phase and the derivative of the precession angle, α. During the inspiral, the asymmetry phase derivative is equivalent to the sum of these terms while closer to the merger it becomes equal to the derivative of the symmetric phase.

Collaborative work

Parts of this thesis are the result of collaborative work.

- In Chapter 2, we introduce the BAM catalogue that consists of 80 numerical relativity simulations that are used to tune the multipole asymmetry model. The catalogue was developed by members of the Cardiff waveform group including myself. This work has been published in [5]. I contributed to the development of 6 of these simulations and I have also developed 4 additional double-spin simulations using the BAM code, which are not included in this catalogue.

- Chapter 3 presents collaborative work with Mark Hannam and Jonathan Thompson. Jonathan Thompson created the symmetric version of the surrogate, assisted me when I was setting up the runs and provided the "de-glitched" data. I conducted the parameter estimation analysis and additional preparations described in the chapter. A publication based on this work is currently in preparation.

- Chapter 4 presents collaborative work with Shrobana Ghosh and Mark Hannam. From the work presented in this chapter, I was responsible for the development of the anti-symmetric amplitude model and Shrobana Ghosh developed the model of the anti-symmetric phase. Therefore, this chapter focuses on the work I did for the development of the amplitude model providing only a brief overview of the phase model. A publication based on this work is currently in preparation.

Acknowledgements

I would like to thank my supervisor, Mark, for giving me the opportunity to work on such an amazing topic, for his support throughout my PhD and his encouragement during these last months when I was writing my thesis. I would also like to thank all the people I was lucky to work with for their support, guidance, and always being willing to listen and answer my questions. I am also grateful to all the outstanding PhD students and postdocs I met during my PhD, who made many days more joyful and entertaining with exciting discussions and by sharing laughs.

I am deeply grateful to all the amazing people in my life who have contributed to this journey. I want to express my deepest appreciation to my mum, Stella, for her invaluable support and encouragement. Thank you for always being just a phone call away. I would also like to thank my partner Aris. Your support has sustained me through the highs and lows of this endeavour. Thank you for being my best friend. Lastly, I want to acknowledge my friends back home for all the joy and support I have received from them over the years, as well as the amazing friends I was very lucky to make while being in Cardiff and in Durham whose friendship, kindness, and encouragement have made this journey richer.

To all those mentioned and those not mentioned, thank you from the bottom of my heart for being part of this journey.

Contents

List of Figures

List of Tables

Chapter 1

Introduction

The LIGO-Virgo-KAGRA collaboration has made more than 90 observations since the first gravitational wave detection in 2015 [10, 11, 12, 13, 9]. The majority of these detections have been binary black holes and we expect this to continue to be the case during the next observing runs. The continuous improvement of the gravitational wave detectors enhances their sensitivity. As a result, in the future, we expect to detect a wider range of signals from a variety of binary black hole systems that can provide new insights into the nature of these compact objects.

Following the detection of the first strongly precessing system [3, 2] in $O3$, the detection of more precessing systems is anticipated in the upcoming $O4$ observing run. The improved sensitivity of the detector will also allow the detection of signals with stronger SNR. Therefore, we expect it to become more common that we can measure precession and the individual spins of the black holes.

However, the significance of these detections would be diminished without accurate waveform models. The waveform models are an essential tool that extracts valuable information from the detected signals about the nature of their sources. Thus, it is vital to ensure the accuracy of these models. In the next observing runs, due to the detection of louder precessing signals, systematic errors associated with these models will pose a new obstacle.

The modelling of the binary black hole systems is a challenging task and several approximations are employed to simplify the process of constructing the models, or to reduce the number and accuracy of the numerical relativity (NR) waveforms that must be used. One such approximation is the assumption that the gravitational wave energy is emitted symmetrically above and below the

orbital plane even in systems where this symmetry is broken by the precession of the orbital plane.

The main focus of this thesis is the study of the impact that the absence of the multipole asymmetry from the waveform models has on the measured binary black hole parameters and the development of more accurate `Phenom` waveform models by modelling this missing physics. In Chapter 2, we provide a basic description of the concepts relevant to this thesis that set the stage for the next chapters. In Chapter 3, we present the results of an extended systematics study that we performed using the `NRSur7dq4` model to investigate the effects that the absence of the multipole asymmetry has on the measurement of the source parameters. In Chapter 4, we present the first phenomenological model of multipole asymmetry. The main outcomes of this work and possible future directions are discussed in Chapter 5.

Chapter 2

Setting the stage: The fundamentals of gravitational wave astronomy

2.1 An introduction to general relativity

The theory of general relativity that was developed by Albert Einstein [14, 15], transformed our perception of gravity and spacetime. In this theory, gravity is described as the outcome of the curvature of spacetime caused by the presence of mass and energy. Here we will provide a brief description of the most important equations of general relativity to help the reader navigate the upcoming sections. For an in-depth description of the theory, we refer the reader to the textbooks [16, 17].

The spacetime is a 4-dimensional differentiable manifold M equipped with a Lorenzian metric g. The metric specifies the geometry and causal structure of spacetime. As a result, it is used to determine the line element

$$ds^2 = g_{\alpha\beta} dx^\alpha dx^\beta \tag{2.1}$$

that denotes the distance between two points on M. In general relativity, the concept of a straight line is extended to accommodate the curvature. In a curved spacetime, freely moving or falling particles move always along geodesics which are paths that extremise the proper time. The geodesic equa-

tions can be expressed mathematically as

$$\frac{d^2x^\alpha}{d\tau^2} = -\Gamma^\alpha_{\beta\gamma}\frac{dx^\beta}{d\tau}\frac{dx^\gamma}{d\tau}. \tag{2.2}$$

The Christoffel symbols $\Gamma^\alpha_{\beta\gamma}$ represent the connection coefficients in a curved spacetime and are defined in terms of the metric as

$$g_{\alpha\delta}\Gamma^\delta_{\beta\gamma} = \frac{1}{2}\left(\frac{\partial g_{\alpha\beta}}{\partial x^\gamma} + \frac{\partial g_{\alpha\gamma}}{\partial x^\beta} - \frac{\partial g_{\beta\gamma}}{\partial x^\alpha}\right). \tag{2.3}$$

The curvature of the spacetime is denoted by the Riemann tensor that encodes the failure of initially parallel geodesics to remain parallel due to the curvature of spacetime and is defined as

$$R^\alpha_{\beta\gamma\delta} = \frac{\partial\Gamma^\alpha_{\beta\delta}}{\partial x^\gamma} - \frac{\partial\Gamma^\alpha_{\beta\gamma}}{\partial x^\delta} + \Gamma^\alpha_{\gamma\epsilon}\Gamma^\epsilon_{\beta\delta} - \Gamma^\alpha_{\delta\epsilon}\Gamma^\epsilon_{\beta\gamma}. \tag{2.4}$$

The relationship between the curvature of spacetime and the distribution of matter is described by the Einstein field equations or Einstein's equations

$$G_{\alpha\beta} = 8\pi G T_{\alpha\beta}. \tag{2.5}$$

In Eq. 2.5 $T_{\alpha\beta}$ is the stress-energy tensor representing the source of curvature and $G_{\alpha\beta}$ is the Einstein tensor defined as

$$G_{\alpha\beta} = R_{\alpha\beta} - \frac{1}{2}g_{\alpha\beta}R, \tag{2.6}$$

where $R_{\alpha\beta}$ is the Ricci tensor or Ricci curvature defined as $R_{\alpha\beta} \equiv R^\gamma_{\alpha\gamma\beta}$ and R is the scalar curvature defined as the trace of the Ricci tensor $R = g^{\alpha\beta}R_{\alpha\beta}$. From its definition and Eq. 2.4, the Ricci curvature can be expressed in terms of the Christoffel symbols as

$$R_{\alpha\beta} = \frac{\partial\Gamma^\gamma_{\alpha\beta}}{\partial x^\gamma} - \frac{\partial\Gamma^\gamma_{\alpha\gamma}}{\partial x^\beta} + \Gamma^\gamma_{\alpha\beta}\Gamma^\delta_{\gamma\delta} - \Gamma^\gamma_{\alpha\delta}\Gamma^\delta_{\beta\gamma}. \tag{2.7}$$

The Einstein field equations consist of ten coupled, non-linear, 2nd-order partial differential equations. We note that in the study of general relativity, it is common practice the use of geometrized units where the gravitational constant, G, and the speed of light, c, are set to unity ($c = G = 1$). In this thesis, we employ geometrized units by default, with explicit inclusion of con-

stants when necessary for clarity. Having discussed some of the fundamental concepts of general relativity, we can now shift our focus to acquire a deeper understanding of gravitational waves.

2.2 Gravitational waves

The existence of gravitational waves was predicted by Albert Einstein, who first introduced them in his theory of general relativity in 1916 [14, 15]. A fundamental principle arising from general relativity is that mass causes the curvature of spacetime. Accelerated matter creates ripples in the curvature of spacetime, which we refer to as gravitational waves. These waves propagate outward, extending in all directions at the speed of light. Although gravitational waves carry significant amounts of energy away from a radiating system, their detection posed a significant challenge due to the inherent weakness of gravitational interaction.

The first indirect evidence for the existence of gravitational waves was observed by Hulse and Taylor in 1974 [18]. They monitored a binary system composed of a neutron star and a pulsar—a rapidly rotating neutron star with high magnetization that emits beams of electromagnetic radiation from its magnetic poles. Similar to black holes and white dwarfs, depending on the mass of the star, neutron stars are a type of stellar remnants formed after a massive star exhausts its nuclear fuel and undergoes gravitational collapse. In the context of general relativity, we refer to this type of binary systems as *compact* binary systems. Compact objects are stellar remnants characterised by high mass density and strong gravitational fields such as neutron stars, black holes and white dwarfs and their study is crucial in understanding and testing the predictions of general relativity. For a more in-depth discussion of stellar evolution and stellar remnants, the reader is encouraged to consult Ref. [19].

Hulse and Taylor observed that the orbital period of the binary system was decreasing in the rate that was predicted by the general theory of relativity [14, 15, 20]. The theory of general relativity asserts that in compact binary systems there is a loss of gravitational binding energy through gravitational wave emission leading to a gradual reduction in their orbital separation. Due to this orbital decay, the orbital period of the system is expected to change over time. Fig. 2.1 shows the remarkable agreement between the observed data

and the theoretical predictions of general relativity. This observation verified the emission of gravitational waves by the binary.

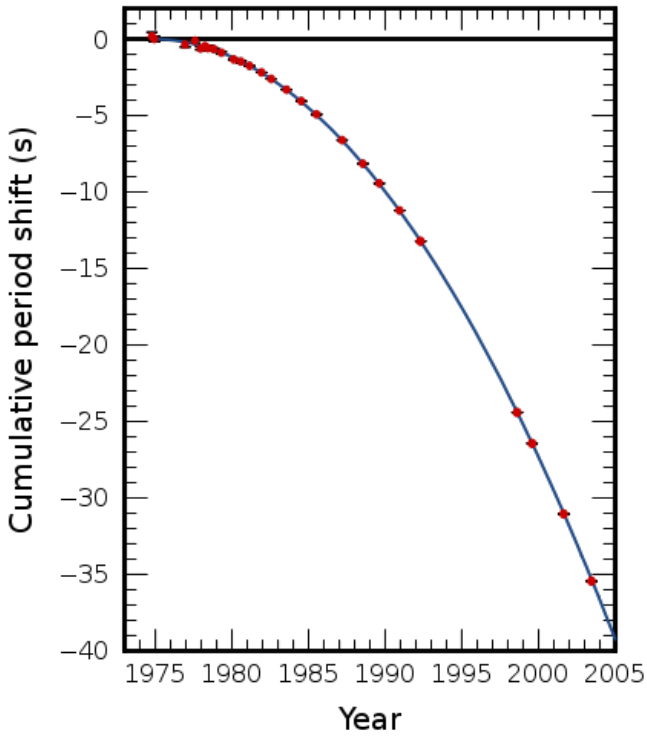

Figure 2.1: Orbital decay of the Hulse-Taylor binary PSR B1913+16. The observed data (red) perfectly match the theoretical curve (blue) predicted by general relativity. The image was taken from [6].

The first direct detection of gravitational waves took place many years later on September 14, 2015 [21]. This was the result of decades of work to construct highly sensitive detectors by a global scientific collaboration. The LIGO-Virgo collaboration detected for the first time, a gravitational wave signal, GW150914, generated from the merging of a binary black hole system [21]. This detection was followed by many more in the following years and marked the dawn of a new era in gravitational wave astronomy. The detection of gravitational waves offers us the unique opportunity to measure the properties of their sources and gain new valuable insights into these objects.

2.2.1 Linearised gravity

Linearised gravity serves as a useful tool for gaining insight into gravitational waves and studying their propagation and their effects on test particles. The

linearised approximation can be applied to weak gravitational fields and small perturbations on a flat spacetime significantly simplifying the solution of the Einstein equations. As a result, this is an excellent approximation for the study of gravitational waves originating from distant sources that reach Earth as subtle disturbances in the spacetime.

Assuming that the effects of gravity are small enough that they can be treated as a small deviation from a flat Minkowski spacetime, we can introduce weak metric perturbations $|h_{\alpha\beta}| \ll 1$ to the flat spacetime metric $g_{\alpha\beta} = \eta_{\alpha\beta}$. Introducing these metric perturbations, if δ denotes the linear perturbation of a quantity, then $h_{\alpha\beta} \equiv \delta g_{\alpha\beta}$ and the metric takes the form

$$g_{\alpha\beta} = \eta_{\alpha\beta} + h_{\alpha\beta} \tag{2.8}$$

where $\eta_{\alpha\beta} = diag(-1, 1, 1, 1)$ is the Minkowski metric and $h_{\alpha\beta}$ are weak perturbations.

Assuming that $T_{\alpha\beta} \neq 0$ and that the curvature produced by $T_{\alpha\beta}$ is weak enough for the linearised approximation to hold, we introduce the *trace-reversed* amplitude

$$\bar{h}_{\alpha\beta} = h_{\alpha\beta} - \frac{1}{2}\eta_{\alpha\beta}h. \tag{2.9}$$

If we then define the Lorenz gauge condition

$$\bar{h}^{\alpha\beta}_{,\beta} = 0, \tag{2.10}$$

we can use it to simplify Eq. 2.5. The linearised field equations for weak sources can then be rewritten as

$$\Box\bar{h}_{\alpha\beta} = -16\pi G T_{\alpha\beta} \tag{2.11}$$

where $\Box$ is the d'Alembertian operator. From Eq. 2.5, we note that in this gauge the linearised Einstein equations become wave equations for each component of $\bar{h}_{\alpha\beta}$.

To unravel the attributes of the gravitational waves, we will study the solution of the Einstein equations outside the source. In vacuum, $T_{\alpha\beta} = 0$ and the Einstein equations given in Eq. 2.5 take the form $R_{\alpha\beta} = 0$. Substituting Eq. 2.8 in $R_{\alpha\beta} = 0$ we can obtain the linearized vacuum Einstein equations

$$\delta R_{\alpha\beta} = 0 \tag{2.12}$$

Expressing the Ricci tensor in terms of the Christoffel symbols the linearised Einstein equations in vacuum become

$$\delta R_{\alpha\beta} = \frac{1}{2}\left[-\Box h_{\alpha\beta} + V_{\beta,\alpha} + V_{\alpha,\beta}\right] = 0 \tag{2.13}$$

where

$$V_\alpha = h^\gamma_{\alpha,\gamma} - \frac{1}{2}h^\gamma_{\gamma,\alpha}. \tag{2.14}$$

If we then introduce the Lorenz gauge condition

$$V_\alpha = h^\gamma_{\alpha,\gamma} - \frac{1}{2}h^\gamma_{\gamma,\alpha} = 0 \tag{2.15}$$

we can simplify Eq. 2.13 significantly and the latter becomes

$$\delta R_{\alpha\beta} = -\frac{1}{2}\Box h_{\alpha\beta} \tag{2.16}$$

Then, by substituting Eq. 2.12, Eq. 2.16 takes the form of the wave equation

$$\Box h_{\alpha\beta} = 0. \tag{2.17}$$

The general solution of Eq. 2.17 is the plane-wave solution

$$h_{\alpha\beta} = \alpha_{\alpha\beta} e^{i\eta_{\alpha\beta}k^\alpha\chi^\beta} \tag{2.18}$$

where $\alpha_{\alpha\beta}$ are the different amplitudes and $k^\alpha = (\omega, \mathbf{k})$ is the wave vector with $k^\alpha k_\alpha = 0$ and $\omega = |\mathbf{k}|$. Furthermore, from the plane-wave solution, we find that the waves are propagating with the speed of light $c = 1$. To simplify the matrix $\alpha_{\alpha\beta}$, we can introduce two more conditions

$$h_{0i} = 0 \tag{2.19}$$
$$h^\beta_\beta = 0 \tag{2.20}$$

where $i = 1, 2, 3$. From these two conditions and the Lorenz condition given in Eq. 2.15 we find that

$$\alpha_{00} = 0 \tag{2.21}$$
$$k^j \alpha_{ij} = 0. \tag{2.22}$$

The last equation yields that the gravitational waves are transverse. Eqs. 2.15, 2.19

and 2.20 define the transverse-traceless gauge (TT) where the plane-wave solutions given in Eq. 2.18 can be rewritten as

$$h_{\alpha\beta}^{TT} = A_{\alpha\beta} e^{i\eta_{\alpha\beta} k^{\alpha} \chi^{\beta}} \tag{2.23}$$

where $A_{\alpha\beta}$ is the polarisation vector. Assuming that the wave propagation is along the z-axis, the general solution of the linearised Einstein equations in the TT gauge becomes

$$h_{\alpha\beta}^{TT} = \begin{pmatrix} 0 & 0 & 0 & 0 \\ 0 & h_{+} & h_{\times} & 0 \\ 0 & h_{\times} & -h_{+} & 0 \\ 0 & 0 & 0 & 0 \end{pmatrix} e^{i\omega(z-t)} \tag{2.24}$$

where h_+ and h_x represent the amplitudes of the gravitational waves in the two gravitational wave polarisations and the common factor $e^{i\omega(z-t)}$ represents the time and space dependence of the wave, emphasizing the common oscillatory behaviour of the two polarizations.

The metric perturbations $h_{\alpha\beta}$ cause no change in the distance between two particles along the z-axis. However, as the gravitational wave propagates, the transverse separations between two particles change with time. We can then define the complex strain h from the cross and plus gravitational wave polarisations

$$h = h_{+} - i h_{\times}. \tag{2.25}$$

To sum-up from the solutions of the linearised Einstein equations, we have found that the gravitational waves propagate at the speed of light, are transverse and have two independent polarisations. Furthermore, we have discussed how they interact with test particles.

2.2.2 Gravitational wave sources

The universe is replete with numerous sources of gravitational waves. Gravitational waves can be produced by any non spherically or cylindrically symmetrical acceleration. This can be better understood if we consider the mass quadrupole moment. According to general relativity, the quadrupole moment is the lowest order moment that can produce gravitational radiation. The lower monopole moment representing the total mass of a system that remains

conserved due to the mass conservation, is unable to radiate gravitationally. Similarly, the dipole moment and its first derivative represent the center of mass and the linear momentum of the system, respectively, and due to the conservation of momentum, it is also unable to generate gravitational waves. While the dipole measures the mass distribution away from the center of mass in a specific direction, the mass quadrupole moment signifies the stretching of mass along an axis *i.e.* a sphere will have zero quadrupole. To rephrase now the statement at the start of this paragraph, gravitational waves are produced by time-varying mass quadrupole moments. For a more in-depth discussion of the mass moments and gravitational radiation, the reader is encouraged to consult Refs. [22, 23].

In the universe, supernova explosions, binary systems, non-spherical spinning stars, the big bang, are just some examples of gravitational wave sources [24, 25]. The gravitational wave signals emitted by these sources can be classified in three categories in terms of the nature of these signals [26, 27]. Transient signals can be defined with respect to the sensitivity of the employed detector as the product of events characterised by brevity in time or events of longer duration such as the coalescence of compact binaries that have been the primary focus of gravitational waves astronomy and can be detected during the final stages. Another type of signal are the continuous signals. The signals in this category have a significantly longer duration increasing in theory the likelihood of observing them. However, their inherent weakness poses a considerable obstacle postponing their detection. The final category is stochastic signals. This term is used to describe a collection of multiple, weak signals rather than isolated individual ones. The signals comprising this sum originate from numerous different sources at various points in time.

The gravitational waves of these sources are emitted across a large range of frequencies and their detection depends on the sensitivity band of the gravitational wave detectors. Current ground based detectors are sensitive to gravitational wave signals within the high-frequency band, spanning from 1 Hz to 10^4 Hz [28, 29, 30, 31]. Some of the sources that can possibly be detected by these interferometers are the compact stellar-mass binaries, core-collapse supernovae and stochastic backgrounds. During the first three observing runs, these detectors identified a large population of binary black hole mergers alongside a smaller number of binary neutron star and neutron star-black hole mergers [11, 12, 13, 9]. Future detectors are expected to make detections at dif-

ferent frequency ranges allowing the detection of gravitational waves emitted from new sources like supermassive black holes that we expect to detect with LISA [32]. In this thesis we will focus on gravitational wave signals emitted from compact binary systems and more specifically binary black hole systems.

The dynamical evolution of a compact binary system is characterised by three distinct phases: the inspiral, merger and ringdown of the system. During these three phases the system emits gravitational radiation and loses energy and angular momentum. At the start of their coalescence, the two compact objects are gravitationally bound, but widely separated exhibiting a quasi-spherical inspiral motion. During this phase, the emission of gravitational waves causes the gradual reduction of the separation between the two objects.

The duration of the inspiral phase in the detectors' sensitivity band is dictated by the masses of the two companions. Objects with greater mass, such as black holes, emit significantly shorter gravitational wave signals compared to lighter objects like neutron stars. During the last orbits of the binary, while the separation between the two objects decreases faster, the emitted gravitational waves become stronger and carry away from the system significant amounts of energy. At the point of merger, the two objects merge into a single remnant black hole. Then during the final phase of the coalescence the produced Kerr black hole goes through damped perturbations and the emitted gravitational radiation is in the form of quasinormal modes.

2.3 Gravitational wave detectors

Gravitational wave detectors utilize the principle of interferometry to detect passing gravitational waves. During the first three observing runs $O1 - O3$, three gravitational wave detectors, the LIGO Livingston, LIGO Hanford and Virgo detectors, were in operation and built a catalogue of close to 100 detections of compact binary mergers. These detectors are in the form of ground based, L-shaped interferometers that take advantage of the quadrupolar deformations that are produced by a passing gravitational wave. They closely resemble a Michelson-Morley interferometer, but they are significantly more complex and larger with arm length of 4 km for LIGO and 3 km for Virgo.

The detectors use a highly sensitive laser beam that is split in two equal beams that each is directed along one of the orthogonal arms of the detector. The beams travel multiple times back and forth the arms reflected by the

mirrors that are placed at the end of the arms and close to the beam splitter before they recombine at the beam splitter. In the absence of detections, the two beams are designed to remain out of phase when travelling the same distance, causing their destructive interference. A passing gravitational wave causes the deformation of space by simultaneously stretching it in one direction and shrinking it in a perpendicular direction. Therefore, the length of each arm increases and decreases alternately as gravitational waves pass and the two beams stop being out of phase. This causes the formation of an interference pattern at the output of the detector.

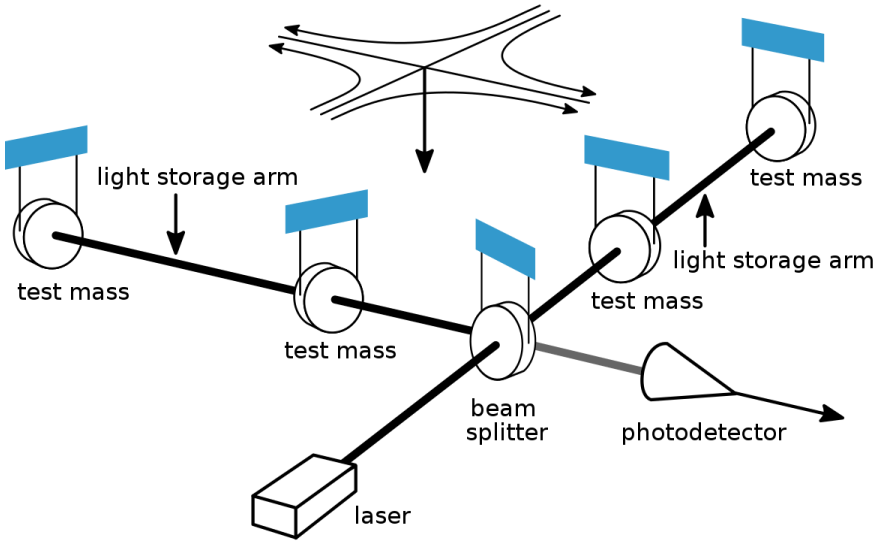

Figure 2.2: Diagram of the LIGO's interferometers. The gravitational wave is reaching the detector from directly above it. The image was taken from [7].

These large interferometers are capable of detecting binary mergers occurring at large extragalactic distances. However, the sensitivity of the detector is limited by the presence of noise. There are three main noise sources: quantum noise that consists of shot noise and radiation pressure, thermal noise and seismic noise [33, 34]. The sum of all the noise sources determines the sensitivity of the detector that is characterised by the frequency dependent power spectral density

$$\frac{1}{2}S_h(f) =< |\tilde{n}(f)|^2 > \Delta f \tag{2.26}$$

or the amplitude spectral density $S_h^{1/2}(f)$, where $\tilde{n}(f)$ is the combination of all the noise sources in the detector in the Fourier domain and the operation $<>$ denotes an average over multiple noise realizations [35].

The sensitivities of the advanced LIGO and advanced Virgo detectors dur-

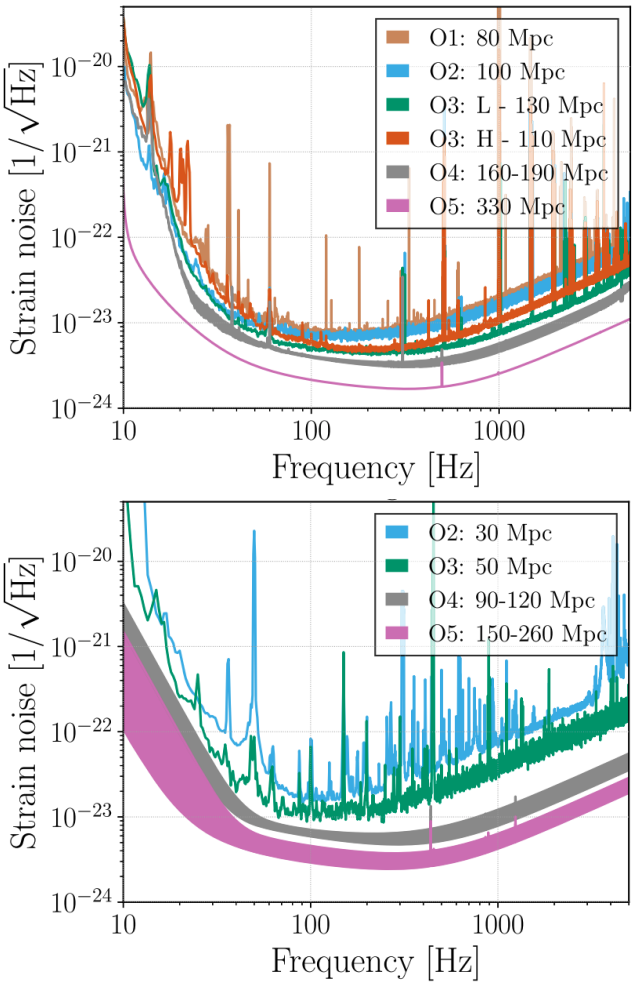

Figure 2.3: Amplitude spectral density of aLIGO (top) and AdVirgo (bottom) for the $O1$-$O5$ observing runs taken from [8]. Some of the anticipated sensitivities are shown as bands due to the uncertainty regarding the impact of the scheduled improvements. Note that the presented ranges correspond to the achieved ranges during the first three observing runs and the anticipated ranges during the next ones, for an orientation-averaged, $1.4M_{\odot} + 1.4M_{\odot}$ binary neutron star merger.

ing the first three observing runs as well as their anticipated values during the $O4$ and $O5$ observing runs [8] are shown in Fig. 2.3. The frequency-dependent strain sensitivity of each detector is limited at low frequencies by a superposition of several noise sources and by the photon shot noise at high frequencies. As can be seen from the sensitivity curves of the detectors, in $O4$ it is anticipated to have better sensitivity indicating more frequent detections. In the forthcoming chapters of this thesis, we use sensitivity curves of the LIGO Livingston, LIGO Hanford and Virgo detectors that were computed in $O3b$ and

used in LVK GWTC-3 analyses [9].

2.4 Post-Newtonian waveforms

In general relativity, the solution of the Einstein field equations is significantly simplified with the use of the post-Newtonian (PN) approximation. In Section 2.2.1, we showed that the linearised theory can offer a valuable insight into gravitational waves assuming weak gravitational fields. In linearised gravity, the curvature of the spacetime and the velocity of the gravitational wave source are regarded as independent entities. The gravitational waves are then studied as small perturbations on the flat spacetime allowing the study of their source using Newtonian physics [36, 16, 17].

However, this approximation proves inadequate in the case of relativistic systems bound together by gravitational forces. From the virial theorem, for weakly self-gravitating systems such as binaries with large separation, we have

$$(v/c)^2 \sim R_s/d \tag{2.27}$$

where v is the relative velocity in the system, $R_s = 2Gm/c^2$ is the Schwarzschild radius, m the total mass of the system and d the orbital separation. In the case of weakly self-gravitating, slowly moving sources, the curvature and the motion of the source cannot be considered independent and the post-Newtonian (PN) formalism emerges as a well-suited approach for the study and modelling of gravitational waves emitted by binary black hole systems allowing the computation of the waveform emitted by an inspiralling binary system. The basis of the PN theory is the introduction of relativistic corrections in (v/c) terms to the results of linearised theory. In the PN formalism, the equations of motion and gravitational field are expanded in terms of (v/c).

Separate PN results exist for the conservative dynamics, the radiation reaction, and the gravitational-wave strain. In Chapter 4, we make use of the results in Ref. [37], which give the gravitational wave strain up to 1.5PN order given the dynamics of a binary system. The reader can find a more detailed introduction to the PN formalism in Ref. [36]. Alternatively, Ref. [38] provides an in-depth presentation of the applications of PN theory in gravitational waves astronomy.

2.5 Binary black hole waveforms

In Section 2.2.1, we showed that the gravitational wave signal can be written as

$$h = h_+ - ih_\times. \tag{2.28}$$

The complex polarisation is frequently decomposed with respect to an orthonormal basis of spin-weighted $s = 2$ spherical harmonics $Y^{-s}_{lm}(\theta, \phi)$ that are defined on a 2-sphere where θ and ϕ are the polar and azimuthal angles. The weighted spin harmonics Y^{-s}_{lm} are defined in Ref. [39] and are given by

$$Y^{-s}_{lm}(\theta, \phi) = (-1)^s \sqrt{\frac{2l+1}{4\pi}} d^l_{sm}(\theta)\, e^{im\phi}, \tag{2.29}$$

with

$$\begin{aligned} d^l_{sm}(\theta) = \sum_{t=C_1}^{C_2} & \frac{(-1)^t \left[(l+m)!(l-m)!(l+s)!(l-s)!\right]^{1/2}}{(l+m-t)!(l-s-t)!t!(t+s-m)!} \\ & \times \left(\cos\frac{\theta}{2}\right)^{2l+m-s-2t} \times \left(\sin\frac{\theta}{2}\right)^{2t+s-m}, \end{aligned} \tag{2.30}$$

where the range of the summation is from $C_1 = max(0, m-s)$ to $C_2 = min(l+m, l-s)$ and t takes integer values within this range [40]. The gravitational wave strain can then be written in the form

$$h(\theta, \phi) = \sum_{l=2}^{+\infty} \sum_{m=-l}^{l} h_{lm}(t) Y^{-2}_{lm}(\theta, \phi). \tag{2.31}$$

The gravitational wave multipoles h_{lm} can then be obtained from the surface integral

$$h_{lm} = \int d\Omega h(\theta, \phi)\, Y^{-2*}_{lm}(\theta, \phi) \tag{2.32}$$

where $d\Omega = \sin\theta d\theta d\phi$ [37]. The h_{lm} multipoles are complex quantities that can be written as the product of their time or frequency dependent amplitude A_{lm} and phase ϕ_{lm}

$$h_{lm} = A_{lm} e^{i\phi_{lm}}. \tag{2.33}$$

In the NR simulations, we often instead calculate the Weyl scalar ψ_4 that is given by

$$\psi_4 = -R_{\alpha\beta\gamma\delta} n^\alpha \bar{m}^\beta n^\gamma \bar{m}^\delta, \tag{2.34}$$

where $R_{\alpha\beta\gamma\delta}$ is the Riemann tensor and n, $\bar{m}$ are part of a null-tetrad basis [40]. The ψ_4^{lm} multipoles of the scalar are given from its projection on the spin weight -2 spherical harmonics

$$\psi_4(t) = \sum_{l,m} Y_{lm}^{-2}(\theta,\phi)\,\psi_4^{lm}(t)\,. \tag{2.35}$$

In the Bondi gauge, ψ_4 is related to the strain h by the relation [41]

$$\psi_4 = \ddot{h}. \tag{2.36}$$

However, computing the strain from Eq. 2.36 can contaminate the sub-dominant multipoles with unphysical artefacts due to the amplification of numerical noise. As we will see in Chapter 4, this calculation can be done with a more preferable method.

2.5.1 Precessing binaries

The presence and the direction of the black holes' spins have a significant impact on the characteristics of the detected waveforms. With respect to their spins, the binary black hole systems can be classified into three distinct types: non-spinning, aligned-spin and precessing binaries.

In the case of *non-spinning binaries*, the two black holes of the system have zero spin and the direction of the orbital angular momentum, $\hat{\mathbf{L}}$, is preserved while the system's orbital plane remains fixed. However, in the presence of spinning black holes the dynamics of the system depend on the direction of the spin vectors with respect to the direction of the orbital angular momentum vector. In the special case of *aligned-spin binaries*, both black holes have spins that are aligned or anti-aligned to the orbital angular momentum $\hat{\mathbf{L}}$. Due to the presence of the aligned or anti-aligned spins, the length of the observed waveform and consequently the total time to merger increases or decreases, respectively, compared to that of the non-spinning binaries. Similar to the non-spinning binaries, the direction of the orbital angular momentum, $\hat{\mathbf{L}}$, of the aligned-spin binaries remains fixed over time resulting in a fixed, time-independent orbital plane throughout the binary black hole coalescence. In these cases, the majority of the gravitational energy that the system emits is found in the dominant $(\ell = 2, |m| = 2)$ multipoles [42].

In more generic cases where the spins are misaligned with the orbital an-

gular momentum $\hat{\mathbf{L}}$, the systems exhibit precession. The arbitrary orientation of the spins results in the coupling of the orbital angular momentum with the spins and the spins with each other. Due to these couplings, the direction of the orbital angular momentum $\mathbf{L}$ and the total spin vector

$$\mathbf{S} = \mathbf{S_1} + \mathbf{S_2} \tag{2.37}$$

become time dependent causing the precession of the orbital plane of the system [43, 44, 45]. The total spin vector precesses around the orbital angular momentum and both these vectors precess about the total angular momentum of the system given as

$$\mathbf{J}(t) = \mathbf{L}(t) + \mathbf{S}(t) \tag{2.38}$$

that maintains an approximately fixed direction over time. This type of precession is called *simple precession*. Assuming a binary with infinite separation, the total angular momentum vector is not fixed, but precesses around its average direction called *asymptotic total angular momentum direction*. However, the shift of its direction with time is small compared to the precession cones of the spins and the orbital angular momentum and can often be neglected [46, 42].

The precession of the orbital plane and the spins is reflected on the emitted radiation. The precession introduces modulations in the amplitude of the emitted waveforms and secular and oscillatory modifications in the phase of the binary. Additionally, the power that is distributed in the waveform multipoles is also affected by precession. Although in the non-precessing systems the signal's power is mostly contained in the dominant ($\ell = 2, |m| = 2$) multipoles, in the presence of precession the power is redistributed and transferred to subdominant multipoles [47].

During the binary black hole coalescence, the primary gravitational energy emission occurs along the direction of orbital angular momentum $\hat{\mathbf{L}}(t)$. Since the orbital angular momentum $\mathbf{L}(t)$ precesses around the average direction of the total angular momentum $\hat{\mathbf{J}}(t)$, the major portion of the gravitational energy is also discharged in the direction of $\hat{\mathbf{J}}(t)$ [48]. As a result, the strength of the precession effects on the detected waveforms depends on the inclination of the orbital plane with respect to the observer. The precession of the same system would be perceived differently by two static observers at different positions with respect to the initial direction of the total angular momentum. An observer

aligned with the direction of the initial total angular momentum will detect a waveform with small modulations, however, an observer positioned in an arbitrary position with respect to $\hat{\mathbf{J}}(t)$ will observe stronger effects of precession on the emitted signal since while the orbital plane precesses, their position with respect to $\hat{\mathbf{L}}(t)$ will alter with time [42, 49].

Simple precession is the most common, but not the only type of precession. In the special case that a system reaches a moment during the binary black hole coalescence where the total spin and orbital angular momentum have approximately the same amplitude and opposite directions, $\mathbf{L} \approx -\mathbf{S}$, the system undergoes a different type of precession called *transitional precession* [50]. It is important for the two vectors to only be approximately anti-aligned since there is no precession in an anti-aligned-spin binary.

For a simple precessing system to reach this epoch, the orbital angular momentum of the binary has to be initially larger than the total spin of the system. As the system evolves during the inspiral, it loses orbital angular momentum and the magnitude of $\mathbf{L}(t)$ decreases while the magnitude of the spin vector $\mathbf{S}(t)$ remains approximately the same. As a result, if the binary reaches a point where $\mathbf{L} \approx -\mathbf{S}$, the type of precession shifts from simple to transitional. The system continues in this new phase of precession for most of the inspiral phase.

Contrary to simple precession, in transitional precession, the total angular momentum $\mathbf{J}(t)$ of the system has a small amplitude and its direction is no longer approximately fixed during the inspiral. Let the orbital plane being in the x-y plane of a Cartesian coordinate system, $\hat{\mathbf{J}}(t)$ changes rapidly with time crossing the x-y plane and taking negative values. This introduces significant distortions in the emitted waveforms. However, the likelihood of detecting transitional waveforms using ground based detectors is anticipated to be very low [42]. For a more detailed description of simple and transitional precession, we direct the reader to Refs. [50, 42]. In this work, we will only be considering cases of simple precession.

2.5.2 Co-precessing frame

In an inertial frame, the presence of strong modulations in the precessing waveforms can complicate their study and the production of accurate waveform models. However, the effects of precession can be significantly minimised with the use of the appropriate frame of reference that can track the precession of

the orbital plane. A *co-precessing* frame is a non-inertial coordinate system whose z-axis tracks the direction along which the majority of gravitational energy emission occurs [47, 51, 52, 53]. The definition of the co-precessing frame does not correspond to a single frame and there are different methods to track the precession of the orbital plane.

The direction of *quadrupole alignment* corresponds to the direction along which the $(\ell = 2, |m| = 2)$ multipoles are maximised [47]. This is accomplished by finding the direction that maximises the function $|\psi_{4,22}|^2 + |\psi_{4,2-2}|^2$. We should note that this calculation can also be done with the gravitational wave strain h instead of the Weyl scalar ψ_4 leading to slightly different co-precessing frames. The non-inertial quadrupole aligned (QA) frame tracks throughout the binary black hole coalescence this direction of maximum emission which is approximately along the direction of the orbital angular momentum $\hat{\mathbf{L}}(t)$. The frame rotates to keep $\hat{\mathbf{L}}(t)$ parallel to the z-axis while the x-y plane tracks the orbital plane. In this co-rotating frame, the system is not precessing closely resembling a non-precessing system.

The QA frame is described by three Euler angles (α, β, γ) that represent the rotation of the precessing waveforms from the inertial frame to the co-precessing frame. The three Euler angles (α, β, γ) constitute the precession angles. The fundamental concept of this rotation revolves around the selection of three distinct axes and expressing the rotation as a combination of three rotations aligned with those axes.

In the first definitions of the QA frame in Refs. [47, 51] it is shown that two rotation angles are sufficient for the rotation to the co-precessing frame. However, as it is shown in Ref. [52], in the complete definition of the QA frame a third angle, γ, is also employed to adjust the phase introducing the *minimal-rotation condition* leading to a uniquely defined frame aligned with the radiation axis that remains invariant under the rotation of the inertial frame. The minimal-rotation condition leads to the expression

$$\dot{\gamma} = -\dot{\alpha} \cos \beta \tag{2.39}$$

that allows the calculation of γ from the other two precession angles.

The rotation to the QA frame is performed by applying a time dependent rotation to the inertial frame using the z-y-z convention. As a result, the $\mathbf{R}(\alpha\beta\gamma)$ rotation is performed in three steps: a rotation by α about the z-axis, followed by a rotation by β about the new y-axis and a final rotation by γ

about the z-axis. The multipoles in the QA frame $\psi^{QA}_{4,lm}$ and the inertial frame $\psi_{4,lm'}$ obey the transformation law

$$\psi^{QA}_{4,lm} = \sum_{m'=-l}^{l} e^{im'\alpha} d^{l}_{m'm}(\beta) e^{im\gamma} \psi_{4,lm'} \tag{2.40}$$

where $d^{l}_{m'm}$ are the Wigner d-matricies described in Ref. [39] and given by Eq. 2.30. Similarly, we can follow the same procedure with the precession angles $(-\gamma, -\beta, -\alpha)$ to rotate the QA frame back to the original precessing inertial frame.

2.5.3 Multipole asymmetry

In non-spinning and align-spin binaries, the direction of the orbital angular momentum $\hat{\mathbf{L}}$ remains fixed along the z-axis at all times. This results in the symmetrical emission of gravitational energy along the negative and positive directions of the z-axis. This symmetrical radiation of energy can be expressed as a symmetry between opposite waveform multipoles leading to the expression

$$h_{lm}(t) = (-1)^{l} h^{*}_{l-m}(t) \tag{2.41}$$

that is valid for non-precessing systems.

On the other hand, in misaligned-spin binaries, the direction of the orbital angular momentum $\hat{\mathbf{L}}$ changes with time leading to the precession of the orbital plane and the gravitational radiation is beamed approximately along the time dependent $\hat{\mathbf{L}}$. In these systems, the gravitational energy is no longer emitted symmetrically and the symmetry between the positive h_{lm} and negative h_{l-m} multipoles is broken. Due to this introduced multipole asymmetry, Eq. 2.41 no longer holds and the relation between opposite waveform multipoles is given by the PN expression that is introduced in Ref. [37]

$$\hat{h}_{l-m}(\Phi) = (-1)^{l} \hat{h}_{lm}(\Phi + \pi) \tag{2.42}$$

where Φ is the orbital phase and $\hat{h}_{lm}$ is the PN h_{lm} normalised by its leading order PN term; see Chapter 4 for more details. Eq. 2.42 denotes the dependency of the multipole asymmetry on the phase of the system. From this arises that when h_{lm} is independent of Φ, Eq. 2.41 holds and there is no multipole asymmetry (see relative discussion in Ref. [37]).

In the co-precessing frame as it is explained in Section 2.5.2, the frame tracks the precession of the orbital plane reducing the effects of precession on the gravitational wave signal. However, the multipole asymmetry continues to be present and Eq. 2.41 does not apply. In this frame, the majority of the energy is radiated along the z-axis, however, there is an imbalance between positive and negative multipoles meaning that the gravitational energy emitted above and below the orbital plane differs. This difference in energy emission is the result of the multipole asymmetry.

The h_{lm} and h_{l-m} waveforms are complex quantities that can be written as the sum of their symmetric and anti-symmetric contributions,

$$h_{lm} = A_s e^{i\phi_s} + A_a e^{i\phi_a}, \tag{2.43}$$
$$h_{l-m} = (-1)^l (A_s e^{-i\phi_s} - A_a e^{-i\phi_a}), \tag{2.44}$$

where A_s and A_a denote the symmetric and anti-symmetric amplitude, respectively, and ϕ_a and ϕ_s are the symmetric and anti-symmetric phase. We should note that the above quantities depend on time, or on frequency in the case where the signal is in the Fourier domain. As a result, these expressions are valid in both the frequency and time domains. Then, in a co-precessing frame, the symmetric and the anti-symmetric contributions of the $(\ell, |m|)$ multipoles are defined as the complex quantities

$$h^s_{lm} = \frac{h_{lm} + (-1)^l h^*_{l-m}}{2}, \tag{2.45}$$
$$h^a_{lm} = \frac{h_{lm} - (-1)^l h^*_{l-m}}{2}, \tag{2.46}$$

respectively, where $*$ denotes the conjugate of the complex h_{l-m} waveform that takes the form

$$h^*_{l-m} = (-1)^l (A_s e^{i\phi_s} - A_a e^{i\phi_a}). \tag{2.47}$$

Recoil velocity

The physical implication of the presence of multipole asymmetry is quite severe for the binary system. In binaries where the black hole spins are misaligned with the orbital angular momentum, the presence of multipole asymmetry leads to the recoil of the binary that is also known as the *rocket effect* [54, 55, 56, 57]. This *kick* that the black hole receives can be of thousands of km/s

and arises from the conservation of momentum.

Throughout the inspiral and merger, the emission of gravitational radiation leads to the loss of angular and linear momentum. Due to the anisotropic emission of gravitational radiation, the loss of linear momentum exhibits a preferential direction. This loss of linear momentum can be calculated from Ψ_4 by

$$\frac{dP_i}{dt} = \lim_{r\to\infty}\left[\frac{r^2}{16\pi}\int_\Omega \ell_i \left|\int_{-\infty}^{t} \Psi_4 d\tilde{t}\right|^2 d\Omega\right] \tag{2.48}$$

where ℓ_i is the radial unit vector $\ell_i = (\sin\theta\cos\phi, \sin\theta\sin\phi, \cos\theta)$ [58, 55] and due to the conservation of momentum at merger the newly formed black hole obtains recoil velocity. The mass and the spins of the two black holes as well as the dynamics of the system closer to the merger determine the value of the recoil velocity. Therefore, at merger the system receives a *kick* that removes it from its initial centre of mass.

In cases where the recoil velocity is significant, the merged black hole can be completely removed from its surrounded environment or even its host galaxy [59, 60, 61]. This leads to a slowly increasing population of interstellar and intergalactic black holes. Furthermore, the rocket effect can also have a severe effect on the evolution and formation of the host galaxies if we consider the presence of massive black holes in the galactic center that could undergo this process.

Superkick binaries

The out-of-plane recoil arises primarily due to the presence of the multipole asymmetry in misaligned binaries. This can be better understood if we consider a *superkick* configuration where the recoil velocity is large [62, 63]. In the special case of a binary system with two equal-mass black holes and in-plane spins with equal magnitude and opposite directions, $\mathbf{S_1} = -\mathbf{S_2}$, the two spins cancel out and the total spin of the binary is $\mathbf{S} = 0$. As a result, similar to the non-spinning binaries, these systems do not exhibit precession and the majority of the emitted gravitational energy is in the $(\ell = 2, |m| = 2)$ multipoles.

The superkick systems display π *symmetry* as they remain unaltered when subjected to a 180 degrees rotation around the initial z-axis or any axis perpendicular to the orbital plane. Due to this symmetry, the linear momentum of the system is radiated solely along the direction of the z-axis. Since there is no loss of linear momentum along the x and y axes, the center of mass of the

system moves only along the z-axis while its position in the x-y plane remains the same.

Although the orbital plane of the superkick binaries exhibits no precession, the asymmetry between the opposite multipoles is present and the linear momentum loss is uneven [63]. Consequently, the superkick configuration offers an insight into the effects of the multipole asymmetry while isolating them from the precession effects on the gravitational wave signal. In Ref. [63], it is found that the recoil velocity of the merged black hole increases with the energy emission difference between the opposite multipoles. Furthermore, it also concluded that there is a sinusoidal dependence of the recoil velocity and consequently of the multipole asymmetry on the initial direction of the black hole spins. These conclusions will be revisited and utilised in the forthcoming chapters.

2.6 Waveform models

The detection of gravitational waves and the extraction of information about their sources depend on the accuracy of waveform models that cover fully the inspiral-merger-ringdown (IMR) phases of the binary black hole coalescence. The development of more accurate waveform models is a continuous effort to ensure that as the sensitivities of the detectors are improved, uncertainties in the measurements that arise from approximations and missing physics will remain small facilitating the accurate estimation of the source parameters.

A large population of binary black hole mergers has been detected during the first three observing runs as described in Section 2.2.2. The waveform models that have been used by the LIGO-Virgo-KAGRA collaboration over this period for the measurement of the properties of the black holes and the location of the detected systems belong to three distinct families of waveform models. The `Phenom` [64, 65, 66, 67, 68, 69, 70, 71, 72, 73, 74, 75, 4] and `SEOBNR` [76, 77, 78, 79, 80, 81, 82] models are the most commonly used models in the analysis of detected signals and a third family, the surrogate [83, 84, 85, 1, 86] models has also been used over the last years.

The `Phenom` and `SEOBNR` waveform models employ results from the PN theory, the effective-one-body (EOB) approximation and numerical relativity to model the waveforms of non-precessing binaries. The EOB formalism is an analytical approach that is used in waveform modelling to describe the motion

and radiation of binary systems. EOB employs high-order PN results, but instead of using them in their Taylor-expanded form, it employs a resummation of these results. A detailed description of this formalism can be found in Refs. [87, 88]. The EOB theory and the PN formalism introduced in Section 2.4 are two approaches to the two-body problem that possess distinct advantages and limitations.

The EOB theory has been found to be accurate in the late inspiral and the merger where the PN formalism that is accurate in the early inspiral cannot be used. In addition, the successful generation of numerical relativity (NR) simulations in 2005 [89, 90, 91] opened the way to the generation of accurate waveform models throughout the IMR. A combination of PN and EOB results has proved sufficient for the accurate modelling of the inspiral while the NR simulations are employed to tune the `Phenom` and `SEOBNR` models at the late inspiral and merger.

These approaches were first applied in the modelling of aligned-spin binaries, where there is no precession to produce aligned-spin `Phenom` and `SEOBNR` models [65, 66, 73, 72, 75, 70, 76, 79]. In misaligned-spin binaries, the presence of precession introduces modulations to the amplitude and phase of the signal and makes its dynamical evolution more complex as we described in Section 2.5.1. These effects are significantly simplified with the use of the appropriate frame. The co-precessing frame that we described in Section 2.5.2, tracks the precession of the orbital plane and thereby the precessing waveform in this frame approximately resembles a non-precessing waveform [42, 49, 68, 77, 64, 84].

The `Phenom` and `SEOBNR` models employ this simplification of the signal in the co-precessing frame to model the precessing waveforms. Instead of directly modelling the more complex precessing signal, both models compute an approximate precession waveform by transforming the non-precessing model to the inertial frame assuming that the non-precessing waveform is a precessing waveform in a co-precessing frame. This rotation to the inertial frame is performed using an independent model for the precession dynamics [64, 68, 92, 74, 77, 76, 93].

In the first `Phenom` models the six spin components of the two black holes of the system are captured by two parameters, the effective aligned-spin parameter, χ_{eff} and the effective precession spin parameter, χ_p [49]. The χ_{eff} was introduced in `PhenomB` [94] to capture the effects of the two spin compo-

nents that are parallel to the orbital angular momentum of the system and is denoted from the following relation

$$\chi_{eff} = \frac{1}{M}(m_1\chi_1 + m_2\chi_2) \tag{2.49}$$

where χ_i are dimensionless spins, m_i the individual masses of the black holes and M the total mass [95]. The χ_p parameter is later introduced in `PhenomPv2` to substitute the four in-plain spin components of the system and its value is assigned to the larger black hole of the system. The last captures the dynamics of precession and is denoted from

$$\chi_p = \frac{S_p}{m_2^2} = max(A_1 S_{1\perp}, A_2 S_{2\perp}), \tag{2.50}$$

where $A_1 = 2 + \frac{3m_2}{2m_1}$ and $A_2 = 2 + \frac{3m_1}{2m_2}$ for $(m_2 > m_1)$ and $S_\perp$ the perpendicular to $\bar{L}$ spin components, respectively, [49, 96]. The χ_{eff} and χ_p parameters continue to be part of the data analysis process as their calculation allows us to gain an insight into the system's spin dynamics and indicates the presence of precession.

The `IMRphenomXPHM` model is the most recent `Phenom` model that was used during the $O3$ observing run for the analysis of the detected signals. It is a frequency-domain model that was built as an extension of `IMRphenomXHM`. In `IMRphenomXPHM` higher multipoles up to $\ell \leq 4$ have been included and tuned to NR data. Furthermore, precession effects have been modelled, but have not been tuned to NR simulations.

In the latest frequency-domain `Phenom` model, `IMRphenomPNR`, that is built upon the aligned-spin model, `PhenomD`, the precession effects at merger and ringdown have been modelled against NR simulations. As we will discuss in the next chapter, up until recently, none of the `Phenom` waveforms modelled the asymmetry between the multipoles, discussed in Section 2.5.3. In Chapter 4, we will introduce a model of the multipole asymmetry that has been added to `IMRphenomPNR` and is the first phenomenological multipole asymmetry model.

2.6.1 Surrogate models

The development of the surrogate waveform models relies mainly on the NR waveforms. NR waveforms that accurately capture the evolution of the binary black hole systems, are employed to train these models minimising the intro-

duction of any additional assumptions that are present in the other families of waveform models [83, 84, 85, 1, 86]. Therefore, compared to other waveform models, surrogate models are significantly more accurate within the parameter space of the NR waveforms they were trained against. The state-of-the-art surrogate is the `NRSur7dq4` waveform model introduced in Ref. [1].

As we explained at the start of this section, for the modelling of precessing waveforms, the use of a co-precessing frame, a non-inertial frame that tracks the precession of the orbital plane, simplifies a precessing waveform that becomes similar to that of a non-precessing binary. Similarly to the other waveform models, the surrogate employs a similar approach and models the precessing waveforms in a *co-orbital* frame [1]. A waveform in the co-precessing frame $h^{copr}_{lm}(t)$ can be transformed to the co-orbital frame by applying a rotation around the z-axis of the co-precessing frame,

$$h^{coorb}_{lm}(t) = h^{copr}_{lm}(t) e^{im\phi(t)} \tag{2.51}$$

where the $\phi(t)$ is the orbital phase given by

$$\phi(t) = \frac{\arg\left[h^{copr}_{2-2}(t)\right] - \arg\left[h^{copr}_{22}(t)\right]}{4}. \tag{2.52}$$

In the co-orbital frame, the black holes of the binary remain on the x-axis with the larger black hole always placed in the positive x-axis. In this frame, the presence of oscillations introduced by precession are further minimised simplifying even more the modelling of the waveforms. In the surrogate, the co-orbital waveforms are further split into the plus h^{+}_{lm} and minus h^{-}_{lm} contributions that correspond to the symmetric and anti-symmetric contributions,

$$h^{\pm}_{lm} = \frac{h^{coorb}_{lm} \pm h^{coorb*}_{l-m}}{2} \tag{2.53}$$

for $m > 0$. For even ℓ the symmetric contribution is $h^{+}_{\ell m}$ and the anti-symmetric contribution is $h^{-}_{\ell m}$, and for odd ℓ it is the reverse. Each of these components is modelled independently and from their combination the co-orbital frame surrogate is obtained [84, 1].

Although, within its validity range, the accuracy of the surrogate is comparable to that of the NR simulations, in other parts of the parameter space its accuracy declines [1]. The surrogate has been trained against 1528 NR waveforms with mass ratios $q \leq 4$, spin magnitudes $\chi_1, \chi_2 \leq 0.8$ and includes

all $\ell \leq 4$ spin weighted spherical harmonic multipoles. Additionally, the surrogate models are produced from NR waveforms that exhibit a limited number of orbits prior to the merger of the system. For the modelling of the non-precessing systems, the surrogate models employ hybridised NR waveforms that are constructed by stitching PN/EOB waveforms with NR results [86]. This method is considered as a possible approach in the efforts to increase the length of precessing surrogate waveforms. Furthermore, assuming a waveform with a starting frequency of 20 Hz, the precessing surrogate `NRSur7dq4` stops being valid at lower total mass $M \lesssim 66 M_{\odot}$.

The use of the surrogate for the measurement of the source parameters is limited only within its validity range and the analysis of signals outside this range can only be done with the `Phenom` and `SEOBNR` models, which are in principle usable at all masses, and for a wide range of mass ratios. In Chapter 3, we will discuss further the implications of these limitations and the construction of the surrogate.

2.6.2 Systematic errors

The IMR models are employed by the matched filtering techniques that are used in the search of signals emitted from binary black hole systems. These techniques are sensitive enough to identify the signals that are generated during the coalescence of the system and separate them from the noise in the data [97], [98]. Then the source parameters of the detected systems are recovered by matching the models to the signals.

The waveform models are approximate models that have a number of simplifications. These simplifications are introduced in some cases due to the high computational cost of the NR simulations or in order to simplify the modelling process by introducing approximations and not including physical effects that are not expected to affect the analysis of the detected signals. However, as the sensitivities of the detectors are improved, the inclusion of some of the missing physics is required to ensure the accuracy of the models in the future detections. Otherwise, these simplifications could be the source of systematic errors in the measurement of the source parameters [96].

This type of errors differ from the statistical errors that depend on the width of the posterior distribution around the mean value of the measured parameter and are the result of introduced detector noise or low signal-to-noise ratio (SNR). In contrast, in the presence of the systematic errors, we observe

an overall shift of the recovered values from their true values. Therefore, the use of certain approximations could introduce significant biases in the measurements of the source parameters resulting in misleading conclusions regarding the detected systems. In the case of the `Phenom` and `SEOBNR` waveform models, one of these simplifications is the absence of the multipole asymmetry from the available models.

In the forthcoming chapters, we employ the `NRSur7dq4` to investigate the importance of including the multipole asymmetry in the waveform models and we present the first `Phenom` model of the multipole asymmetry. `NRSur7dq4` is the first waveform model that modelled the anti-symmetric contribution of the waveform. The clear separation of the symmetric and anti-symmetric waveform contributions in this model enables a simple removal of the anti-symmetric contribution, thereby allowing us to utilize this model effectively to study the effects that the absence of the multipole asymmetry has on the data analysis. Furthermore, due to the high accuracy of the surrogate within a specified area of the parameter space, the selection of appropriate binary configurations within this area allows us to treat `NRSur7dq4` as our "true" model and the starting point for systematic studies.

2.7 Parameter estimation

The measurement of the source parameters from the detected gravitational wave signals offers a unique opportunity to study their population, understand their formation mechanisms and test the theory of general relativity as well as other theories of gravity. To obtain the astrophysical parameters of the sources, we utilise statistical inference techniques on the signals' data $\boldsymbol{d}(t)$ that are the sum of the signal $\boldsymbol{s}(t)$ and the combination of all the noise sources $\boldsymbol{n}(t)$,

$$\boldsymbol{d}(t) = \boldsymbol{s}(t) + \boldsymbol{n}(t). \tag{2.54}$$

The weak nature of the detected signals results in large uncertainties in the parameters we wish to measure and prior assumptions regarding the amplitude and phase evolution of the signals influence greatly the reconstructed waveforms. To address these factors, the inference of the system's physical parameters is carried out within the framework of Bayesian parameter estimation [35].

Given a waveform model h_M and $\boldsymbol{\theta}$ the model parameters that we wish to measure, by employing the Bayes' theorem [99] that is defined as

$$p(\boldsymbol{\theta}|\boldsymbol{d}, h_M) = \frac{p(\boldsymbol{d}|\boldsymbol{\theta}, h_M)p(\boldsymbol{\theta}|h_M)}{p(\boldsymbol{d}|h_M)}, \tag{2.55}$$

we can calculate the posterior probability $p(\boldsymbol{\theta}|\boldsymbol{d}, h_M)$ that is proportional to the prior probability distribution $p(\boldsymbol{\theta}|h_M)$ and the likelihood $p(\boldsymbol{d}|\boldsymbol{\theta}, h_M)$. The latter is the probability the data $\boldsymbol{d}$ to be observed given we use a model h_M with parameters $\boldsymbol{\theta}$. Following the assumption that the noise can be treated as stationary, Gaussian and independent between each of the detectors, we can define a Gaussian likelihood [35] for each detector,

$$\mathcal{L} \propto \exp\left[-\frac{1}{2}\langle \boldsymbol{d}(t) - h_M(\boldsymbol{\theta})|\boldsymbol{d}(t) - h_M(\boldsymbol{\theta})\rangle\right], \tag{2.56}$$

where $h_M(\boldsymbol{\theta})$ is the waveform model evaluated at $\boldsymbol{\theta}$ and the operation $\langle\cdot|\cdot\rangle$ is the noise weighted inner product. The inner product of two waveforms $h_1(f)$ and $h_2(f)$ is given by

$$\langle h_1|h_2\rangle = 4Re\int_0^\infty \frac{h_1(f)h_2^*(f)}{S_n(f)}df, \tag{2.57}$$

where $S_n(f)$ is the power spectral density of a detector [100, 101, 102]. The likelihood function given by Eq. 2.56 holds substantial significance in Bayesian inference. Together with the selection of appropriate priors [103], it facilitates the computation of the model evidence

$$p(\boldsymbol{d}|h_M) = \int d\boldsymbol{\theta} p(\boldsymbol{\theta}|h_M)p(\boldsymbol{d}|\boldsymbol{\theta}, h_M) \tag{2.58}$$

that provides the odds of a signal being present [104, 105]. These calculations allow the evaluation of the posterior distributions for the model parameters $\boldsymbol{\theta}$.

The waveform model parameters $\boldsymbol{\theta}$ define a N-dimensional vector $\boldsymbol{\theta} = \{\theta_1, \theta_2, ...\theta_N\}$. To find the posterior of one parameter, we first substitute $\boldsymbol{\theta}$ in equation 2.55 and we obtain the joint posterior probability which contains all the information about these parameters [98]. Then, by marginalising over the other parameters θ_i, we obtain the wanted probability, for example for the

parameter θ_1 we have

$$p(\theta_1|\boldsymbol{d}, h_M) = \int d\theta_2 ... d\theta_N p(\boldsymbol{\theta}|\boldsymbol{d}, h_M). \tag{2.59}$$

From the last relation we can see the dependence of the recovered parameters on the information about the system before and after the observations [98]. The mean of a parameter θ_i is given from

$$\langle \theta_i \rangle = \int \theta_i p(\theta_i|\boldsymbol{d}, h_M) d\theta_i. \tag{2.60}$$

An in-depth description of the data analysis techniques that are used in the detection of the gravitational wave signals and the inference of the source properties is given in Ref. [35]. In this thesis, we perform parameter estimation using the LALInference software library, a software package that is presented in Ref. [98] and has all the needed algorithms and infrastructure. Another parameter estimation pipeline that has been widely by the LVK collaboration is BILBY [106]. For an introduction to these two parameter estimation pipelines, we refer the reader to [98] and [106].

LALInference provides support for two stochastic sampling techniques, the Markov-chain Monte Carlo (MCMC) sampler [107] that will be used in the following chapter and the nested sampling techniques [104]. The MCMC algorithms estimate the posterior distribution by iteratively sampling the parameter space and exploring the regions of high probability. MCMC algorithms are designed to stochastically wander through the parameter space, generating samples that are distributed proportionally to the density of the target posterior distribution. In MCMC each sample is dependent on the previous sample. These methods use a proposal distribution to generate a new sample based on the current sample, and then decides whether to accept or reject the new sample based on a certain criterion. This allows the chain to move gradually towards the regions of higher probability in the parameter space. The MCMC implementation in LALInference employs the Metropolis–Hastings algorithm described in Refs. [108, 109].

The nested sampling technique employs a Monte Carlo approach. In this sampling technique, starting from a set of initial points sampled from the prior distribution, the lowest likelihood points are replaced by higher likelihood samples while concurrently estimating the evidence integral. This iterative process continues until a stopping criterion is met, resulting in the estimation

of the evidence and a representative sample from the posterior distribution. A summary of these two sampling techniques can be found in Ref. [98].

2.8 Numerical relativity waveforms

The Einstein equations govern the dynamical behaviour of a physical system and provide a framework for studying gravitational phenomena. They consist of ten differential equations that describe the fundamental interactions of gravity and spacetime geometry as discussed in Section 2.1. However, their analytical solution is not feasible for complex spacetimes and sophisticated numerical techniques are employed to solve the Einstein equations numerically [110].

To solve these equations numerically, the 4-dimensional spacetime manifold is appropriately sliced using the $3+1$ decomposition. The $3+1$ decomposition is a technique to split the 4-dimensional spacetime into 3-dimensional spacelike hypersurfaces that correspond to specific moments in time. This method is particularly important for the generation of NR simulations, as it allows the spacetime to be treated as a sequence of spatial slices evolving over time. A detailed description of the $3+1$ decomposition of Einstein's equations can be found in Ref. [110].

2.8.1 BAM Code

In the last decade, a number of different methods has been developed and adopted to create numerical codes that solve Einstein's equations. The most notable codes are the BAM code [111, 40, 112] that follows the "moving puncture" approach [90, 91] and the Spectral Einstein Code (SpEC) that uses pseudo-spectral methods [113]. In this thesis, we will discuss briefly the BAM code that has been used to generate the NR waveforms that consist the BAM catalogue and have been used for the modelling of the multipole asymmetry in Chapter 4.

The BAM code employs the moving puncture approach to evolve the black hole spacetime, where the wormhole topology is used to simulate the black holes of the binary [114]. In this topology, instead of reaching the singularities of the black holes we adopt a transformation from Schwarzschild coordinates to isotropic and transfer to a asymptotically flat end connected to the initial flat region by a wormhole [115]. The asymptotically flat ends are compactified

in a way that its spatial infinity is mapped to a single point referred to as a "puncture". This construction avoids all of the black hole singularities, eliminating the need to remove any region during numerical simulations using these data.

To initiate the simulations, we employ black hole binary puncture initial data [116, 117] which were generated using a pseudo-spectral elliptic solver [118]. Subsequently, the evolution of the initial data was carried out using the χ-variant of the moving-puncture [90, 91] method of the BSSN [119, 120] formulation of the 3+1 Einstein's equations. The code employs spatial finite-difference derivatives that exhibit sixth-order accuracy within the bulk [112]. For the time evolution, a fourth-order Runge-Kutta algorithm is utilized [40]. The Berger-Oliger adaptive mesh refinement [121] is used.

In the simulation, the grid is structured using a hierarchical arrangement of nested Cartesian grids. At the lower levels of the hierarchy, there are two distinct grids centred on individual punctures. At the higher levels, as the two grids approach the point of overlapping, they are replaced by a unified grid centred on the center of motion that contains the two punctures. In this grid arrangement, the smaller grids in the lower levels track the punctures' positions using a shift vector while the larger grids remain stationary [40]. The levels have different resolutions that are higher at the levels where the wave extraction takes place. The information of the binary is extracted from the simulation using the Newman-Penrose formalism [122], where the outgoing transverse gravitational radiation is given by the Weyl scalar ψ_4 [40]. The Weyl scalar is computed at the selected extraction radii from Eq. 2.34.

The eccentricity of a binary black hole system reduces, while the system emits gravitational waves and is led to merger. During the quasi-circular orbits of the inspiral, the eccentricity needs to remain close to zero and the low eccentricity evolution of the initial data is required. The eccentricity can be estimated from the following relation

$$e_D(t) = \frac{D(t) - D_c(t)}{D_c(t)}, \tag{2.61}$$

where $D(t)$ is the coordinate separation and $D_c(t)$ the coordinate separation that corresponds to a zero-eccentricity quasicircular inspiral [123].

2.8.2 BAM catalogue

The accurate modelling of the binary black hole late inspiral and merger requires the use of NR simulations that cover well the parameter space. The BAM catalogue presented in Ref. [5] consists of 80 NR simulations that were generated using the BAM code. The catalogue comprises single spin precessing configurations where the larger black hole of the binary is spinning.

Each of these 80 configurations is characterised by the individual masses of the two black holes m_1 and m_2, the mass ratio $q = m_1/m_2 > 1$, the magnitude of the larger black hole spin χ and the angle θ_{LS} between the spin and the orbital angular momentum of the binary. The catalogue covers a large area of the parameter space that extends to higher mass ratio with $q \in [1, 2, 4, 8]$, $\chi \in [0.2, 0.4, 0.6, 0.8]$ and $\theta_{LS} \in [30^o, 60^o, 90^o, 120^o, 150^o]$.

The waveforms of this catalogue have been used for the tuning of the `PhenomPNR` model presented in Ref. [4] and the development of the first phenomenological multipole asymmetry model. We should note that [124] was used for many of the processes and calculations that were required for the use of the BAM catalogue. In Chapter 4, we describe in detail the construction of the asymmetry model. However, before we delve into the modelling of the asymmetry, let us first understand the motivation behind this endeavour in the next chapter.

Chapter 3

Multipole asymmetries and parameter biases

The accurate extraction of properties from binary black hole detections relies heavily on waveform models. However, approximations used in these models may introduce systematic errors in parameter estimation results. One such approximation is the assumption that the gravitational energy is emitted symmetrically above and bellow the orbital plane even in systems where this symmetry is broken by precession. Neglecting this asymmetry could result in biases in parameter measurements. In this chapter, we investigate the presence of this potential bias in LIGO-Virgo parameter estimation results. Using the surrogate model, `NRSur7dq4`, where the effects of multipole asymmetry have been incorporated, we search for systematic biases by injecting the surrogate and recovering with both the original model and a symmetric version of the `NRSur7dq4` model. We also extend this study to include the GW200129_065458 signal, which we refer to as GW200129. This is the first LVK event where a clear measurement of in-plane spins was possible. We recover the GW200129 data with the two versions of the `NRSur7dq4` model. Our results indicate that, for precessing systems, the absence of multipole asymmetry is a significant source of systematic biases in the measurement of the black hole spins. These findings highlight the importance of accurately modelling multipole asymmetry in future waveform models.

3.1 Introduction

Gravitational wave detections provide us with a unique opportunity to observe and study some of the most extreme events that take place in our universe. Since the first gravitational wave detection of a binary black hole merger in 2015, several other detections have been made including primarily black hole mergers and more recently neutron star mergers as well as neutron star and black hole mergers [10, 11, 12, 13, 9, 125]. These detections opened up avenues for measuring the parameters of these binaries and exploring their formation mechanisms. However, the accuracy of the gravitational wave measurements depends on theoretical waveform models and any systematic biases in the models can lead to incorrect inferences about the source properties.

For binary black hole binaries, waveform models describe the three stages of the dynamical evolution of a binary black hole system, the inspiral, the merger and the ringdown. As explained in Chapter 2, there are currently three types of theoretical waveform models that are commonly used in binary black hole detections characterised by different modelling approaches. The `Phenom` and `SEOBNR` models are based partly on PN and EOB results and partly on tuning to NR simulations [4] [93]. The surrogate models rely on accurate NR waveforms and are extremely accurate models within the parameter space of their training NR simulations [1]. Full details about the surrogate are given in Section 2.6.1.

Several approximations are used in waveform modelling to simplify the process of constructing the models, or to reduce the number and accuracy of the NR waveforms that must be used. However, these approximations can introduce systematic errors in the measurement of the source parameters. The multipole asymmetry, an asymmetry between the positive and the negative m spherical harmonic multipoles, is one of the features of precessing binary black hole systems that is not present in the current `Phenom` [64, 65, 66, 67, 68, 69, 70, 71, 72, 73, 74, 75, 4] or `SEOBNR` [76, 77, 78, 79, 80, 81, 82] models.

In the special case where we have a non-precessing system in a frame where the orbital angular momentum $\bar{L}$ remains parallel to the z-axis at all times, there is a symmetry between the positive and the negative multipoles of the gravitational wave of the form,

$$h_{lm}(t) = (-1)^l h^*_{l-m}(t). \tag{3.1}$$

In binaries where one or both black holes have spins that are not parallel to the orbital angular momentum of the system, the spins and the orbital angular momentum precess around the total angular momentum of the binary. As a result, the orbital plane wobbles introducing modulations to the amplitude and the phase of the gravitational wave signal. In these cases, the precession breaks the multipole symmetry and Eq. 3.1 is no longer valid as described in Section 2.5.3.

The strength of the multipole asymmetry depends on the in-plane spin magnitude and the mass ratio of the binary system. In the presence of this asymmetry, the energy is emitted in a preferred direction that results in the loss of linear momentum. This loss is maximised close to the merger and imparts a recoil velocity due to the linear momentum conservation. At this point, the black hole that is formed receives a kick that depends on the mass ratio and spins of the initial black holes and can be up to thousands of km/s [54, 55, 56, 57]. The subject of modelling the asymmetry will be revisited in the next chapter.

Previous studies have shown that the absence of the multipole asymmetry effects from the waveform models could introduce biases in the measurement of the binary black hole parameters at SNR between 15 and 80 and in particular at SNR where we expect to measure precession [126, 127]. The recent detection of the highly precessing GW200129 signal that was found to have a large recoil velocity [2, 3] indicates that the detection of a number of precessing signals can be expected in the near future. Furthermore, the large recoil of GW200129 is a sign that the effects of the asymmetry are measurable. This implies that the multipole asymmetry has already become important in observations.

These possible biases are particularly important for future detections as the sensitivity of the detectors is improved and signals will be recovered at higher SNR. Biases in the measurement of the source parameters could have a significant impact on population studies and the efforts to better understand the formation of the observed black holes that rely on the accurate measurement of the binary black hole parameters. Although the asymmetry is modelled in `NRSur7dq4`, this model has a limited range of validity as we will explain in the next section. As a result, it is essential to study the effects that the absence of the multipole asymmetry has on our measurements and include it in the `Phenom` and `SEOBNR` waveform models if this is required.

In this chapter, we will explore the systematic biases that can arise in the

waveform models when the multipole asymmetry is neglected and their impact on the gravitational wave measurements. Our analysis will provide important insights into the reliability of future gravitational wave measurements and inform the development of more accurate waveform models in the future.

In Section 3.2, we discuss the selection of appropriate waveform models that allow us to isolate the effects of the multipole asymmetry. In Section 3.3, we discuss how the parameter estimation runs were set up and the selection of the appropriate configurations for this study. The final results are presented in Section 3.4 and the conclusions of this study are discussed in Section 3.5.

3.2 Waveform model

As has been discussed in the previous section the phenomenological models use a number of simplifications including the non-inclusion of the multipole asymmetry. The search of systematic errors introduced by the multipole asymmetry requires the isolation of this effect. Consequently this study cannot be performed with the current phenomenological models.

These limitations do not apply to the surrogate waveform model `NRSur7dq4` where the inclusion of multipole asymmetry allows the search of biases in the parameter estimation results. The `NRSur7dq4` model has been built from numerical relativity simulations with mass ratios $q \leq 4$, generic spin directions and spin magnitudes up to 0.8 and includes all $\ell \leq 4$ spin weighted spherical harmonic modes. In addition, these NR simulations start at $\sim$ 20 orbits or $\sim 4300M$ prior to merger. Therefore, the surrogate models are restricted to waveforms of this length and are inadequate whenever longer waveforms are required. Assuming for example a waveform with a starting frequency of 20 Hz, the surrogate will only be valid for binaries with total masses $M \gtrsim 66M_{\odot}$ depending on the mass ratio of the system [1]. However, within its range of validity `NRSur7dq4` is currently the most accurate waveform model.

To perform a systematics study we isolated the effect of the multipole asymmetry on the parameter estimation results by using two versions of the `NRSur7dq4` surrogate model, the "full" `NRSur7dq4` and the "symmetric" `NRSur7dq4`. The full `NRSur7dq4` is the original `NRSur7dq4` waveform model without any alterations. The symmetric `NRSur7dq4` is a simplified, altered version of this model. In the symmetric version of the model in LALSuite software library [128], the multipole asymmetry has been removed and only the symmetric waveform

remains present, thus Eq. 3.1 applies. As discussed in Section 2.6.1, in the surrogate, the co-orbital waveforms are split into the plus h^{+}_{lm} and minus h^{-}_{lm} contributions given by Eq. 2.53. Each of these components is modelled independently and from their combination the co-orbital frame surrogate is obtained [84, 1]. Therefore, by also taking into account Eqs. 2.43 - 2.46, to remove the multipole asymmetry, for even ℓ we have set to zero the h^{-}_{lm} expression in the co-orbital frame while the h^{+}_{lm} expression of the symmetric contribution takes the following form,

$$h^{+}_{lm} = \frac{h^{coorb}_{lm} + h^{coorb*}_{l-m}}{2}, \tag{3.2}$$

and the reversed have been done for odd ℓ. Then to isolate the effect that the absence of the multipole asymmetry has on the measured source parameters, we look at measuring the properties of a full signal using both the full and symmetric `NRSur7dq4` models. We refer to the symmetric `NRSur7dq4` model as `NRSur7dq4_sym` to simplify notation. As we will see in the next session, setting up two identical parameter estimation runs that only differ by the presence or the absence of the multipole asymmetry permits a direct systematics study of its effects.

3.3 Parameter estimation analysis

The aim of this study is to understand the effects of the absence of the multipole asymmetry from the waveform models in the measurement of the source parameters. To better understand these effects and the conditions that affect them we consider a number of different binary configurations and we performed a series of injections with the `NRSur7dq4` surrogate. Additionally, to explore the impact that neglecting multipole asymmetry has on current and near-future observations, we also consider the public detector data of the precessing signal GW200129 that have undergone glitch removal. Following the subtraction of the glitches, we refer to these as "de-glitched" data [9, 3].

The analysis is performed using the MCMC stochastic sampling technique from the LALInference software library presented in Ref. [98] that was used for the first observing runs, $O1-O2$ [10, 11, 12, 13, 9]. LALInference is widely used for Bayesian inference data analysis and it contains all the required algorithms and infrastructure. For our analysis, we use all three detectors and public

available power spectral densities that were taken during the *O3b* observing run and used in LVK GWTC-3 analyses [9]. It is important to note that these are the same power spectral densities that were used in the analysis of the GW200129 signal in Refs. [9, 3]. The corresponding sensitivity curves of the LIGO Hanford, LIGO Livingston and Virgo detectors are shown in Fig. 3.1.

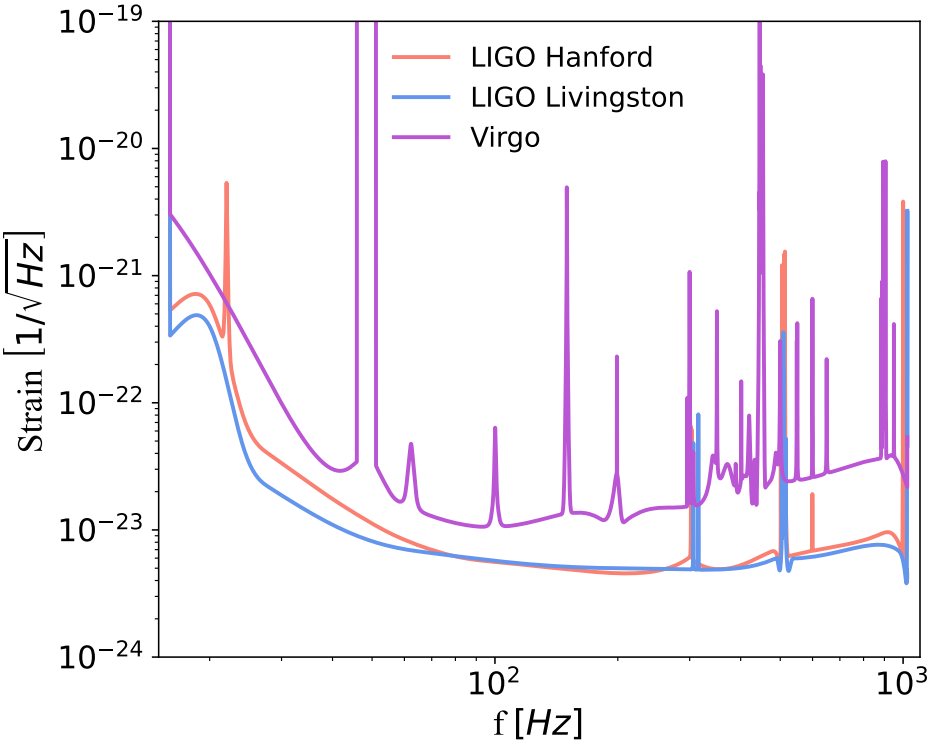

Figure 3.1: Amplitude spectral density of the three interferometers' strain sensitivity: LIGO Livingston, LIGO Hanford, Virgo. The sensitivity curves were computed in *O3b* and used in LVK GWTC-3 analyses [9] and the analysis of GW200129 in Ref. [3]. The square of the amplitude spectral density gives the power spectral density of the detectors.

In our parameter estimation analysis, we have chosen to use a flat prior over spin magnitude, the cosine of the tilt angle and the component masses. The parameter estimation results can be significantly affected by the selected priors of the spin magnitudes and the tilt angles. Since there is no evident justification for employing a prior from the observed population or one motivated by other astrophysical factors, we have selected these particular priors that do not introduce strong assumptions about the underlying astrophysical population. These are the default priors that were also used in Refs. [9, 3]. Furthermore, the prior parameter space has been adjusted to not exceed significantly the validity range of the surrogate model, setting the total mass to

be $M \geq 68M_{\odot}$, the chirp mass to be within $14.5M_{\odot}$ and $49M_{\odot}$ and the mass ratio to be less than $1:4$ or $1:6$ depending on the configuration. We chose the minimum frequency where the analysis starts to be 20 Hz. The `NRSur7dq4` waveforms were generated with starting time that corresponds to 11 Hz for the $(\ell = 2, |m| = 2)$ multipole, to ensure that the highest-frequency multipoles, $(\ell = 3, |m| = 3)$, also start below 20 Hz.

In the case of the `NRSur7dq4` injections, the data were all injected with an SNR of 100 and start at 20 Hz using the same basic setup as the *O3b* catalog [9]. For their sky location, the declination is $\delta = 1.4323$ rads and right ascension $\alpha = 0.2896$ rads, while the polarisation is set to $\psi = 1.4$ rads. Each production run produced approximately $\sim 10^5$ samples. Considering that for standard applications of the `LALInference` sampler 10^4 is a typical amount of samples, we are confident that 10^5 samples is a sufficient number. However, to further ensure the convergence of each run we took into account the behaviour of the autocorrelation function and the value of the Gelman-Rubin diagnostic [129].

The `NRSur7dq4` data are injected in zero-noise meaning that the detector noise is set to zero while the power spectral densities of the detectors (see Fig. 3.1) are used to compute the likelihood. In the zero-noise injection, the noise is removed, but the parameter estimation analysis is performed with the relative frequency-dependent sensitivity (noise curve) that corresponds to each detector and for sky location, orientation and polarisation values appropriately also adjusted to the detectors allowing the computation of an SNR. We can interpret the results obtained from this type of injection as an average over many Gaussian noise realisations.

In Section 2.7, we explained that the Gaussian likelihood [101] is given by the noise-weighted inner product [100]

$$\log \mathcal{L} \propto -\frac{1}{2}\langle d(t) - h_M(\theta) | d(t) - h_M(\theta)\rangle, \tag{3.3}$$

where $h_M(\theta)$ is the waveform model evaluated at θ and $d(t)$ is the data given as the sum of the signal $s(t)$ and $n(t)$ the noise. For a zero-noise injection, since $n(t) = 0$, the data becomes $d(t) = s(t)$ and $\log \mathcal{L} \propto -\frac{1}{2}\langle s(t) - h_M(\theta) | s(t) - h_M(\theta)\rangle$. From the definition of the inner product between two waveforms h_1 and h_2 that is also given in Section 2.7

$$\langle h_1 | h_2 \rangle = 4Re \int_0^{\infty} \frac{h_1(f) h_2^*(f)}{S_n(f)} df, \tag{3.4}$$

where $S_n(f)$ is the power spectral density, it becomes clear that in the case of the zero-noise injections, the frequency-dependent sensitivity of the detectors is used in the calculation of the likelihood. From the definition of the log likelihood, we note that if the model produces a waveform $h_M(\theta)$ that matches well the signal $s(t)$, the log likelihood $|\log \mathcal{L}|$ has a lower value.

In the case of the GW200129 de-glitched data, the parameter estimation analysis is performed using the same settings as those employed in LVK GWTC-3 analysis [9], while also applying the additional settings described in Ref. [3] such as reducing the prior parameter space to fit within the validity range of the `NRSur7dq4`. For our analysis the waveform is generated at 20 Hz and we have included all the $l \leq 3$ spin-weighted spherical-harmonic multipoles.

3.3.1 NRSur7dq4 theoretical waveforms

In the first part of this work, we use the `NRSur7dq4` waveform model to investigate how the absence of the multipole asymmetry from the model affects the measured parameters for a number of theoretical signals of strongly precessing binaries with high SNR. Furthermore, we consider specific configurations that allow us to explore how the introduced biases depend on the recoil velocity of the final black hole, the inclination of the system, the magnitude of the primary black hole's spin and the mass ratio of the binary. In each of these cases the signal is generated from the full `NRSur7dq4` waveform model, and the parameter recovery uses the `NRSur7dq4` and `NRSur7dq4_sym` models. We also note that our study is limited to single-spin systems; the phenomenology is likely to be more complex in two-spin configurations.

The dependency on the recoil velocity and the inclination is tested by injecting a series of waveforms to study how two extreme recoil values and different inclinations affect the parameter estimation results. To achieve this, we employed the full `NRSur7dq4` waveform model to generate two theoretical signals with different in-plane spin orientations that correspond to a maximum and a minimum recoil velocity while also varying the inclination of the system from face-on to edge-on. These two `NRSur7dq4` waveforms differ only by the orientation of their spins.

To ensure the highest accuracy with the `NRSur7dq4` model, we have selected the binaries' parameters to be within the validity range of the model. The analysis is done with two theoretical signals that have the same mass ratio,

$q = 2$, and a large primary spin of magnitude $a_1/m_1 = 0.7$ that lies in the plane creating a strongly precessing system. The asymmetric masses of the binaries ensure the better measurement of the spins and the inclination of the systems. In cases where the masses are not equal, the precession effects on the waveforms are more pronounced and the contributions from higher multiples are heightened.

We selected a total mass of $M = 100M_{\odot}$ for both binaries, which falls within the range of total masses that have been observed. To achieve a stronger signal at merger and increase the impact of the multipole asymmetry, we opted for a large total mass that still falls within the validity range of the `NRSur7dq4` model. To ensure the observation of the biases that arise when the asymmetry is neglected, we utilized previous findings from Refs. [126, 127] and chose a high SNR of 100. Although this SNR value exceeds the SNR of the signals we expect to detect in the near future, these strong signals enable the measurement of the spin magnitude and tilt angle, and the clear observation of the biases they exhibit.

For the study of the recoil dependency, to clearly demonstrate the impact that the recoil velocity may have on the measurement of the binaries' parameters, we chose the lowest and the highest possible recoil velocity for a configuration with the above characteristics. Since the recoil velocity of the remnant black hole depends on the direction of the in-plane spin, we found the appropriate in-plane spin directions that correspond to a maximum and a minimum recoil velocity.

This was achieved by computing the recoil velocities for `NRSur7dq4` theoretical waveforms with varying in-plane spin directions of the binaries between 0° and 180°. The in-plane spin direction is denoted by the the misalignment angle ϕ_{Sn} between the black holes' separation vector, $\hat{n}$, and the projection of the spin vector $\hat{S}$ on the orbital plane, at the starting frequency. The waveforms were generated in the inertial $\mathbf{L_0}$-frame where $\hat{\mathbf{L}} = \hat{\mathbf{z}}$ at a reference time, satisfying `LAL` conventions using the `LALSimulation` function `SimInspiralChooseTDModes` [128, 130]. The recoil velocity was computed from the waveform multipoles [131] in the final $\mathbf{J}$-frame where the z-axis is parallel to the total angular momentum, $\mathbf{J}$, of the remnant black hole. Fig. 3.2 shows the measured recoil velocities for different ϕ_{Sn} angles. As we expected for a misaligned-spin system the value of the minimum recoil velocity is not zero due to the presence of in-plane recoil. This has also been observed for

aligned-spin binaries, but the minimum recoil velocity will have a lower value in those systems [62]. Based on these results, the lowest recoil velocity is $v_{f_{\rm min}} = 236\,{\rm km/s}$ and the highest is $v_{f_{\rm max}} = 1461\,{\rm km/s}$. For these two cases the initial in-plane-spin directions ϕ_{Sn} are, respectively, 67° and 138°.

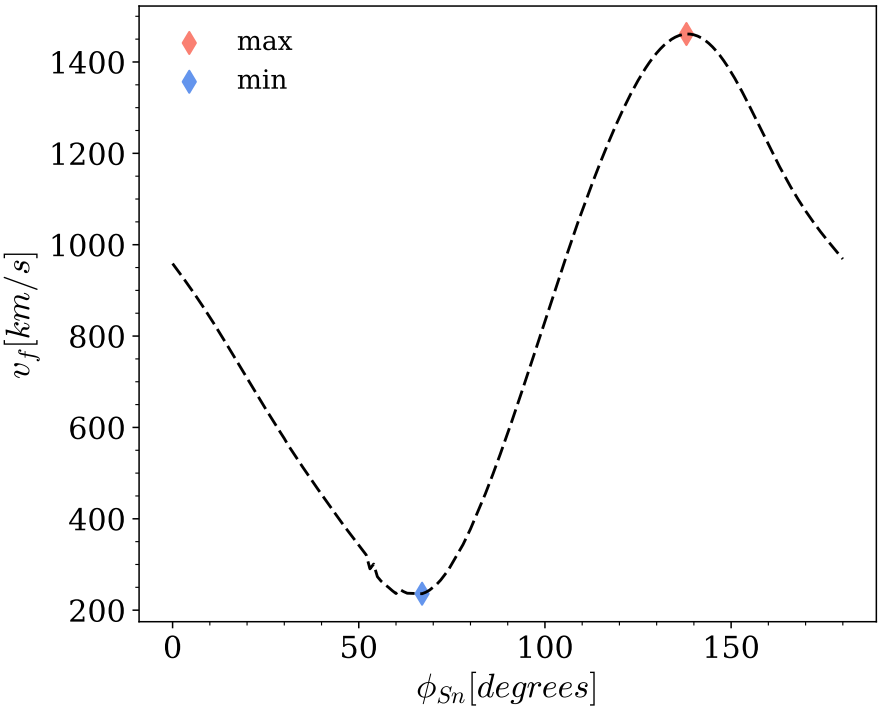

Figure 3.2: The minimum (blue) and maximum (red) recoil velocity values and the corresponding in-plane spin direction angles that were selected for this study.

Furthermore, to increase the effects of the asymmetry, we have ensured that the asymmetry is beamed along the z-axis when it peaks during merger. To achieve this we first rotate the waveforms from the $\mathbf{L_0}$-frame to the $\mathbf{J}$-frame and finally to the quadrupole-aligned frame that tracks the direction of the maximum radiation emission [42]. Then by adding in quadrature the $\ell = 2$ multipoles of the waveform's strain in the co-precessing frame, we compute the time that maximises the sum to *define* a notion of merger time, t_m. We then computed at this peak time the Euler angles, $\alpha(t_m), \beta(t_m), \gamma(t_m)$, that would allow the rotation from the $\mathbf{L_0}$-frame to the co-precessing frame. These set of angles allowed us to rotate the minimum and maximum recoil waveforms from the $\mathbf{L_0}$-frame to a frame where the maximum emission is along the z-axis at this approximate merger time, t_m. This ensured that the anti-symmetric contribution to the signal is beamed along the z-axis when it peaks at the

merger.

In general the binary inclination, ι, is defined as the direction of the observer relative to the orbital angular momentum, $\mathbf{L}_0$, at the frequency when the signal enters the detector's sensitivity band. Since $\mathbf{L}$ precesses during inspiral, this definition describes the orientation of the orbital plane to the observer at only one moment. In the case of precessing systems the effects of precession generally become stronger with inclinations $\iota \sim 90°$. Due to the use of the previously described frame in the case of the minimum and maximum recoil `NRSur7dq4` waveforms, we define the binary inclination relevant to the direction of maximum power in the antisymmetric contribution to the signal at merger. As a result, $\iota = 0^o$ corresponds to an inclination where the maximum emission direction is along the z-axis at merger and the other inclinations are relative to that. To ensure this, we prevented `LAL` from performing a frame rotation by artificially setting $\hat{\mathbf{L}}$ to be along the z-axis in the waveform metadata. The two `NRSur7dq4` waveforms were injected with different inclinations, varying from 0° to 90°. This allowed us to investigate how the inclination of the detected system affects the biases that the asymmetry's absence may introduce in the parameter estimation results. However, the fact that ι varies throughout the inspiral can create a more complicated picture in our measurements.

In addition, to test how the `NRSur7dq4_sym` model behaves for different mass ratios and spin magnitudes, we performed two additional injections. The selected configurations for that purpose are a binary black hole configuration with mass ratio $q = 2$ and a smaller in-plane spin of magnitude $a_1/m_1 = 0.4$, and a binary with a higher mass ratio $q = 4$ and slightly higher in-plane spin of magnitude $a_1/m_1 = 0.8$. In these last two cases, the in-plane spin direction is $\phi_{Sn} = 0°$ and the total mass of these binary is $M = 100M_\odot$. The selected inclination is $\iota = 60°$ and they are both injected at SNR 100. For these additional injections we use the standard `LAL` definition of inclination.

3.3.2 GW200129 gravitational wave signal

In the second part of this work, we consider the GW200129 gravitational wave signal that was first reported in Ref. [132]. Ref. [3] presented strong evidence that GW200129 was the first GW observation of a precessing binary, with masses $m_1 = 39M_\odot$ and $m_2 = 22M_\odot$, and the primary black hole rapidly spinning with $a_1/m_1 = 0.9$, and the spin lying almost entirely in the orbital plane. The measured parameters of the signal calculated with the `NRSur7dq4`

are displayed in Table 1 of Ref. [3]. The total total network SNR of GW200129 is 26.5 and the SNR in each detector were measured to be 14.6 in Hanford, 21.2 in Livingston and 6.3 in Virgo. Ref. [2] also showed that the GW200129 has a large recoil velocity of $v_f = 1542km/s$, which suggests that the anti-symmetric contribution to the signal was measurable and could significantly influence the parameter estimates.

The measurement of precession is expected to be more frequent in the next observing runs when the detection of signals with higher SNR will be possible. However, these measurements are extremely rare with the current sensitivity of the detectors. We know that the multipole asymmetry effects will be more significant for strongly precessing systems. Therefore, this system is considered to be of great interest for this study as it is a strongly precessing system indicating the presence of strong multipole asymmetry effects. Obtaining the recovered parameters with the two versions of the surrogate gives us the opportunity to understand how a model that contains only the symmetric counterpart will perform at the detection of a precessing signal. As noted in Sec. 3.3, besides the change in the model used in the analysis, all other settings are the same as in the analysis reported in Ref. [3].

3.4 Results

We have investigated the effects of the multipole asymmetry absence from the waveform models by injecting full surrogate waveforms and recovering their source parameters with the two versions of the model, the full and the symmetric `NRSur7dq4`. We have considered a number of injected waveforms with different inclinations $\iota \in [0^o, 30^o, 60^o, 90^o]$, mass ratios $q \in [2, 4]$, spins $a_1/m_1 \in [0.4, 0.7, 0.8]$ and two different spin orientations that correspond to the maximum and minimum recoil velocities. These are all strongly precessing systems that we injected at SNR 100 to maximise the effects of the asymmetry. We present the parameter estimation results of some of these cases and we show the impact that the absence of the multipole asymmetry has on the parameter estimation results for each of these systems. We have also tested the effects of the multipole asymmetry absence in the case of the highly precessing GW200129 signal.

3.4.1 The impact of the anti-symmetric contribution

One case that demonstrates well the results of this study is the single-spin precessing system ($q = 2, a_1/m_1 = 0.7, \theta_{\rm LS} = 90°$) described in Section 3.3.1. This is a black hole system with total mass $M = 100$ and the ϕ_{Sn} angle that corresponds to the minimum recoil velocity. The inclination of this selected system is $\iota = 30^o$ and it is injected at SNR 100.

In Figs. 3.8a - 3.10a, we present the posterior distributions for the $\chi_{\rm eff}$, the mass ratio q and the total mass M. The measured values are only slightly affected by the symmetric approximation in `NRSur7dq4_sym`. Nonetheless, we do see *some* bias; the true value of the mass and mass-ratio lies outside the 90% confidence interval. In several measurements shown here (and similarly in the other configurations we studied) there is a less clear sign of bias.

Furthermore, due to the high SNR of this signal, it should also be possible to measure the individual spins of the black holes. It is in these measurements where we find a bias. We observe that the symmetric model fails to measure accurately the dimensionless magnitudes and the tilt angles of the primary and the secondary black hole spins. The tilt angles of the primary and the secondary black hole spins, θ_{LS_1} and θ_{LS_2}, show the misalignment between the corresponding spin vector and the direction of the orbital angular momentum. A 0^o angle means that there is no misalignment and the black hole spins in the same direction as the binary black hole orbit while a 180^o angle indicates that the black hole spins in the opposite direction.

The two-dimensional posterior probabilities for the recovered spin magnitudes and tilt angles are presented in Fig. 3.3. In each disc plot, the spin magnitude is between 0 and 1 while the tilt angle is given by the central angle and ranges between 0^o and 180^o. The shading indicates the parameters' measured values and the different colors correspond to the results from the recovery with the two versions of the surrogate model.

In Fig. 3.3a, the recovered spin magnitude and the tilt angle of the primary black hole with the symmetric surrogate have a higher value indicating that the spin vector lies outside the plane of the binary. Furthermore, the recovered spin magnitude reaches the Kerr limit, $a_1/m_1 = 1$. In contrast, the measured parameters with the full surrogate agree well with the true values. A similar behaviour can be observed for a_2/m_2. The true spin of the secondary black hole is zero, as recovered well with the `NRSur7dq4` model. However, the `NRSur7dq4_sym` model measures a high spin value for the same black hole and

a low tilt angle, i.e., the spin appears nearly aligned with the orbital angular momentum.

Despite the significant biases in the spin measurements with the `NRSur7dq4_sym` model, the combination $\chi_{\rm eff}$ is measured correctly; the biases counteract so that $\chi_{\rm eff}$ has the correct value. We saw similar results in all of the consider configurations: the `NRSur7dq4_sym` recovery for a_1/m_1 and a_2/m_2 varied in magnitude and direction, but always such that $\chi_{\rm eff}$ was roughly correct. This is not surprising since we expect that the absence of the anti-symmetric contribution in a model will lead to biases in the spin measurements, but are less likely to bias parameters that are independent of the in-plane spin components, like the total mass, mass ratio, and aligned-spin combination $\chi_{\rm eff}$ that affects the inspiral rate [133, 134, 135], and therefore the overall binary phasing. Consequently, $\chi_{\rm eff}$ is likely to be measured well regardless of the multipole asymmetry, which has minimal, if any, effect on the rate of inspiral.

We might expect, however, that in larger-mass-ratio binaries with sufficiently high spin on the primary, that the spin measurements will rail against the Kerr limit, and it will not be possible for the biases to fully counteract each other to give a correct value of $\chi_{\rm eff}$. We will see examples of this in the next section.

3.4.2 Dependence on inclination, recoil, spin magnitude and mass ratio

To further investigate the effects that the absence of the multipole asymmetry has on the parameter estimations results, we test how the symmetric surrogate performs for different configurations.

As we explained previously, a system with strong asymmetry will have a high maximum recoil velocity. To investigate if there is a correlation between the recoil velocity and the biases that are introduced in the measurement of the source parameters from a symmetric model, we compare the results we obtained in the case we presented earlier to the results we obtain from a system that has a different recoil velocity. These two systems are almost identical and injected with the same inclination. They only differ by the in-plane spin direction of the spins. The spin direction of each system has been selected to maximise and to minimise the recoil velocity of the system.

Fig. 3.4 shows the measured spin magnitude and tilt angle of the binary

that has the maximum recoil velocity. In this case, we notice that the primary spin magnitude a_1/m_1 is now closer to the correct value, but the secondary spin magnitude a_2/m_2 shows a stronger preference for extreme spins. However, despite these small differences, qualitatively the results are similar. These similarities with the minimum recoil signal can also be noticed in Fig. 3.8b - 3.10b. Our results show that when investigating the dependency of the biases on the recoil velocity of the final black hole, the recovery with the symmetric model introduces similar biases in both cases. This behaviour was observed across all the cases we tested where the configurations were injected with different inclinations and the minimum and maximum possible recoil velocity for a system of this mass ratio and spin magnitude.

Although our initial expectation was that the importance of the anti-symmetric contribution's absent in parameter measurements would be large for cases with large recoil, and small for cases with small recoil, we see no clear indication that in the case of the minimum recoil `NRSur7dq4_sym` performs better. However, this can be explained if we consider that the signal's SNR depends on $|h|^2$ as observed at the detector (i.e., from one direction), while the recoil depends on $|\dot{h}|^2$ integrated over the entire sphere. There is therefore no reason to expect that a large recoil corresponds to a larger importance of the anti-symmetric contribution on the parameter measurements.

Furthermore, we investigate what happens when the inclination of the system is increased to 90^o and the binary is edge-on. The injected waveform in this case is identical to our main example case presented in Section 3.4.1 differing only by the inclination. From the results in Fig. 3.4, we see that the symmetric model fails to measure accurately the spins of the black holes. In the case of the primary black hole, the spin is recovered by the symmetric surrogate at a higher magnitude and lower tilt angle. For the secondary black hole where the spin magnitude is $a_2/m_2 = 0$, the symmetric surrogate recovers a different spin magnitude and tilt angle. Figs. 3.8c - 3.10c shows q, M and χ_{eff} for an inclination of $\iota = 90°$. In this case we do not see any clear sign of bias (similarly, we see slightly larger biases in $\iota = 0$ cases), which suggests that we may have removed the impact of the asymmetric contribution on these parameters.

This result differs from the obvious initial expectation that the asymmetry contributions would cancel out for edge-on systems. However, it can be understood if we consider that the power in the signal is dominated by the

symmetric part of the $(\ell = 2, |m| = 2)$ multipole in all of the cases we consider. Even when the signal is nominally edge-on, the majority of the signal power is in the plus polarisation, where the total power in the $(\ell = 2, |m| = 2)$ multipoles is comparable in face-on or face-off configurations. Since the overall amplitude of the anti-symmetric $(\ell = 2, |m| = 2)$ contribution is a ratio of the symmetric contribution that depends only on the intrinsic parameters of the binary, the fraction of the total power in the anti-symmetric contribution will be roughly the same regardless of the orientation. We therefore expect that any biases due to neglecting the anti-symmetric contribution will be of similar magnitude regardless of the binary's orientation, for fixed total SNR.

To further investigate these biases in the absence of the multipole asymmetry, we performed two additional NR injections that have different spin magnitude and mass ratio compared to the configuration presented in the previous section. The independence of the introduced biases from the value of the recoil velocity and the inclination of the binary allows us to compare these next cases with the ones we discussed in this section.

To test the effects that the spin magnitude of the primary black hole has on the introduced biases, we consider a lower-spin system, $(q = 2, a_1/m_1 = 0.4, \theta_{\rm LS} = 90^\circ)$. The waveform was injected with inclination $\iota = 60^o$ at SNR 100. In this case the multipole asymmetry is expected to be weaker compared to the previous configuration where the primary black hole had a more significant spin magnitude since the magnitude of the anti-symmetric contribution depends on the in-plane-spin magnitude. As a result, we expect the biases in the measurement of the spin magnitude and tilt angle to be more subtle.

In this case the magnitude and the tilt angle of the primary black hole are only slightly shifted away from the true value when recovered with the symmetric surrogate as can be seen in Fig. 3.6a. A similar behaviour is visible in Fig. 3.6b where the magnitude of the secondary black hole spin is shifted towards higher values. The posteriors for M, q and $\chi_{\rm eff}$ are wider in the analysis with the `NRSur7dq4_sym` model, but we still do not see any significant bias, except for a shoulder in the M posterior in one case. This is consistent with our expectation that a lower spin magnitude will also lower the impact of the multipole asymmetry.

Another case we consider is a system with larger mass ratio and larger spin, $(q = 4, a_1/m_1 = 0.8, \theta_{\rm LS} = 90^\circ)$ that is injected with inclination $\iota = 60^o$ at SNR 100. This case allows us to see how different mass ratios affect the

parameter estimation results when the multipole asymmetry is absent from the waveform models.

In this case the posteriors from the `NRSur7dq4_sym` recovery are much broader that for the `NRSur7dq4`, especially for the total mass, where the width of the 90% confidence region has almost doubled. We also see that there is now a clear bias in $\chi_{\rm eff}$ when recovering with the `NRSur7dq4_sym` model. Additionally, from Fig. 3.7, it now appears that the primary spin can be measured accurately with both models, suggesting that the spin imprint on the symmetric contribution to the signal is strong enough to constrain the value. This is not the case for the secondary spin, and without the anti-symmetric contribution to the model the secondary spin is biased. The bias in this sector of the model also appears to be so strong that it is no longer counteracted by the inspiral phasing that plays the dominant role in determining $\chi_{\rm eff}$, and so this is now also biassed. We expect that this is a general trend: at higher mass ratios ($q \gtrsim 4$) the measurement of the primary spin is more reliable than quantities that include both spins. Since there is a partial degeneracy between the mass ratio and $\chi_{\rm eff}$ [133, 134, 102], the bias in $\chi_{\rm eff}$ also leads to a bias in the mass ratio.

These results do also agree with the log likelihoods of the two models in 3.15e where the log likelihood of the `NRSur7dq4_sym` model is significantly lower compared to that of the `NRSur7dq4`. Comparing this plot with the other log likelihood posteriors shown in Fig. 3.15, we can see that this difference between the two posteriors is larger for the $(q = 4, a_1/m_1 = 0.8, \theta_{\rm LS} = 90°)$ configuration as we would expect considering that in this case although the spins were recovered more accurately, more parameters were affected introducing overall additional biases. However, it is also important to keep in mind for this comparison that the measured log likelihoods of Figs. 3.15a - 3.15c correspond to almost identical cases that differ either by spin orientation or inclination. On the other hand, the separate injections of the $(q = 2, a_1/m_1 = 0.4, \theta_{\rm LS} = 90°)$ and $(q = 4, a_1/m_1 = 0.8, \theta_{\rm LS} = 90°)$ waveforms employ a different definition of inclination and the waveforms were not generated using the same process described in Section 3.3.1.

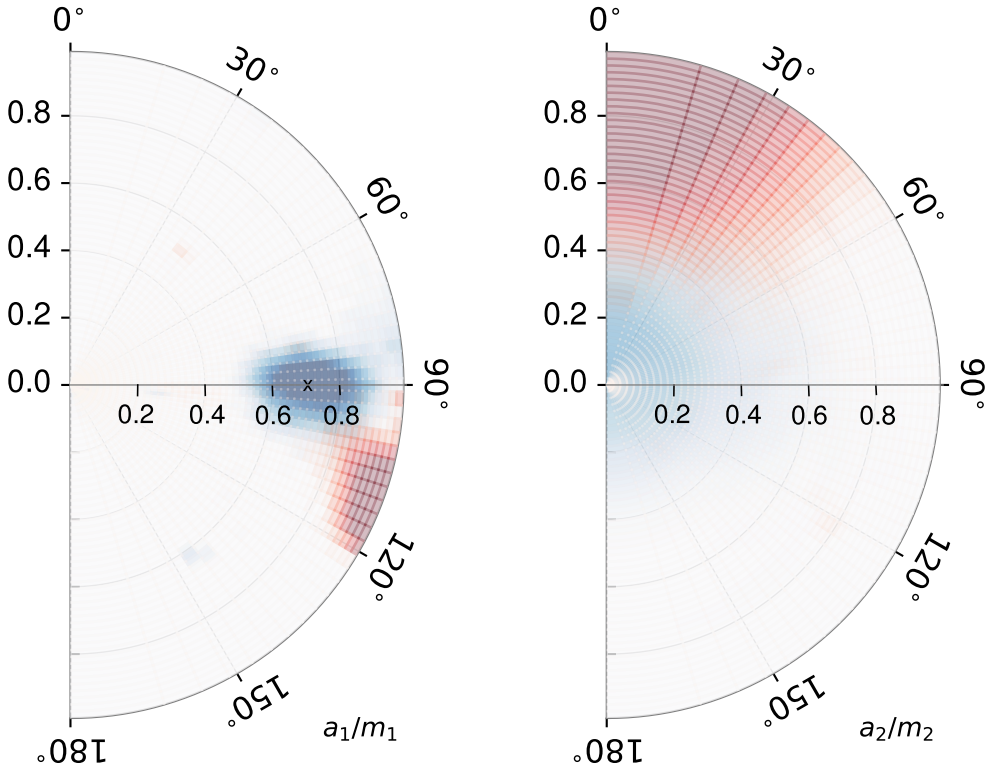

(a) (b)

Figure 3.3: Magnitude and direction of each spin, a_1/m_1 and a_2/m_2, for minimum recoil ($q = 2$, $a_1/m_1 = 0.7$, $\theta_{\rm LS} = 90°$) configuration at inclination $\iota = 30°$ as they were measured by the `NRSur7dq4` (blue) and `NRSur7dq4_sym` (red) models. The results indicate that the absence of the multipole asymmetry introduces biases in the measurement of the spins magnitudes and tilt angles.
(a) The measured dimensionless magnitude, a_1/m_1, and tilt angle, θ_{LS_1}, of the primary black hole. The true value is 0.7 for the magnitude and 90^o for the tilt angle. The two parameters are recovered well with `NRSur7dq4`. However, the measurements with the symmetric surrogate fail to recover correctly the same parameters. In this case, the results indicate that the primary black hole has a higher spin magnitude and tilt angle.
(b) The measured dimensionless magnitude, a_2/m_2, and tilt angle, θ_{LS_2}, of the secondary black hole. This is a single-spin system. The two parameters are recovered well with the full surrogate. However, the measurements with `NRSur7dq4_sym` fail to recover them correctly. In this case, the results indicate that the secondary black hole is spinning.

3.4.3 GW200129 signal

We now consider the gravitational-wave signal GW200129. The measured parameters presented in Refs. [132, 3] indicate that this system is similar to some of the injected `NRSur7dq4` waveforms that were discussed in the previous section. However, interestingly in this case the SNR is only 26.5 making this signal significantly weaker compared to the theoretical signals of the previous section that have a significantly higher SNR value. As a result, we expect the effects of the absence of the asymmetry to be more subtle.

The results were recovered using the `NRSur7dq4` and `NRSur7dq4_sym` models. As shown in Table 3.1, the total mass, M, is recovered well with the two version of the `NRSur7dq4`. However, the measurements of the mass ratio, q, and the individual masses, $m_{1,2}$, differ between the two models. The results presented in Fig. 3.16 show that the full model measures that this is an unequal-mass system while the measurement of the mass ratio with the symmetric model is not well constrained. Furthermore, the primary spin measurements presented in Fig. 3.16 show that the recovery with both versions of the surrogate led to similar results for the tilt angle. However, in the case of the primary spin magnitude, this is poorly constrained with the `NRSur7dq4_sym`, while it is clearly identified as a high spin by `NRSur7dq4`.

From these results it becomes evident that even at relatively low SNR, including the asymmetry in the model was essential in identifying this system as an unequal-mass binary with large in-plane spin. We note that in the LVK analyses of this signal, which used the `IMRPhenomXPHM` and `SEOBNRv4PHM` models, the `IMRPhenomXPHM` results showed some support for unequal masses and high spin. However, since this model does not include the multipole asymmetry, it is possible that the apparent measurement of a high primary spin was due to uncertainties in the waveform model (as suggested in Ref. [3]), and its partial agreement with the results from the more accurate and complete `NRSur7dq4` model may have been coincidental. To fully clarify these questions would require a more detailed study of the uncertainties of all three models in this region of parameter space, but since the `Phenom` and `SEOBNR` models have now both been superseded by upgraded versions [136, 137], these points may be moot. The broader and more important conclusion that we can draw from these results is that further improvement in symmetric models alone will not be sufficient to accurately measure the parameters of precessing systems, even at moderate SNRs; the inclusion of the multipole asymmetry is required in all

waveform models.

	Full	Symmetric
Primary mass, $m_1(M_\odot)$	$47.62^{+6.17}_{-8.88}$	$42.48^{+11.0}_{-4.94}$
Secondary mass, $m_2(M_\odot)$	$27.0^{+8.83}_{-4.96}$	$32.54^{+4.64}_{-9.73}$
Mass ratio, $q = m_2/m_1$	$0.57^{+0.36}_{-0.15}$	$0.77^{+0.21}_{-0.34}$
Total mass, $M = m_1 + m_2(M_\odot)$	$74.83^{+3.06}_{-3.07}$	$75.28^{+3.06}_{-3.27}$
Primary spin, a_1/m_1	$0.88^{+0.11}_{-0.45}$	$0.68^{+0.31}_{-0.58}$
Primary spin tilt angle, $cos\theta_{LS_1}$	$0.16^{+0.42}_{-0.36}$	$0.25^{+0.6}_{-0.72}$
χ_{eff}	$0.06^{+0.12}_{-0.12}$	$0.12^{+0.09}_{-0.14}$
χ_p	$0.85^{+0.13}_{-0.37}$	$0.66^{+0.31}_{-0.45}$

Table 3.1: The recovered parameters for the de-glitched GW200129 data with their 90% credible intervals. The results were recovered using the `NRSur7dq4` and `NRSur7dq4_sym` models.

3.5 Conclusion

We have presented the effects that neglecting the multipole asymmetry in the waveform modelling has on the measurements of the source parameters. We employed a series of theoretical waveforms and we tested the performamce of a symmetric version of the `NRSur7dq4` waveform model against the full `NRSur7dq4` model. Our results show that the absence of the multipole asymmetry from the waveform models introduces systematic errors in the case of strongly precessing systems with high SNR. We find strong evidence across all the considered configurations that at high SNR the absence of the multipole asymmetry from the waveform models introduces significant biases in the measurements of the spins and tilt angles of precessing binary systems.

Furthermore, we investigate how the introduced biases depend on the inclination of the binary, the primary spin magnitude and the mass ratio of the system. We also test their dependence on the recoil velocity of the final black hole by injecting two `NRSur7dq4` waveforms with two different in-plane spin directions that correspond to the maximum and minimum recoil. Our results show no evidence of dependence between the introduced biases and the recoil velocity or the inclination of the system. We find that the considered inclinations of $\iota \in [0^o, 30^o, 60^o, 90^o]$, have no significant impact on the biases even if the system is oriented from face-on to edge-on. Similarly, in the case of the maximum and minimum recoil value, the introduced biases remain overall

unaffected by these recoil extreme values.

In contrast, the biases introduced by the symmetric model are found to depend on the primary spin and the mass ratio of the system. We investigate these effects for configurations with two different primary spin values $a_1/m_1 = 0.4, 0.7$. Since the effects of the multipole asymmetry are weaker for lower spins, the introduced biases are more subtle in the analysis of the waveform with spin $a_1/m_1 = 0.4$. To test the dependency on the mass ratio, we considered waveforms with mass ratios $q = 2, 4$. In this case, the multipole asymmetry is stronger for the signal with the higher mass ratio $q = 4$. The introduced biases indicate that the symmetric waveform model tries to search for parameters to produce the waveform with the high mass ratio and fails to recover the true values of some of the parameters measuring less accurately the mass ratio, the $\chi_{\rm eff}$ parameter and the magnitude and tilt angle of the secondary black hole.

In this study, we have also considered the GW200129 signal which is the only detected precessing signal. This detection was particular interesting for this study as it can illustrate how the symmetric models perceive precessing systems. We find that the measurement of the source parameters is less accurate and the use of the symmetric waveform results in the introduction of biases.

These findings are significantly important for future detections of binary black hole systems when detectors' sensitivity will be further improved. In the next observing runs, we expect to observe more signals similar to GW200129 at higher SNR that could reach values greater than 50. In the case of precessing systems, these strong signals will allow the measurement of precession and the black holes' spins. However, employing symmetric waveforms for the analysis of these signals will lead to incorrect measurements. This could have a significant impact on population studies and the efforts to better understand the formation of the observed black holes that rely on the accurate measurement of the binary black hole parameters.

Although the asymmetry is currently modelled in `NRSur7dq4`, the accuracy of the model degrades outside of its validity range. Furthermore, to ensure the accuracy of the obtained parameter estimation results, the use of more than one independent waveform models during this process is vital. Therefore, our results show that it is essential to include the multipole asymmetry in the `Phenom` and the `SEOBNR` waveform models.

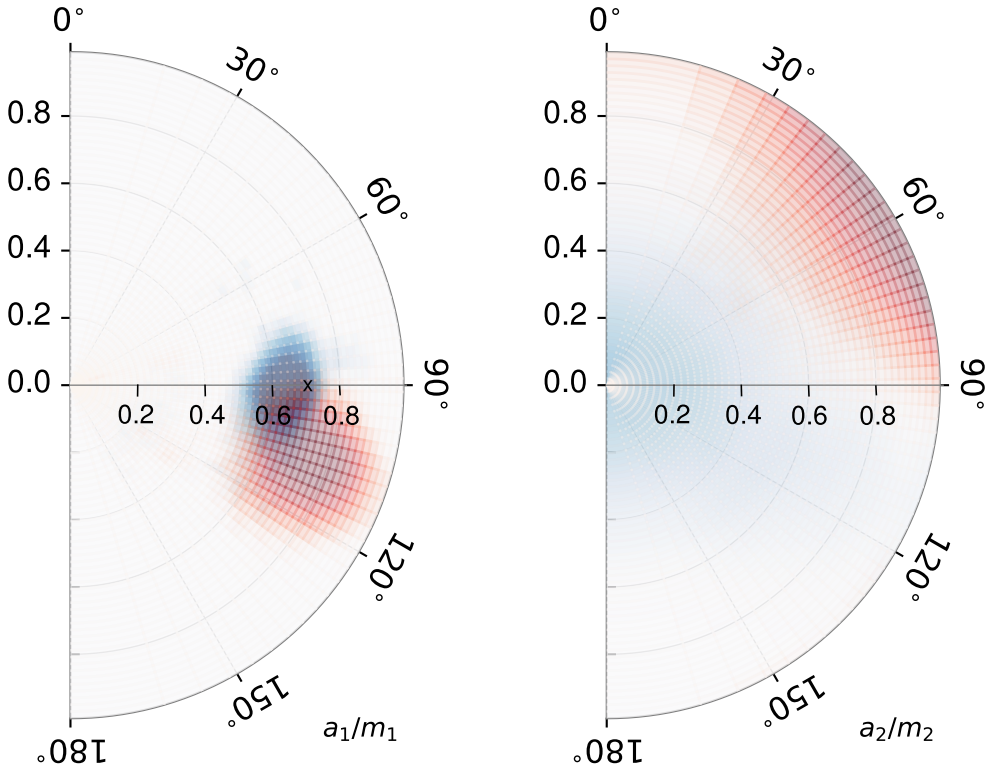

(a) (b)

Figure 3.4: Magnitude and direction of each spin, a_1/m_1 and a_2/m_2, for maximum recoil ($q = 2$, $a_1/m_1 = 0.7$, $\theta_{\rm LS} = 90°$) configuration at inclination $\iota = 30°$ as they were measured by the `NRSur7dq4` (blue) and `NRSur7dq4_sym` (red) models. The results indicate that the absence of the multipole asymmetry introduces biases in the measurement of the spins magnitudes and tilt angles. Comparing these results to the ones presented in Fig. 3.3, we observe that the introduced biases are not significantly affected by the in-plane spin direction.
(a) The measured dimensionless magnitude, a_1/m_1, and tilt angle, θ_{LS_1}, of the primary black hole. The true value is 0.7 for the magnitude and 90^o for the tilt angle. The two parameters are recovered well with the full surrogate. However, the measurements with the symmetric surrogate fail to recover correctly the same parameters. In this second case, the results indicate that the primary black hole has a slightly higher spin magnitude and tilt angle.
(b) The measured dimensionless magnitude, a_2/m_2, and tilt angle, θ_{LS_2}, of the secondary black hole. This is a single-spin system. The two parameters are recovered well with the full surrogate. However, the measurements with `NRSur7dq4_sym` fail to recover them correctly. In this second case, the results indicate that the secondary black hole has a high spin magnitude.

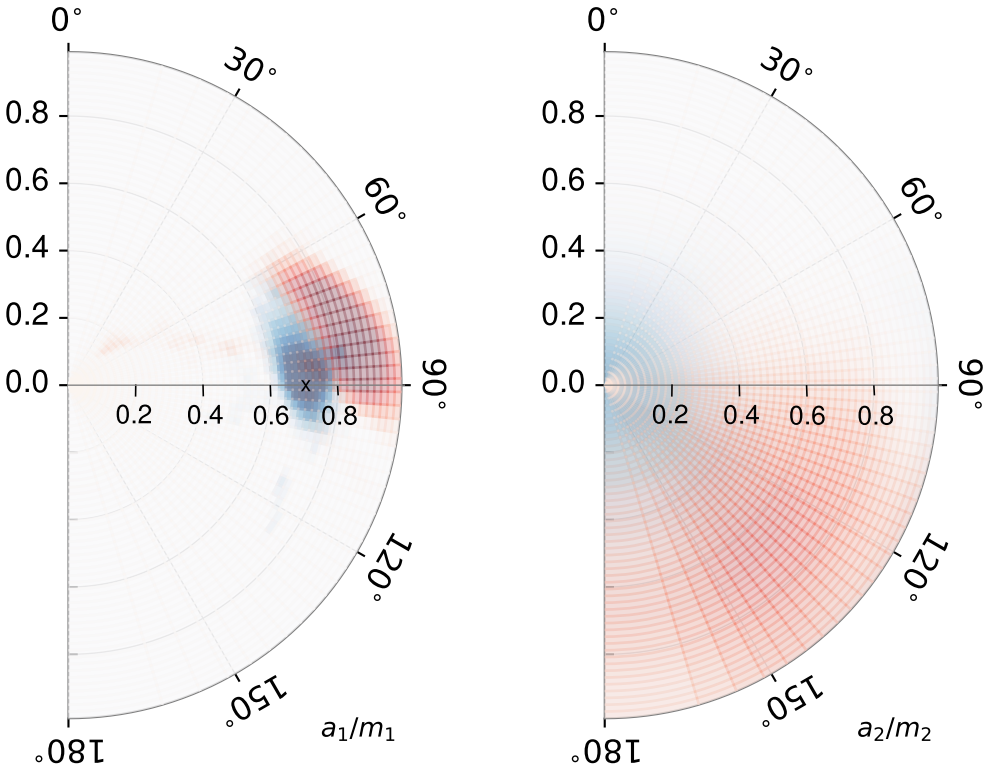

(a) (b)

Figure 3.5: Magnitude and direction of each spin, a_1/m_1 and a_2/m_2, for maximum recoil ($q = 2$, $a_1/m_1 = 0.7$, $\theta_{\rm LS} = 90°$) configuration at inclination $\iota = 90°$ as they were measured by the `NRSur7dq4` (blue) and `NRSur7dq4_sym` (red) models. The results indicate that the absence of the multipole asymmetry introduces biases in the measurement of the spins magnitudes and tilt angles. Comparing these results to the ones presented in Fig. 3.3, we observe no significant dependency between the introduced biases and the inclination of the binary black hole system.
(a) The measured dimensionless magnitude, a_1, and tilt angle, θ_1, of the primary black hole. The true value is 0.7 for the magnitude and 90^o for the tilt angle. The two parameters are recovered well with `NRSur7dq4`. However, the measurements with the symmetric surrogate fail to recover correctly the same parameters. In this case, the results indicate that the primary black hole has a higher spin magnitude.
(b) The measured dimensionless magnitude, a_2, and tilt angle, θ_2, of the secondary black hole. This is a single-spin system. The two parameters are recovered well with the full surrogate. However, the measurements with `NRSur7dq4_sym` fail to recover them correctly. In this case, the results indicate that the secondary black hole has a high spin magnitude and tilt angle.

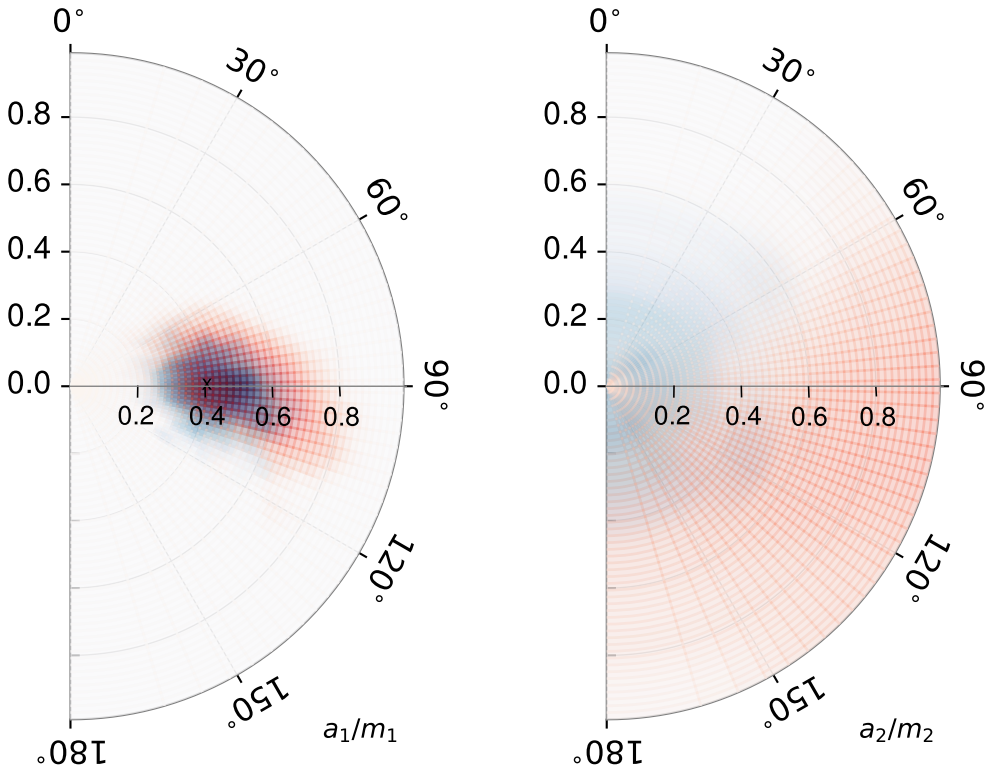

(a) (b)

Figure 3.6: Magnitude and direction of each spin, a_1/m_1 and a_2/m_2, for maximum recoil ($q = 2$, $a_1/m_1 = 0.4$, $\theta_{\rm LS} = 90°$) configuration at inclination $\iota = 60°$ as they were measured by the `NRSur7dq4` (blue) and `NRSur7dq4_sym` (red) models. The results indicate that the absence of the multipole asymmetry introduces some biases in the measurement of the spins magnitudes and tilt angles.
(a) The measured dimensionless magnitude, a_1, and tilt angle, θ_1, of the primary black hole. The true value is 0.4 for the magnitude and 90^o for the tilt angle. The two parameters are recovered well with both models and the measurements with the symmetric surrogate are only slightly shifted.
(b) The measured dimensionless magnitude, a_2, and tilt angle, θ_2, of the secondary black hole. This is a single-spin system. The two parameters are recovered well with the full surrogate. However, the measurements with `NRSur7dq4_sym` fail to recover them correctly. In this case, the results indicate that the secondary black hole is spinning.

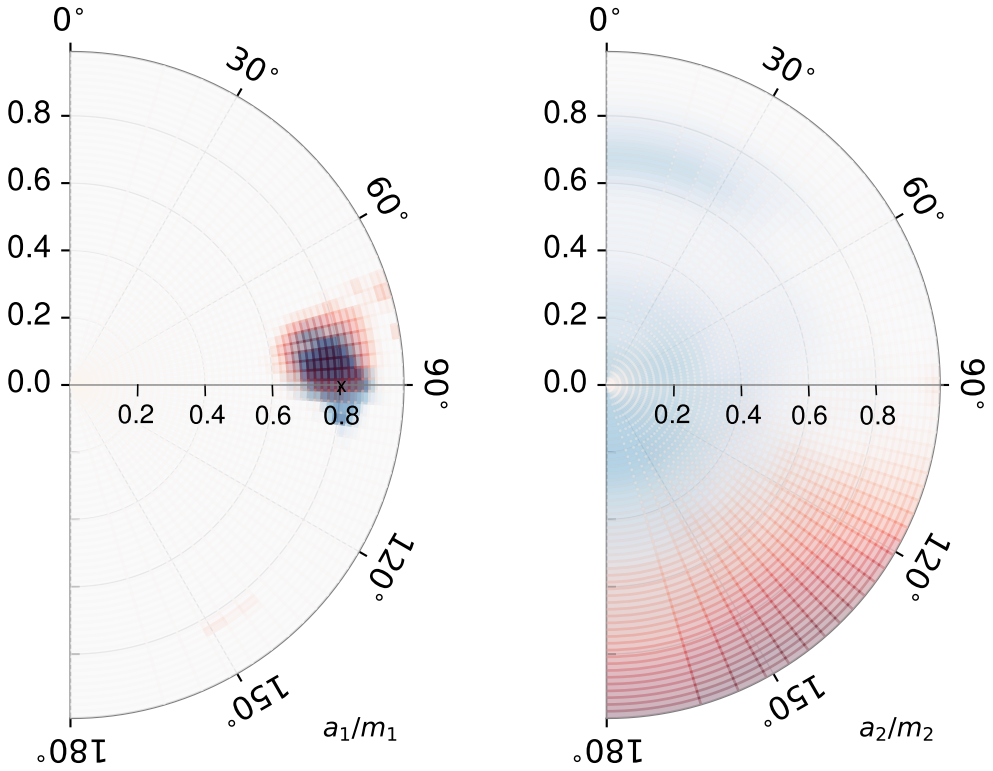

(a) (b)

Figure 3.7: Magnitude and direction of each spin, a_1/m_1 and a_2/m_2, for maximum recoil ($q = 4$, $a_1/m_1 = 0.8$, $\theta_{\rm LS} = 90°$) configuration at inclination $\iota = 60°$ as they were measured by the `NRSur7dq4` (blue) and `NRSur7dq4_sym` (red) models. The results indicate that the absence of the multipole asymmetry introduces some biases in the measurement of the spins magnitudes and tilt angles.
(a) The measured dimensionless magnitude, a_1, and tilt angle, θ_1, of the primary black hole. The true value is 0.8 for the magnitude and 90^o for the tilt angle. The two parameters are recovered relatively well with both models and the measurements with the symmetric surrogate are only slightly shifted.
(b) The measured dimensionless magnitude, a_2, and tilt angle, θ_2, of the secondary black hole. This is a single-spin system. The two parameters are recovered well with `NRSur7dq4`. However, the measurements with `NRSur7dq4_sym` fail to recover them correctly. In this case, the results indicate that the secondary black hole has a high spin that reaches the Kerr limit and a high tilt angle.

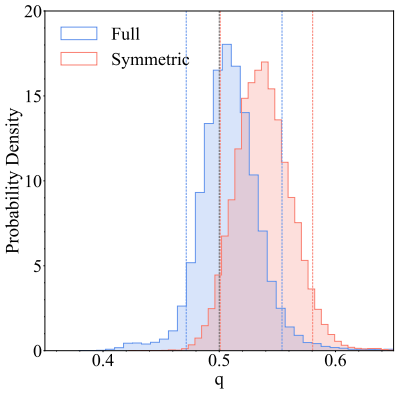

(a) q2a07t90p67, inclination 30

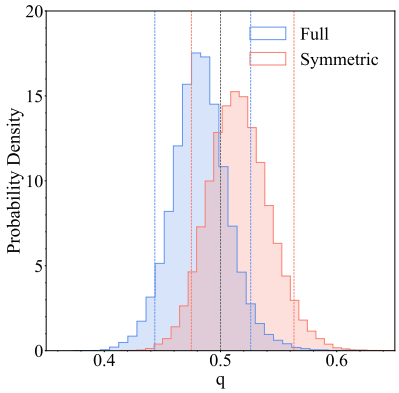

(b) q2a07t90p138, inclination 30

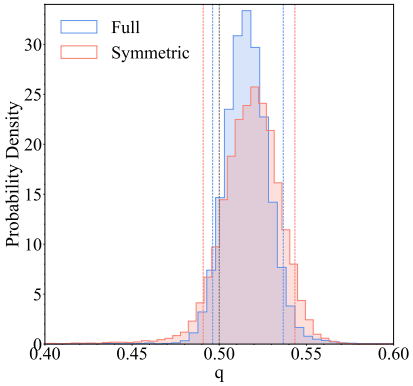

(c) q2a07t90p67, inclination 90

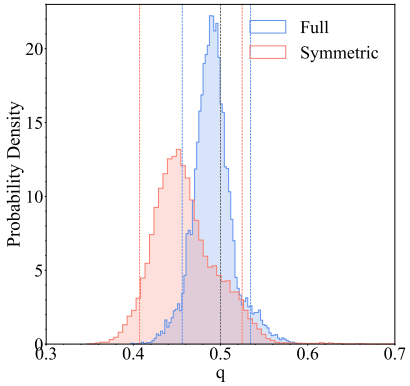

(d) q2a04t90p0, inclination 60

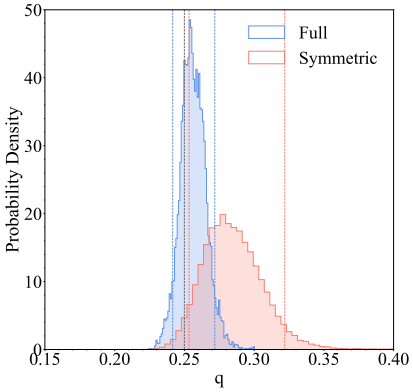

(e) q4a08t90p0, inclination 60

Figure 3.8: **Comparison between the results from the full surrogate model and those from the symmetric surrogate.** One-dimensional posterior distributions for the mass ratio of the binary black hole system.

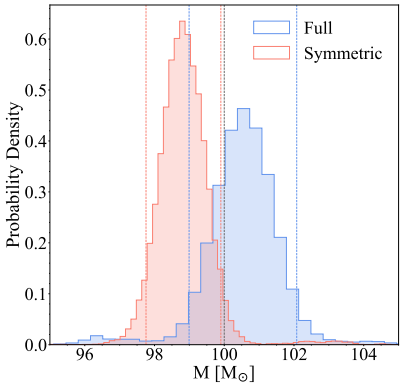

(a) q2a07t90p67, inclination 30

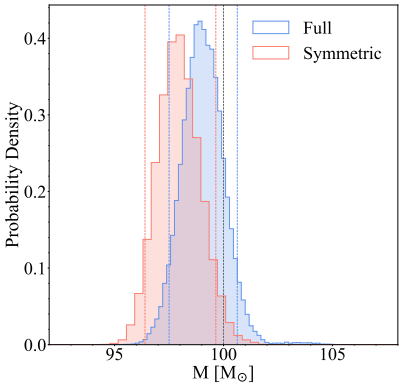

(b) q2a07t90p138, inclination 30

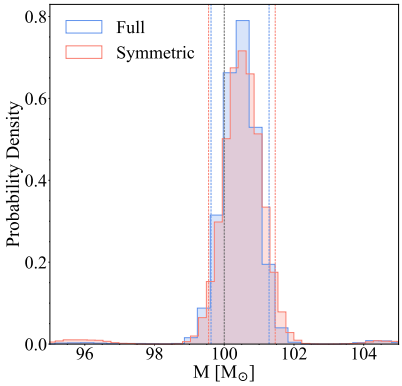

(c) q2a07t90p67, inclination 90

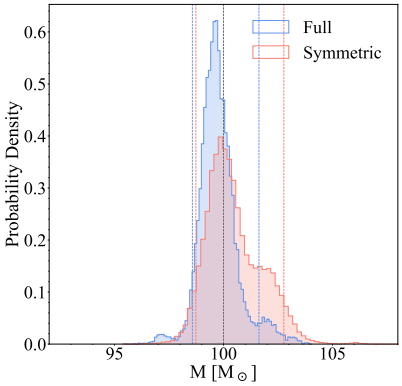

(d) q2a04t90p0, inclination 60

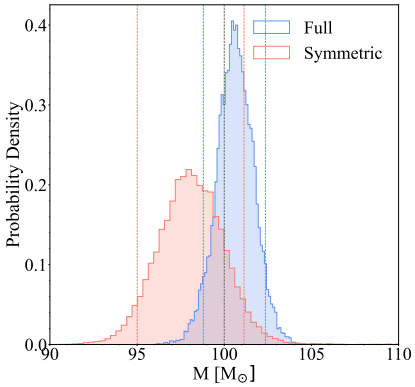

(e) q4a08t90p0, inclination 60

Figure 3.9: **Comparison between the results from the full surrogate model and those from the symmetric surrogate.** One-dimensional posterior distributions for the total mass of the binary black hole system.

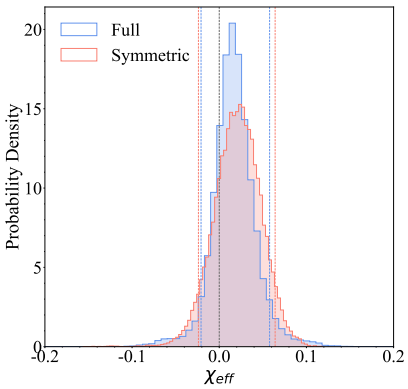

(a) q2a07t90p67, inclination 30

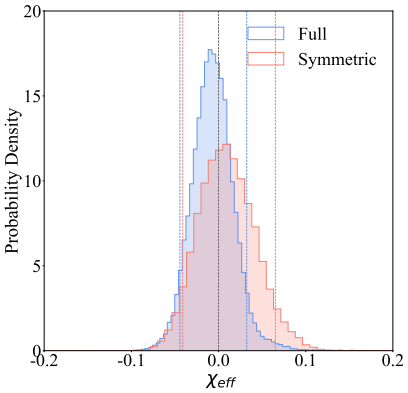

(b) q2a07t90p138, inclination 30

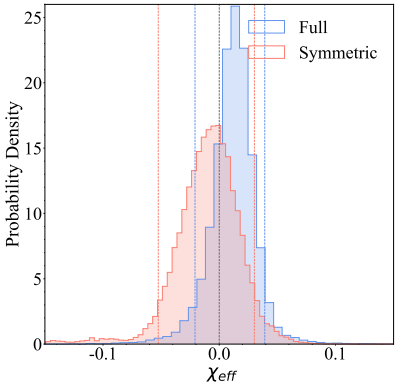

(c) q2a07t90p67, inclination 90

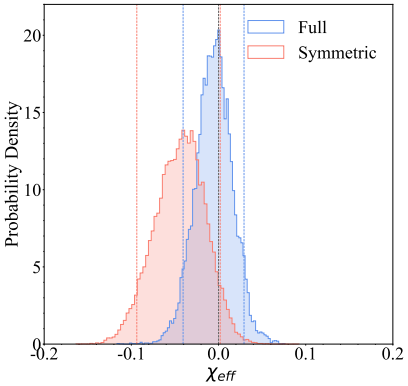

(d) q2a04t90p0, inclination 60

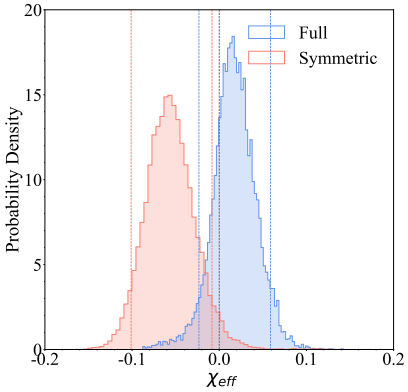

(e) q4a08t90p0, inclination 60

Figure 3.10: **Comparison between the results from the full surrogate model and those from the symmetric surrogate.** One-dimensional posterior distributions for the $\chi_{\rm eff}$ of the binary black hole system.

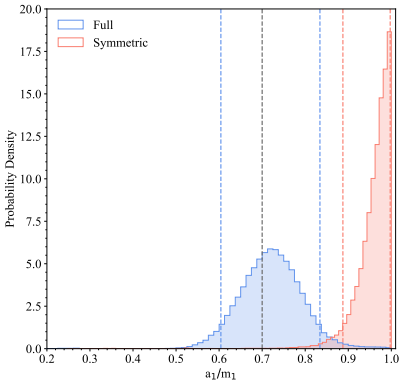

(a) q2a07t90p67, inclination 30

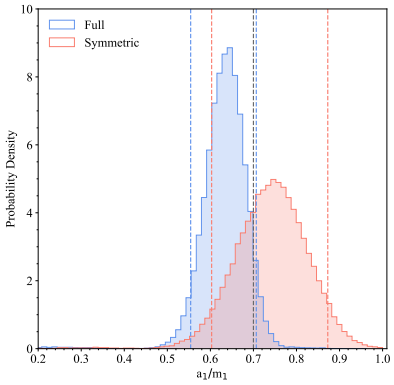

(b) q2a07t90p138, inclination 30

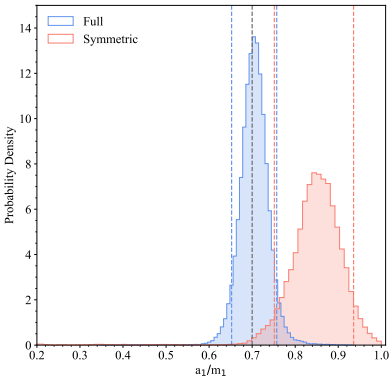

(c) q2a07t90p67, inclination 90

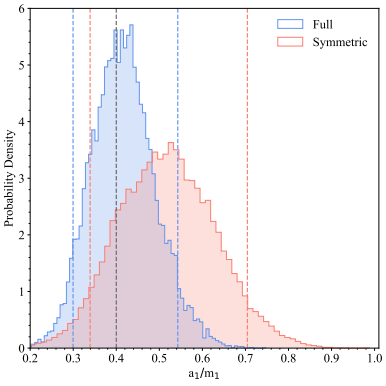

(d) q2a04t90p0, inclination 60

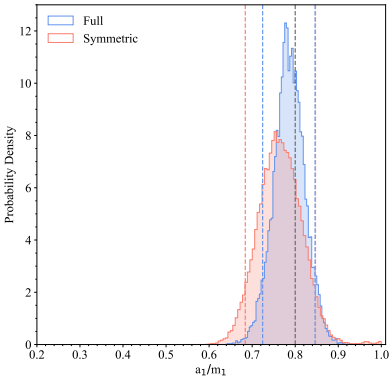

(e) q4a08t90p0, inclination 60

Figure 3.11: **Comparison between the results from the full surrogate model and those from the symmetric surrogate.** One-dimensional posterior distributions for the primary black hole's dimensionless spin a_1/m_1.

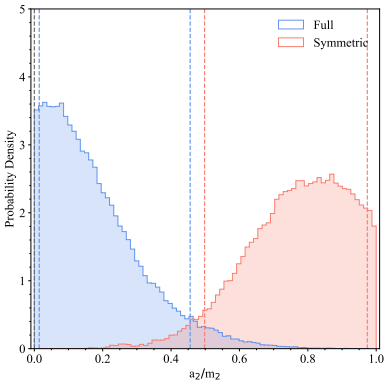

(a) q2a07t90p67, inclination 30

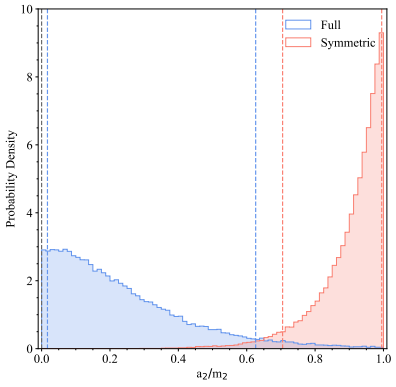

(b) q2a07t90p138, inclination 30

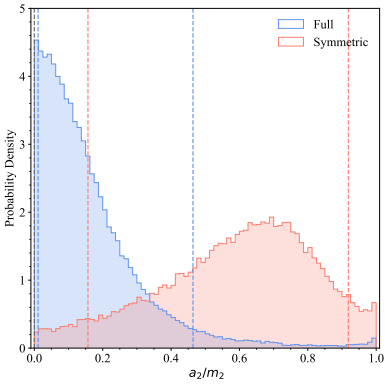

(c) q2a07t90p67, inclination 90

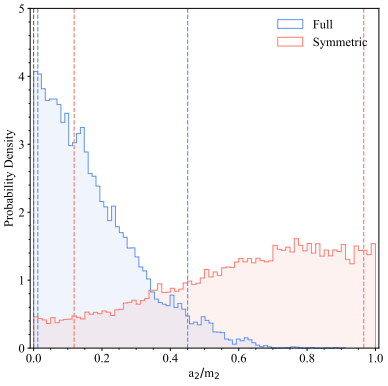

(d) q2a04t90p0, inclination 60

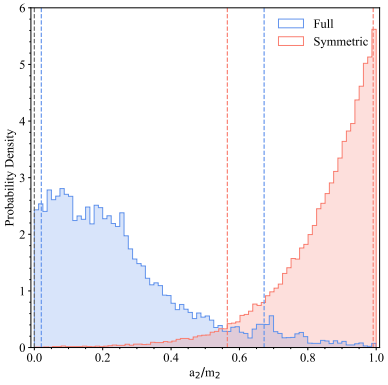

(e) q4a08t90p0, inclination 60

Figure 3.12: **Comparison between the results from the full surrogate model and those from the symmetric surrogate.** One-dimensional posterior distributions for the secondary black hole's dimensionless spin a_2/m_2.

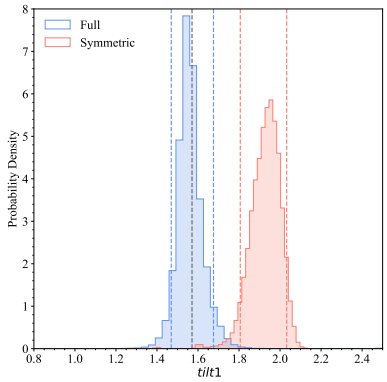

(a) q2a07t90p67, inclination 30

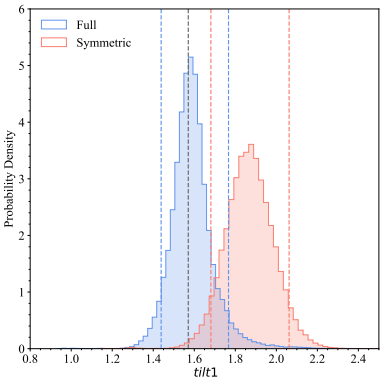

(b) q2a07t90p138, inclination 30

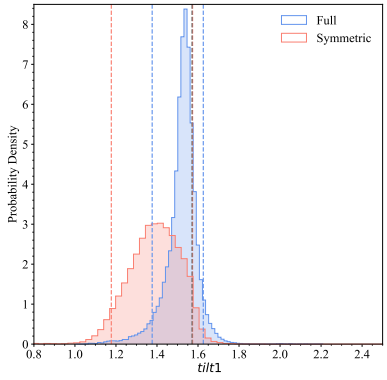

(c) q2a07t90p67, inclination 90

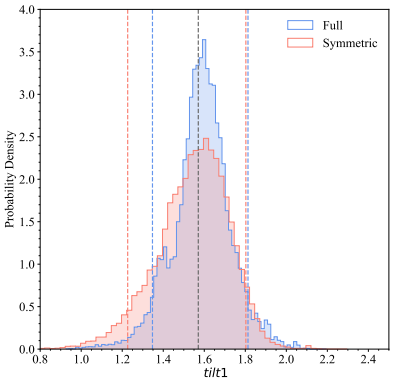

(d) q2a04t90p0, inclination 60

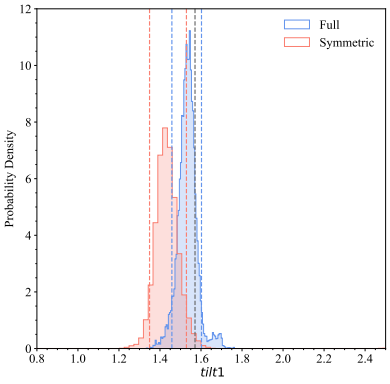

(e) q4a08t90p0, inclination 60

Figure 3.13: **Comparison between the results from the full surrogate model and those from the symmetric surrogate.** One-dimensional posterior distributions for tilt angle of the primary black hole's spin.

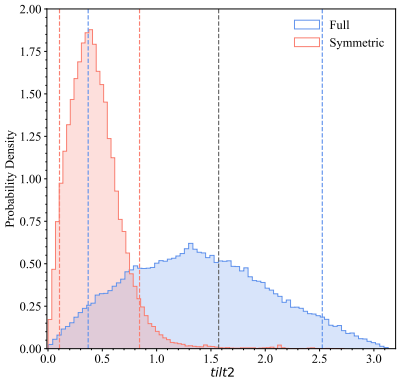

(a) q2a07t90p67, inclination 30

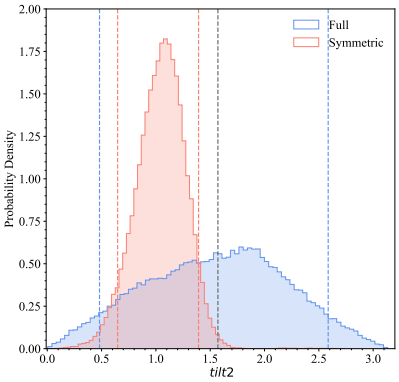

(b) q2a07t90p138, inclination 30

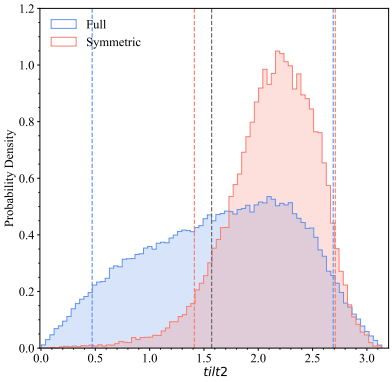

(c) q2a07t90p67, inclination 90

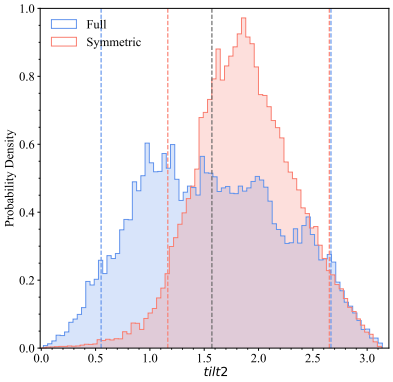

(d) q2a04t90p0, inclination 60

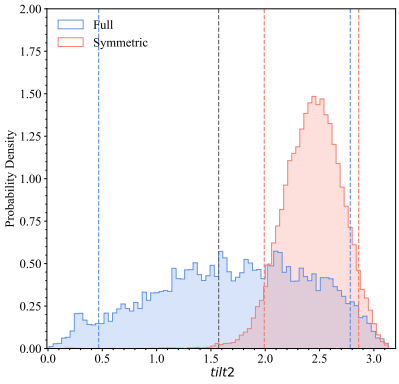

(e) q4a08t90p0, inclination 60

Figure 3.14: **Comparison between the results from the full surrogate model and those from the symmetric surrogate.** One-dimensional posterior distributions for tilt angle of the secondary black hole's spin.

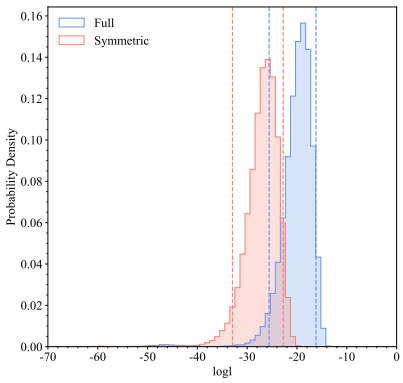

(a) q2a07t90p67, inclination 30

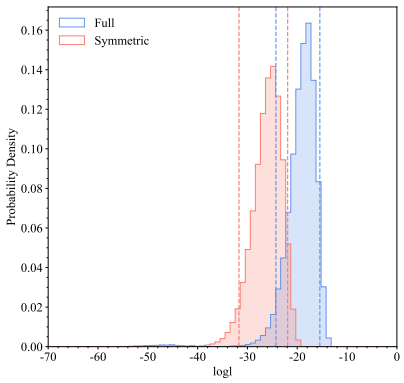

(b) q2a07t90p138, inclination 30

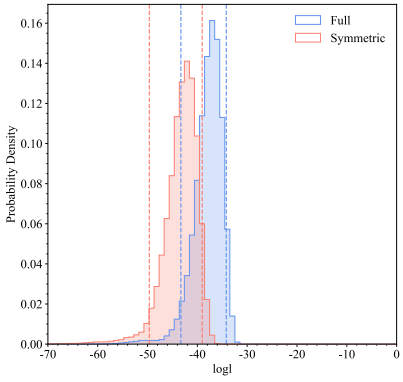

(c) q2a07t90p67, inclination 90

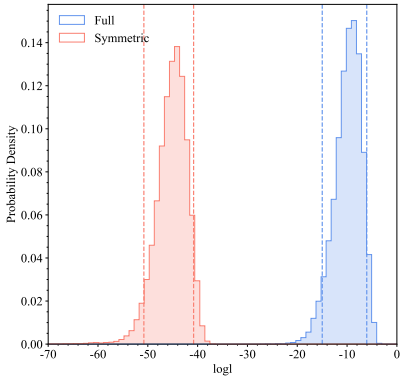

(d) q2a04t90p0, inclination 60

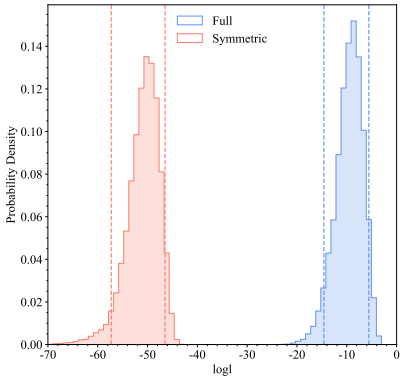

(e) q4a08t90p0, inclination 60

Figure 3.15: **Comparison between the results from the full surrogate model and those from the symmetric surrogate.** One-dimensional posterior distributions for the log likelihood.

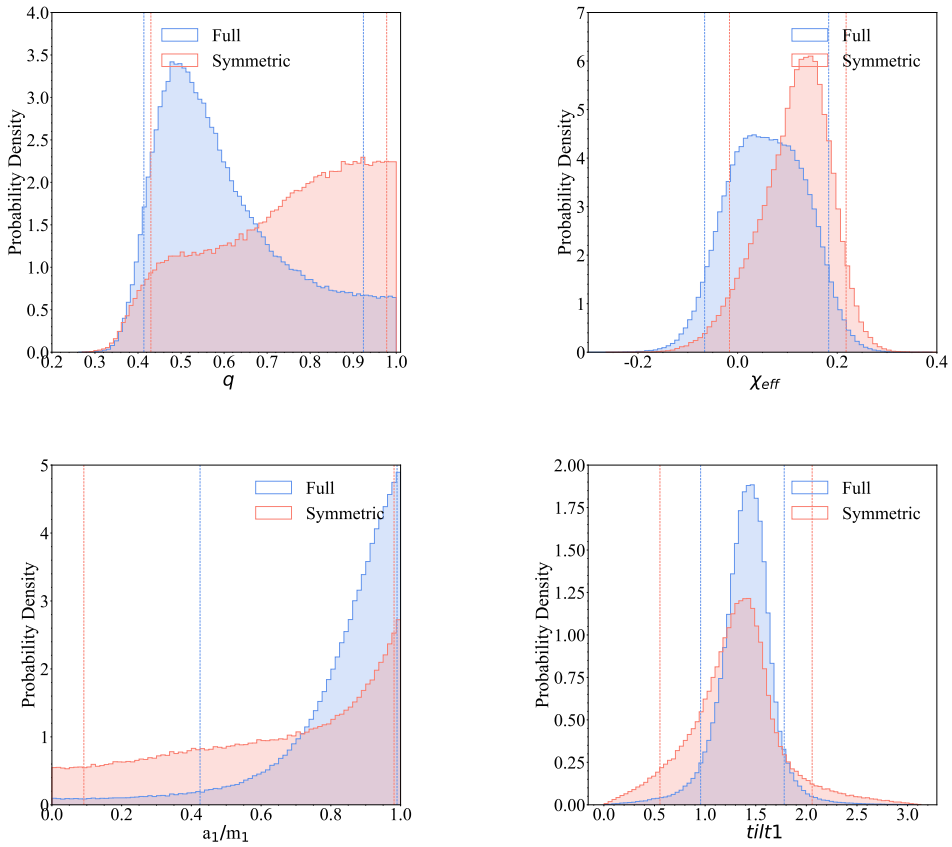

Figure 3.16: One-dimensional posterior distributions for the mass ratio, $\chi_{\rm eff}$, primary spin magnitude and tilt angle, for the `NRSur7dq4` (blue) and `NRSur7dq4_sym` (red) recovery of GW200129.

Chapter 4

A phenomenological model of the multipole asymmetry

4.1 Introduction

As shown in the previous chapter and discussed in Refs. [126, 127], neglecting the multipole asymmetry effects in the waveform models could introduce biases in the measurement of the binary black hole parameters at high SNR where we expect to measure precession and even at moderate SNR, as with GW200129. We found that the absence of the asymmetry introduces systematic errors in the measurement of the individual spins of the black holes in the case of loud precessing systems.

To date, the multipole asymmetry has only be modelled by the `NRSur7dq4` model [1] and has yet to be incorporated into the `Phenom` and `EOBNR` models. As we explain in the previous chapter the presence of the multipole asymmetry in the `NRSur7dq4` model is insufficient. This model has a narrow validity range compared to the other two model families and it cannot be used to measure the properties of signals with low total masses approximately below $66M_{\odot}$, or with mass ratios higher than 4. Furthermore, it is important to have more than one model that can verify the accuracy of the measured parameters. Therefore, we have concluded that the inclusion of the multipole asymmetry in the `Phenom` and `EOBNR` models is crucial.

In this chapter, we present the first phenomenological multipole asymmetry model. We have created a simple and efficient waveform model that captures accurately the behaviour of the anti-symmetric component. To model the amplitude and the phase of the multipole asymmetry we explored the typical

phenomenological approaches that have been widely employed in developing phenomenological models. However, a further study of the Post Newtonian expression of the anti-symmetric contribution led us to a simpler approach. We have produced a multipole asymmetry model where the anti-symmetric component of the waveform is estimated from the symmetric amplitude and phase and can in principle be applied to any frequency-domain model.

In Section 4.2.1 we explain the motivation behind our modelling approach. We explain the preparation of the NR data that we used to calibrate our model in Section 4.2.2. In Section 4.2.3 we look into the PN symmetric and antisymmetric contributions. We explain how we have utilised PN-NR hybrid waveforms and the construction of our ratio model in Section 4.2.4. The final amplitude model and the surface fit of its coefficient across the parameter space are presented in Sections 4.3 and 4.4, respectively. Finally, in Section 4.5, we present briefly the phase model of the anti-symmetric component and we discuss the outcome of this project in 4.7.

4.2 Structure of the model

In this section, we give a detailed description of the phenomenology of the anti-symmetric and symmetric contributions of the $\ell = |m| = 2$ multipoles and we discuss how the symmetric waveform can be used in the modelling of the multipole asymmetry. We will find that there is a simple way to model the multipole asymmetry using the symmetric contribution that is already present in the `Phenom` models.

4.2.1 Motivation for the multipole asymmetry model

In non-precessing systems where the spins are aligned with the orbital angular momentum, the symmetry between the waveform multipoles

$$h_{lm}(t) = (-1)^l h^*_{l-m}(t) \tag{4.1}$$

allows the computation of the $m < 0$ multipoles from the $m > 0$ multipoles and simplifies the construction of the waveform models. However, in binaries where the spins are randomly oriented Eq. 4.1 no longer applies. In the current `Phenom` and `EOBNR` waveform models the precessing binary waveforms are modelled by "twisting-up" an aligned-spin waveform model using a precession

dynamics model that has been developed separately [64, 68, 92, 74, 77, 76, 93]. In this process, the aligned-spin waveform model is regarded to be approximately the same as a precessing waveform in the co-precessing frame and is transformed to the inertial frame using the Euler angles obtained from the precession dynamics model [42, 49]. This approximation is possible since in the co-precessimg frame that tracks the precession, the precessing waveform exhibits a close resemblance to the corresponding non-precessing signal [42, 49, 68, 77, 64, 84]. However, in the co-precessing frame, the multipole asymmetry continues to be present and Eq. 4.1 does not hold. Thus, the "twisting-up" method that is employed to construct the `Phenom` and `EOBNR` models, excludes the multipole asymmetry from these waveform models.

We consider the $(\ell = 2, |m| = 2)$ multipoles in the co-precessing frame, and split them into their symmetric and anti-symmetric parts,

$$h^{CP}_{2,2}(f) = A_s(f)e^{i\phi_s(f)} + A_a(f)e^{i\phi_a(f)}, \tag{4.2}$$

$$h^{CP}_{2,-2}(f) = A_s(f)e^{-i\phi_s(f)} - A_a(f)e^{-i\phi_a(f)}. \tag{4.3}$$

The symmetric $(\ell = 2, |m| = 2)$ amplitude and phase, $A_s(f)$ and $\phi_s(f)$, are the amplitude and phase of the standard model that does not include multipole asymmetries. The symmetric and anti-symmetric contributions of the $\ell = |m| = 2$ multipoles in this frame are defined by

$$h^{CP,s}_{2,2} = \frac{1}{2}(h^{CP}_{2,2} + h^{*CP}_{2,-2}), \tag{4.4}$$

$$h^{CP,a}_{2,2} = \frac{1}{2}(h^{CP}_{2,2} - h^{*CP}_{2,-2}). \tag{4.5}$$

As is evident from the definition of the anti-symmetric component of the waveform, we are modelling a complex function. Therefore, we model separately in the co-precessing frame the amplitude and the phase of the anti-symmetric contribution. Similar to the other models of the `Phenom` family, we model the multipole asymmetry in the frequency domain.

Furthermore, in the construction of the multipole asymmetry model we focus solely on the asymmetry in the dominant $(\ell = 2, |m| = 2)$ multipoles. The $(\ell = 2, |m| = 2)$ multipole asymmetry is weaker compared to the corresponding symmetric contribution indicating that the asymmetry in the higher order multipoles will be considerably less significant. This is illustrated in Fig. 4.1 where the amplitudes of the $(\ell = 2, |m| = 2)$ and $(\ell = 3, |m| = 3)$ anti-symmetric

contributions are plotted along with the amplitudes of the $(\ell = 2, m = 2)$ and higher order multipoles for a binary with mass ratio $q = 2$, spin magnitude $\chi = 0.8$ and spin and orbital angular momentum misaligment $\theta_{SL} = 90^o$. From Fig. 4.1, it becomes apparent that the amplitude of the $(\ell = 2, |m| = 2)$ anti-symmetric component is comparable to the $(\ell = 3, m = 3)$ multipole, whereas the $(\ell = 3, |m| = 3)$ multipole asymmetry is comparable to the $(\ell = 5, m = 5)$ multipole. Since overall the power in the $(\ell = 3, m = 3)$ multipole is higher than for the $(\ell = 2, |m| = 2)$ multipole asymmetry, it is evident that the asymmetry is important if we also take into account that the $(\ell = 4, m = 4)$ multipole is included in the waveform models. Furthermore, considering that the `Phenom` models include higher order multipoles up to $\ell \leq 4$, we have not modelled the asymmetry in the higher multipoles [138, 92, 139].

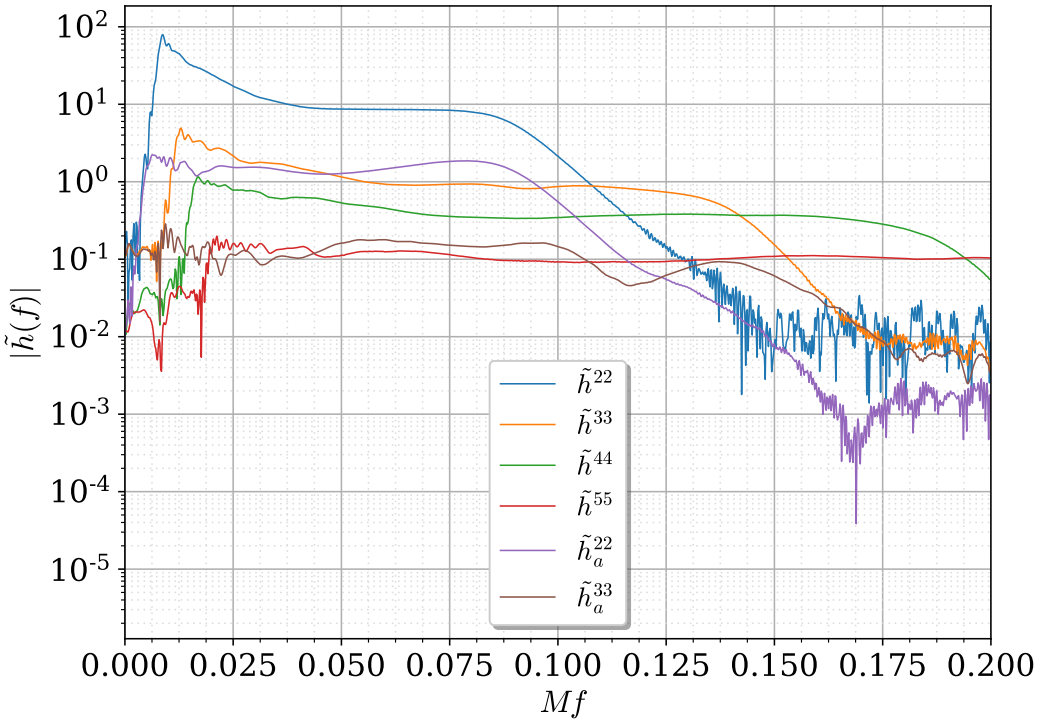

Figure 4.1: The $(\ell = 2, |m| = 2)$ and $(\ell = 3, |m| = 3)$ multipole asymmetry amplitudes in the frequency domain co-precessing frame against the $(\ell = 2, m = 2)$ and higher multipoles for the $(q = 2, \chi = 0.8, \theta_{SL} = 90^o)$. The amplitude of the $(\ell = 2, |m| = 2)$ anti-symmetric component, $\tilde{h}_a^{22}$, is comparable to the amplitude of the $(\ell = 3, m = 3)$ multipole, $\tilde{h}^{33}$. However, since the $(\ell = 3, m = 3)$ multipole extends to higher frequencies, overall the power in the $(\ell = 3, m = 3)$ multipole is higher than for the $(\ell = 2, |m| = 2)$ multipole asymmetry. The $(\ell = 3, |m| = 3)$ anti-symmetric component, $\tilde{h}_a^{33}$, is weaker and comparable to the $(\ell = 5, m = 5)$ multipole, $\tilde{h}^{55}$.

To understand better the phenomenology of the amplitude and phase of the multipole asymmetry and to explore potential new avenues for modelling it efficiently, we compute the leading-order symmetric and anti-symmetric contributions in PN theory. We consider a single-spin binary black hole system with masses $m_1 > m_2$. The dimensionless spin of the primary black hole lies in the orbital plane and is defined as $\chi = S_1/m_1^2$ where S_1 is the magnitude of the primary black hole's angular momentum.

The PN expressions for this system are computed from the expressions given in Ref. [37]. From the definitions of the symmetric and anti-symmetric spin quantities, χ_s and χ_a, in Ref. [37], we find that for a single-spin system $\chi_s = \chi_a = \chi/2$. In the source frame, the total angular momentum $\hat{\mathbf{J}}$ is along the z-axis and the instantaneous direction of the orbital angular momentum $\hat{\mathbf{L}}$ is given by the inclination angle of the orbital angular momentum relative to the total angular momentum, $\iota(t)$, and the $\alpha(t)$ is the angle between x-axis and the projection of the orbital angular momentum onto the x-y plane. The angle $\alpha(t)$ is the azimuthal precession angle of the orbital angular momentum $\hat{\mathbf{L}}$ around the total angular momentum $\hat{\mathbf{J}}$ as well as the azimuthal angle of the total in-plane spin χ. Then, by aligning the instantaneous orbital plane to coincide with the x-y plane, we can write the total in-plane spin as $\chi = \chi(\cos(\alpha), \sin(\alpha), 0)$.

To compute the symmetric and anti-symmetric contributions, we first obtain the h_{22} and h_{2-2} multipoles from Ref. [37]. The h_{22}^{PN} multipole is given in Eq. B1 of Ref. [37] and the h_{2-2}^{PN} multipole is computed from $\hat{h}_{22}^{PN}$, the normalized h_{22}^{PN} multipole by its leading order term, using the relations

$$\hat{h}_{lm}^{PN} = -\frac{h_{lm}^{PN}}{\frac{(2M\nu v^2)}{D_L}\sqrt{\frac{16\pi}{5}}e^{-im(\Psi+\alpha)}}, \tag{4.6}$$

$$\hat{h}_{l-m}^{PN}(\Psi) = (-1)^l \hat{h}_{lm}^{*PN}(\Psi+\pi) \tag{4.7}$$

from [37] where $\nu = m_1 m_2/M^2$ is the symmetric mass ratio, $\delta = (m_1 - m_2)/M > 0$ is a fractional mass difference and D_L is the luminosity distance to the source. The relative velocity v is related to the frequency, f, by $v = (\pi f M)^{1/3}$. In Ref. [37], Ψ is the orbital phase in the instantaneous orbital plane given as the phase, Φ, shifted in the presence of an arbitrary reference frequency $\omega_0 \neq \omega_{orb}$. Here we consider $\omega_0 \equiv \omega_{orb}$ and consequently $\Psi = \Phi$. Subsequently, we enter a co-precessing frame by setting the inclina-

tion $\iota = 0$ and the azimuthal angle $\alpha = 0$. We then substitute the single-spin approximation $\chi_{ax} = \chi_{sx} = \chi\cos(\alpha)/2$ and $\chi_{ay} = \chi_{sy} = \chi\sin(\alpha)/2$, which re-introduces α. In this co-precessing frame, the symmetric and the anti-symmetric waveform contributions are computed from their definitions given in Eqs. 4.4 and 4.5, respectively, and by keeping terms up to $O(v^4)$ order we obtain the relations

$$h^{CP,s}_{2,2} = A(2 + v^2(55\nu - 107))e^{-2i\Phi}, \tag{4.8}$$

$$h^{CP,a}_{2,2} = Av^2(1 + \delta)\chi e^{-i(\Phi+a)}, \tag{4.9}$$

where the amplitude $A = \sqrt{\pi/5}(3M\nu v^2/2D_L)$ and Φ is the total orbital phase.

From Eqs. 4.8 and 4.9, we can obtain some valuable insights. We notice that at this order the spin, χ, appears only in the amplitude of the anti-symmetric contribution. The anti-symmetric contribution enters at the order $O(v^4)$ while the symmetric contribution enters earlier at the order $O(v^2)$. The azimuthal angle α that determines the direction of the in-plane spin, is absent from the amplitude of the asymmetry but appears to modify the phase of the anti-symmetric part. As a result, we find that the phase of the asymmetry depends on the direction of the in-plane spin relative to the separation vector of the two black holes. Thus, the anti-symmetric phase exhibits variations that stem not only from the orbital phase, Φ, but also from the slower precession rotation of the spin, given by the azimuthal angle, α. This observation aligns with other observations from studies on out-of-plane recoil velocity that have provided evidence for a sinusoidal dependency between the amplitude of the recoil and the initial direction of the in-plane spin [63].

It is evident from Eq. 4.9 that adding a correction α_0 to the initial direction of the in-plane spin will result in a phase shift in the $(\ell = 2, m = 2)$ anti-symmetric waveform contribution. This is an important insight that substantially facilitated the construction of our multipole asymmetry model. It implies that by utilizing a set of single-spin NR waveforms that cover the parameter space of mass ratio, dimensionless spin magnitude and spin misalignment, it is possible to calibrate the multipole asymmetry model without extending the parameter space to include several initial in-plane spin directions. Due to this factor, we are able to use our BAM catalogue for the modelling. This catalogue contains 80 single-spin NR waveforms that were generated using the BAM code with mass ratios $q \in [1, 2, 4, 8]$, spin mag-

nitudes $\chi \in [0.2, 0.4, 0.6, 0.8]$ and spin angles $\theta_{LS} \in [30^o, 60^o, 90^o, 120^o, 150^o]$. More information about the construction of the BAM catalogue can be found in Section 2.8.2 and Ref. [5]. This catalogue has been previously used to construct `PhenomPNR` the first IMR model that calibrated precession effects to NR simulations [4].

An example of the amplitude and phase derivative of the anti-symmetric and symmetric components of a NR waveform in the frequency domain are presented in Fig. 4.2a and 4.2b. This single-spin NR waveform is from a binary with mass ratio $q = 1$, spin amplitude $\chi = 0.4$ and spin and orbital angular momentum misalignemnt $\theta_{LS} = 60^o$; full details are given in Ref. [5]. Following the procedure developed when producing the `IMRPhenomD` model [140, 141], and continued in subsequent models in the `Phenom` family [142, 143, 4], we consider the phase derivative, $\partial\phi/\partial f \equiv \phi'(f)$. Differentiating the phase removes an overall phase constant and enables a more precise examination of its features.

As we can see from Fig. 4.2a, both the symmetric and anti-symmetric amplitudes peak at the merger and then decrease with the same decay rate at the ringdown. In Fig. 4.2b, the anti-symmetric and symmetric phase derivatives exhibit a similar behaviour as they decrease sharply and perfectly match each other closer to the merger where they exhibit a "dip" at the ring-down frequency.

In the next sections, we show that a model of the ratio of the anti-symmetric amplitude over the symmetric amplitude can be used to scale the symmetric amplitude of any current frequency domain waveform or model. Similarly, we find that the multipole asymmetry phase can be computed using the symmetric contribution of the same waveform or model.

4.2.2 NR data conditioning for modelling

The model is tuned to 80 single-spin NR waveforms that were generated using the BAM code. In order to use the NR simulations to calibrate the asymmetry model in the frequency domain co-precessing frame, the NR waveforms need to be transformed from the BAM frame where they have been generated to the co-precessing frame. However, the NR data need to be first prepared by applying a smooth window function and zero padding. A Hann window is used to remove the inspiral "junk" radiation and numerical noise in the post-ringdown waveform that exists outside of the function's interval. Furthermore, to ensure that the frequency domain step size is sufficiently small, the time-

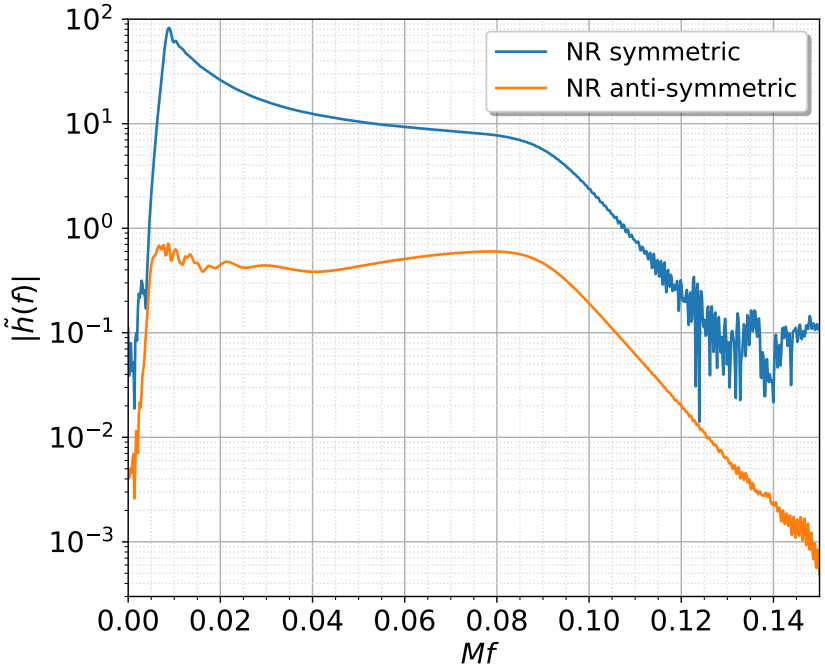

(a) The amplitude of the $(\ell = 2, m = 2)$ symmetric and anti-symmetric waveform components.

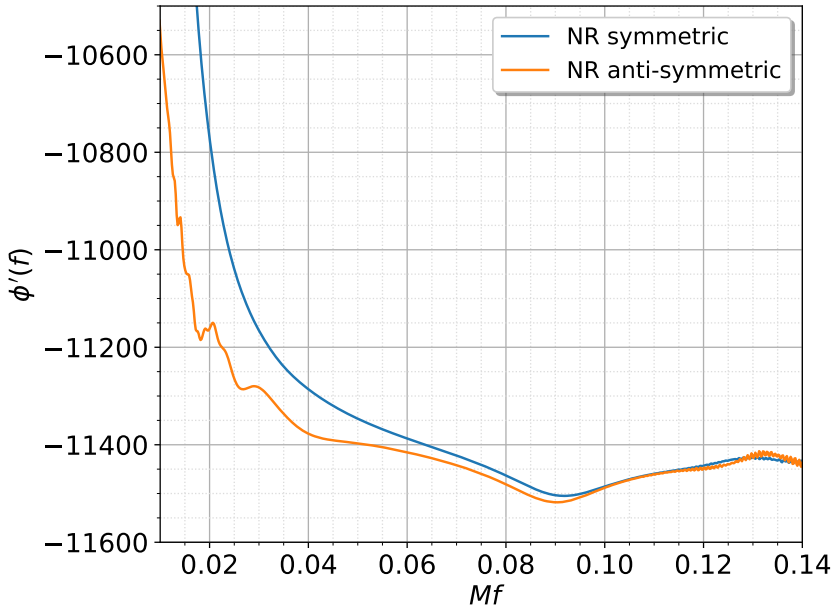

(b) The phase derivative of the $(\ell = 2, m = 2)$ symmetric and anti-symmetric waveform components.

Figure 4.2: The two panels show the amplitude and the phase derivative of the $(\ell = 2, m = 2)$ symmetric and anti-symmetric waveform components in the frequency-domain QA frame. The symmetric and anti-symmetric waveforms are computed for the $(q = 1, \chi = 0.4, \theta_{LS} = 60^o)$ NR simulation.

domain data are padded with zeros to the right. These processes ensure that the power of the signal is not exaggerated by noise and that the signal's features will be adequately resolved in the frequency-domain.

Then, to ensure that our NR data will pass smoothly to the chosen co-precessing frame, we follow the process presented in [4] and we first transform them to the $\hat{J}(t)$-frame. This is required because the total angular momentum of the NR waveforms does not remain fixed over time, but is shifted by a few degrees. The $\hat{J}(t)$-frame is a non-inertial frame where the total angular momentum of the binary, $\hat{J}(t)$, is fixed along the z-axis at all times.

To transform a waveform to the $\hat{J}(t)$-frame we first compute the total angular momentum, $J(t)$, from the expressions of the angular momentum emission rate given in [58]. This is achieved by integrating numerically these equations and setting the integration constant $J(0) = J_{ADM}$ to agree with the total angular momentum of the system at the start of the simulation. We have chosen to not include a model for the variations in $\hat{J}(t)$ for consistency with the construction of the `PhenomPNR` model, which, as a first attempt to model precession through merger and ringdown, did not model the variations in the direction of $J(t)$. Knowing the total angular momentum, $J(t)$, we compute the Euler angles, (α, β, γ) that perform a time-dependent rotation to the $\hat{J}(t)$-frame. The first two Euler angles are spherical angles and due to the minimum rotation condition [144], γ is given by

$$\dot{\gamma} = -\dot{\alpha}\cos\beta. \tag{4.10}$$

The waveform is then transformed to the chosen co-precessing frame, the quadrupole-aligned (QA) frame that tracks the direction of the maximum radiation emission. This is achieved by computing another set of Euler angles, (α, β, γ) that rotate the coordinate system form the $\hat{J}(t)$-frame to the co-precessing frame. In this frame, the multipoles are significantly simplified, with the $(l = 2, |m| = 2)$ multipoles having the strongest amplitude, and the presence of precession-induced modulations in the waveform is minimised.

Furthermore, the NR waveforms are transformed from the time-domain to the frequency-domain where the features of the signal can be more easily identified and we model the multipole asymmetry. To achieve this, we utilise the fast Fourier transform as defined in Eq. 4.11. Similarly, the data can be transformed back to the time-domain using the inverse fast Fourier transform. The transformation of the strain from the time-domain, $h(t)$, to the frequency-

domain, $\tilde{h}(f)$, and its inverse are given by

$$\tilde{h}(f) = \mathcal{FFT}\left(h(t)\right) = \int h(t)e^{-2\pi i f t}\, dt, \tag{4.11}$$

$$h(t) = \mathcal{IFFT}\left(\tilde{h}(f)\right) = \int \tilde{h}(f)e^{2\pi i f t}\, df. \tag{4.12}$$

In addition, to compute the strain, h, from ψ_4 in the frequency-domain we can use the following expression

$$\tilde{h}(f) = -\frac{\tilde{\psi}_4(f)}{\omega^2}. \tag{4.13}$$

where $\omega = 2\pi f$. Eq. 4.13 can be derived in the frequency domain from the following expression

$$\tilde{\psi}_4(f) = \mathcal{FFT}\left(\psi_4(t)\right) = \mathcal{FFT}\left(\ddot{h}(t)\right) = -\omega^2\tilde{h}(f). \tag{4.14}$$

The anti-symmetric and symmetric components of the waveform in the QA frame are computed from 4.5 and 4.4, respectively. The computed symmetric and anti-symmetric strains, h_s^{NR} and h_a^{NR}, are complex quantities that can be written as

$$h_s^{NR}(f) = A_s^{NR}(f)e^{i\phi_s^{NR}(f)}, \tag{4.15}$$

$$h_a^{NR}(f) = A_a^{NR}(f)e^{i\phi_a^{NR}(f)} \tag{4.16}$$

and we can easily calculate their amplitude, A^{NR}, and phase, ϕ^{NR}, as their absolute value and argument, respectively.

4.2.3 Symmetric and anti-symmetric contributions in PN theory

To create an efficient and accurate amplitude model, we have capitalized on the similar features of the symmetric and the anti-symmetric amplitude that are illustrated in Fig. 4.2a. Through our search for an efficient modelling approach, we have discovered that a simple and elegant solution is to scale the symmetric contribution of the waveform to match the anti-symmetric amplitude. This can be accomplished by multiplying the symmetric amplitude with a ratio of the anti-symmetric amplitude over the symmetric amplitude. As a result,

rather than directly modelling the multipole asymmetry amplitude shown in Fig. 4.2a, we have developed a model for this ratio that can subsequently be used to precisely scale the symmetric waveform.

From the NR data, we have identified the prospect of creating a ratio model. However, generating a complete IMR model requires obtaining accurately the ratio of these amplitudes over the appropriate frequency range. While we can rely on the NR data to accurately compute the ratio at higher frequencies, for the early inspiral we would need to utilize the PN theory to obtain the ratio. Thus we could attempt to produce a model that incorporates both the PN ratio and an NR-tuned correction at higher frequencies.

However, we need first to verify the accuracy of the PN ratio in frequencies bellow the start of the NR waveforms. This will ensure that the length of our waveforms is sufficient for the development of an accurate IMR modelling. To accomplish this, we will calculate, from PN theory, an approximate ratio of the anti-symmetric amplitude over the symmetric amplitude and construct hybrid PN-NR waveforms to study the behaviour of the PN ratio across a wide range of frequencies.

The first step in constructing the ratio model is to compute the ratio in the framework of PN theory as a PN expansion in terms of v/c where v is the relative velocity of the two black holes and c is the speed of light, and we choose geometric units where $c = 1$. We consider a single-spin binary black hole system where the dominant precession effects are present. The total mass of the system $M = m_1 + m_2$, where m_1 and m_2 are the masses of the two black holes, can be removed as an overall scale factor, and for simplicity we choose $M = 1$. The dimensionless spin on the larger black hole is $\chi = S_1/m_1^2$ where S_1 is the angular momentum magnitude of the larger black hole.

To compute the PN ratio, we obtain from Ref. [37] the complex PN expression of the time-domain $\ell = m = 2$ multipole, h_{22}^{PN}, for spinning, precessing binaries with generic inclination angle ι moving on nearly circular orbits through 1.5PN given in Eq. B1 of Ref. [37]. The $(\ell = 2, m = -2)$ multipole, h_{2-2}^{PN}, is computed from the h_{22}^{PN} multipole using Eqs. 4.7 and 4.6. The strains of the $\ell = |m| = 2$ multipoles can then be transformed to a co-precessing frame that follows the instantaneous orbital plane. To achieve this, we set to zero the inclination angle of the orbital angular momentum relative to the total angular momentum, $\iota = 0$, and we use an approximate reduction to a

single-spin system [4] by setting

$$\chi_{s/a,x} = -\chi \sin(\theta_{LS} - \iota)\cos(\alpha)/2 \quad (4.17)$$
$$\chi_{s/a,y} = -\chi \sin(\theta_{LS} - \iota)\sin(\alpha)/2 \quad (4.18)$$
$$\chi_{s/a,z} = \chi \cos(\theta_{LS} - \iota)/2 \quad (4.19)$$

where $\chi_s = (\chi_1+\chi_2)/2$, $\chi_a = (\chi_1-\chi_2)/2$ are the symmetric and anti-symmetric spins defined in Ref. [37] and θ_{LS} is the inclination of the spin from the orbital angular momentum vector.

In this co-precessing frame, we substitute the simplified PN $\ell = |m| = 2$ multipoles in Eqs. 4.4 and 4.5 to obtain the complex PN expressions of the symmetric and the anti-symmetric components of the waveform that can be written in the following form

$$h_s^{PN}(f) = A_s^{PN}(f)e^{i\phi_s^{PN}(f)}, \quad (4.20)$$
$$h_a^{PN}(f) = A_a^{PN}(f)e^{i\phi_a^{PN}(f)} \quad (4.21)$$

where A^{PN} and ϕ^{PN} the amplitude and the phase of the two components. Since the computed PN symmetric and anti-symmetric components are complex quantities, the desired amplitudes are their absolute values, A_s^{PN} and A_a^{PN}. Setting the luminosity distance to be $D_L = 1$ and considering $\alpha, \Psi \in \mathbb{R}$, the PN symmetric and anti-symmetric amplitudes of the $\ell = |m| = 2$ multipoles are given by

$$A_s^{PN}(f) = -\frac{4}{21}\sqrt{\frac{\pi}{5}}v^2\nu\left(42 + 84\pi v^3 + v^2(-107 + 55\nu) - 28v^3(1 + \delta - \nu)\chi\cos\theta_{LS}\right), \quad (4.22)$$
$$A_a^{PN}(f) = -2\sqrt{\frac{\pi}{5}}v^4(1+\delta)\nu\chi\sin\theta_{LS}. \quad (4.23)$$

The PN ratio of the two amplitudes is then given by the following expression

$$\kappa^{PN}(f) = \frac{21v^2(1+\delta)\chi\sin\theta_{LS}}{2(42 + 84\pi v^3 + v^2(-107 + 55\nu) - 28v^3(1 + \delta - \nu)\chi\cos\theta_{LS})}. \quad (4.24)$$

where $\nu = m_1m_2/M^2$ is the symmetric mass ratio, $\delta = (m_1 - m_2)/M > 0$ is a fractional mass difference, χ is the dimensionless spin magnitude and θ_{LS} is the angle between the orbital momentum and spin vector. The expression of

the PN ratio of the anti-symmetric amplitude over the symmetric amplitude depends on the symmetric mass ratio, ν, the spin magnitude, χ, and the angle θ_{LS} of the system. Consequently, Eq. 4.24 can be used to compute the PN ratio of any configuration as a function of frequency since $v = (\pi f M)^{1/3}$.

Having derived an expression for the ratio of the two amplitudes, we need to check its accuracy. To accomplish this we construct a hybrid PN-NR waveform that is longer than the NR waveforms and extends down to lower frequencies. In the next section, we study the behaviour of the PN ratio at low frequencies where the BAM simulations are less accurate.

4.2.4 Hybrids and amplitude ratio

As we explained in 4.2.3, the NR simulations describe well the last orbits, merger and ringdown of the binary black hole coalescence, but they are not accurate at the early inspiral phase. In contrast, at these lower frequencies, the PN approximation is accurate and could be used to study the behaviour of the anti-symmetric and symmetric amplitude ratio at this frequency range. Therefore, to test the accuracy of the PN ratio given by Eq. 4.24 and create a precise IMR model, we need to construct long waveforms that remain accurate across the whole frequency range of the IMR. This can be achieved by *stitching* together the PN and NR waveforms to construct hybridised PN-NR waveforms. Through this process we create longer waveforms that allow us to understand the phenomenology of the amplitudes during the three stages of the binary black hole coalescence.

Hybrid waveforms are frequently employed in waveform modelling as they are longer, more accurate waveforms throughout the IMR. They were first used in Ref. [145] in the development of `Phenom` models and since then they became a vital component in the development of many models of the `Phenom` family [145, 146, 140, 141, 142]. However, the utility of the hybrid waveforms extends beyond their application in waveform modelling. Refs. [147, 148, 149] have demonstrated the usefulness of PN-NR hybrid waveforms in studying the accuracy of the PN approximation for GW observations. They have also been used as approximate signals to test the efficiency of data-analysis pipelines before the first gravitational wave detection in Refs. [150, 151].

We build hybrid waveforms for the symmetric and anti-symmetric contributions of the dominant $\ell = 2$ and $|m| = 2$ multipoles for a selected single-spin system. This is a binary black hole system with mass ratio $q = m_1/m_2 = 2$,

primary black hole spin magnitude $\chi = 0.7$ and spin misalignement with the orbital angular momentum by $\theta_{LS} = 90^o$. The NR waveform for this configuration was generated with the BAM code for a previous study described in Ref. [126]. The NR data are transformed to the QA-frame and we compute the symmetric and anti-symmetric contributions of the $\ell = |m| = 2$ multipoles from their definitions given by Eqs. 4.4 and 4.5. The NR waveform starts at a frequency of $M\Omega = 0.025$ and it is sufficiently long to be used for the construction of full IMR hybrids, as indicated from Refs. [147, 148].

Since the PN-NR hybridised waveform is constructed to facilitate checking the accuracy of the PN ratio, we want to generate PN inspiral waveforms that illustrate accurately the phenomenology of this ratio at lower frequencies. As a result, in this case, we make no use of the approximations used for the construction of the PN ratio that we describe in Section 4.2.3. The construction of the PN waveform is done by solving the full PN equations of motion. For the evolution of the equations of motion, we follow the work presented in Refs. [123, 152, 153, 42] and we adopt the Taylor-expanded form of the Hamiltonian equations of motion. We utilise the non-spinning 3PN Hamiltonian presented in Refs. [154, 155, 156, 157, 158, 159] and the radiation flux that is given up to 3.5PN order [160, 161, 162]. We also include the leading-order [44, 163, 164, 165, 166, 167] and next-to-leading order [168, 169, 170] spin-orbit and spin-spin coupling terms of the Hamiltonian, as well as the spin-induced radiation flux terms outlined in Refs. [171, 44, 167]. Furthermore, we add the flux contribution resulting from the energy flowing into the black holes, which manifests at the relative 2.5PN order [172].

To obtain the multipoles of the precessing PN waveform, we use the expressions for the $h^{PN}_{l,m}$ multipoles given in Appendix B of Ref. [37] for generic inclination angle ι and compute the $h^{PN}_{l,-m}$ multipoles from Eqs. 4.6 and 4.7. We obtain the full PN waveform and we transform it to the chosen co-precessing frame, the QA-frame that tracks the direction of dominant emission. To achieve this, we compute the ψ_4 in the time-domain using the relation $\psi_4 = \ddot{h}$ and we compute the QA Euler angles (α, β, γ). In the QA-frame, we compute the symmetric and anti-symmetric contributions of the $\ell = |m| = 2$ multipoles from Eqs. 4.5 and 4.4.

The hybrid waveforms are constructed by first aligning the PN and NR waveforms and then joining them together. This process is repeated for the symmetric and the anti-symmetric waveforms. We start by finding the times at

which the PN and NR waveforms reach a selected common frequency ω_0, $\omega_0 = \omega_{PN}(t_{PN}) = \omega_{NR}(t_{NR})$ and we align them with a time and phase shift. We blend together the amplitude and the phase of the PN and NR anti-symmetric and symmetric contributions using the following piecewise expressions for the amplitude and the phase, respectively,

$$\psi_4^{hyb} = \begin{cases} \psi_4^{PN}(t+t_{PN}) & t \leq t_1 \\ \psi_4^{PN}(t+t_{PN}) \times t_{rm}(t) + \psi_4^{NR}(t+t_{NR}) \times t_{rp}(t) & t_1 \leq t \leq t_2 \\ \psi_4^{NR}(t+t_{NR}) & t > t_2 \end{cases} \tag{4.25}$$

$$\phi^{hyb} = \begin{cases} \phi^{PN}(t+t_{PN}) - \phi^{PN}(t_{PN}) & t \leq t_1 \\ \bar{\phi}^{\rm PN}(t) \times t_{rm}(t) + \bar{\phi}^{\rm NR}(t) \times t_{rp}(t) & t_1 \leq t \leq t_2 \\ \phi^{NR}(t+t_{NR}) - \phi^{NR}(t_{NR}) & t > t_2 \end{cases} \tag{4.26}$$

where

$$\bar{\phi}^{\rm PN}(t) = \phi^{\rm PN}(t+t_{\rm PN}) - \phi^{\rm PN}(t_{\rm PN}) \tag{4.27}$$

$$\bar{\phi}^{\rm NR}(t) = \phi^{\rm NR}(t+t_{\rm NR}) - \phi^{\rm NR}(t_{\rm NR}) \tag{4.28}$$

and t_{rm} and t_{rp} are the following transition functions

$$t_{rm}(t) = \frac{t_2 - t}{t_2 - t_1}, \tag{4.29}$$

$$t_{rp}(t) = \frac{t - t_1}{t_2 - t_1}, \tag{4.30}$$

that are applied to a time window with a width of $t_2 - t_1 = 500M$ for the symmetric and the anti-symmetric waveforms. From Eqs. 4.25 - 4.30, we separately obtain the PN-NR hybrid waveforms of the symmetric and anti-symmetric contributions in the time-domain.

To obtain from Eq. 4.25 the anti-symmetric and symmetric strain of the hybrid waveform in the frequency-domain where we want to model the asymmetry, the hybrid Ψ_4^{hyb} is transformed from the time-domain to the frequency-domain, $\tilde{\Psi}_4^{hyb}$, using the fast Fourier transform given by Eq. 4.11 and we employ Eq. 4.14 to compute the anti-symmetric and symmetric strain, $\tilde{h}_a^{hyb}$ and $\tilde{h}_s^{hyb}$,

in the frequency-domain. The two strains can be written in the following form

$$\tilde{h}_s^{hyb}(f) = A_s^{hyb}(f)e^{i\phi_s^{hyb}(f)}, \quad (4.31)$$
$$\tilde{h}_a^{hyb}(f) = A_a^{hyb}(f)e^{i\phi_a^{hyb}(f)} \quad (4.32)$$

where A^{hyb} and ϕ^{hyb} the amplitude and phase of the symmetric and anti-symmetric components, respectively. The amplitude and the phase derivative of the anti-symmetric component of the hybrid waveform are presented along with the corresponding NR data that we used to construct them in Fig. 4.10.

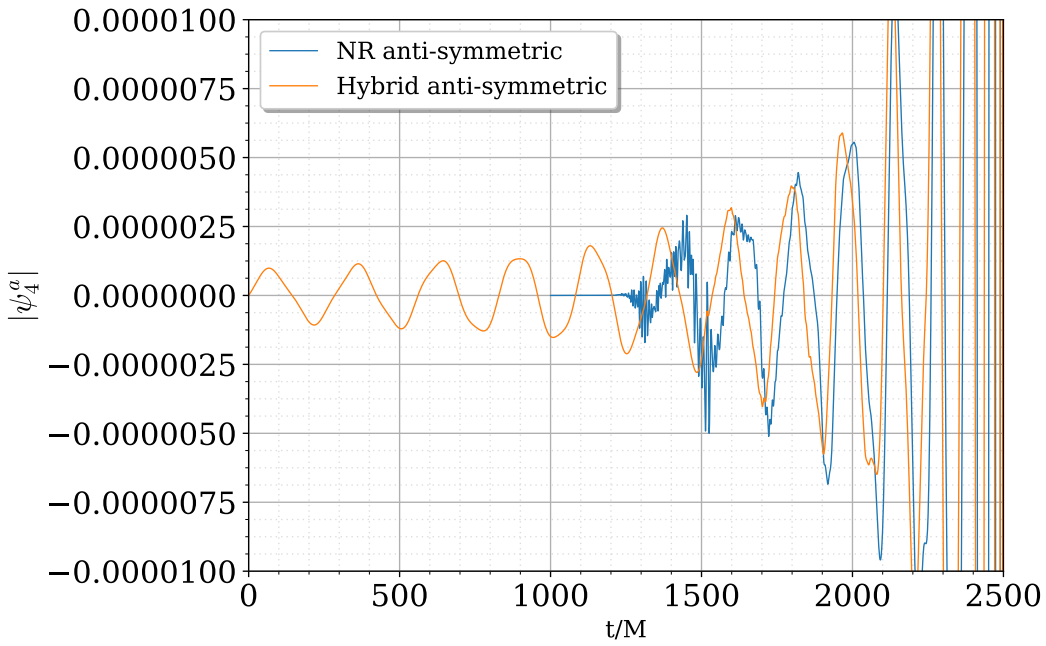

Figure 4.3: The anti-symmetric contribution of the hybrid waveform (orange) plotted against the anti-symmetric contribution of the NR waveform of the $(q = 2, \chi = 0.7, \theta_{LS} = 90^o)$ configuration in the time-domain. The waveforms have been aligned at the merger and at early times the asymmetry of the hybrid is oscillating.

The hybrid waveforms can be a valuable tool for comprehending the phenomenology of the ratio of the anti-symmetric to symmetric amplitude in the frequency-domain defined as

$$\kappa^{hyb}(f) = \frac{A_a^{hyb}(f)}{A_s^{hyb}(f)}. \quad (4.33)$$

The *hybrid ratio*, κ^{hyb}, allows us to test the accuracy of the PN ratio, κ^{PN}, given by Eq. 4.24. As we have discussed at the start of this section, at lower

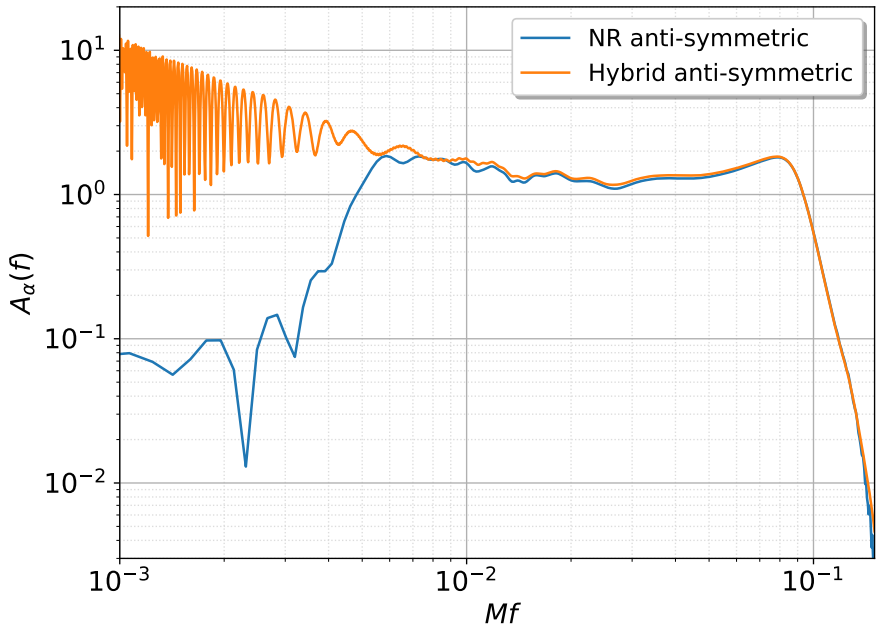

(a) The amplitude of the $(\ell = 2, m = 2)$ anti-symmetric component.

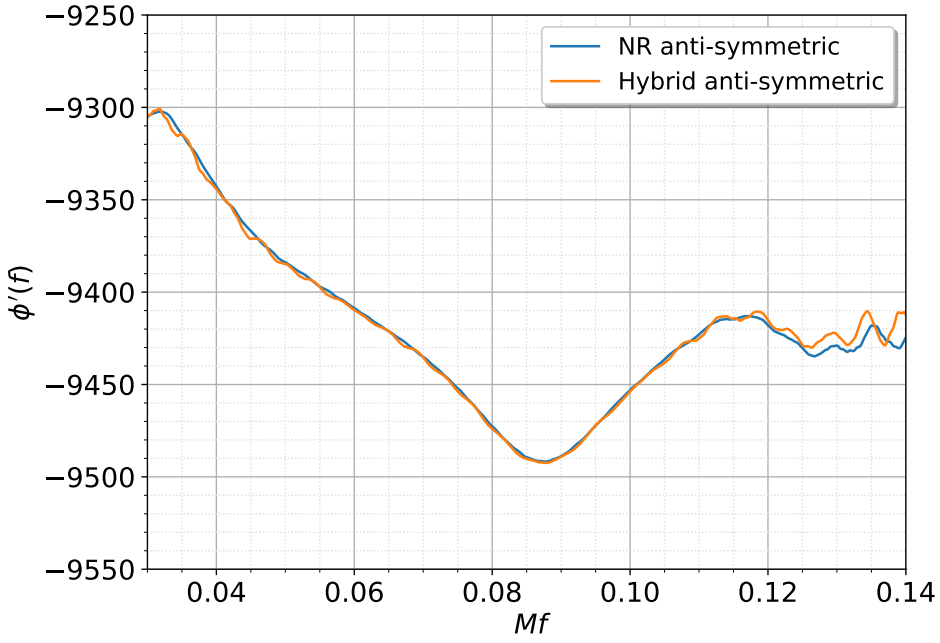

(b) The phase derivative of the $(\ell = 2, m = 2)$ anti-symmetric components.

Figure 4.4: The two panels show the amplitude and the phase derivative of the $(\ell = 2, m = 2)$ multipole asymmetry in the frequency-domain QA frame. The PN-NR hybridised waveform of the $(q = 2, \chi = 0.7, \theta_{LS} = 90^o)$ configuration is compare against the corresponding NR simulation.

frequencies we expect the PN-NR hybrid ratio to agree with the PN ratio that is also calculated from PN theory using some additional approximations. Due to these introduced approximations, it is also important to test the accuracy of the PN ratio in the NR regime.

The PN ratio, κ^{PN}, is compared against the hybrid and NR ratio, κ^{hyb} and κ^{NR}, respectively, of the same single-spin binary black hole system ($q = 2$, $\chi = 0.7$, $\theta_{LS} = 90^o$) in Fig. 4.5. We observe a region at the inspiral where all three ratios briefly agree indicating that the PN ratio is sufficiently accurate at those frequencies. At higher frequencies, the hybrid and NR ratios increase while the PN ratio reaches a plateau.

Due to the presence of the PN waveforms, the PN-NR hybrid ratio is longer and more accurate at the early inspiral compared to the NR ratio. In contrast to the PN ratio, in the early inspiral of the hybrid ratio, we notice the presence of large oscillations. These oscillations are absent from the PN ratio due to the fact that the $\ell = |m| = 2$ PN multipoles are transformed to a co-precessing frame by employing the approximation $\iota = 0$. On the other hand, in the case of the hybrid waveforms, the PN multipoles are transformed to a different co-precessing frame, the QA frame, using the QA angles (α, β, γ) [42, 4]. These observed oscillations will not be incorporated into the ratio model. Furthermore, as we can see from Fig. 4.5, the PN ratio goes through these modulations in the lower frequencies and captures accurately the behaviour of the hybrid ratio at the early inspiral.

These results suggest that our PN ratio is a good starting point for the construction of the amplitude model. Furthermore, since the PN ratio appears to be accurate up to the point where the PN waveforms begin, the use of the NR data is sufficient for the modelling and there is no need to construct hybrids for all the simulations. The PN ratio is accurate at the early inspiral, but needs to be improved to capture accurately the behaviour of the NR ratio at higher frequencies. To accomplish this and model accurately the NR ratio, we can add the appropriate higher order terms to Eq. 4.24 and the latter takes the form

$$\kappa(f) = \kappa(f)^{PN}(1 + bv^n), \tag{4.34}$$

where bv^n is the added higher order term. This will act as a correction to the lower order terms of the PN ratio, increasing its accuracy.

In our search for the appropriate correction we considered numerous combinations of higher order terms. To ensure that we will produce an efficient

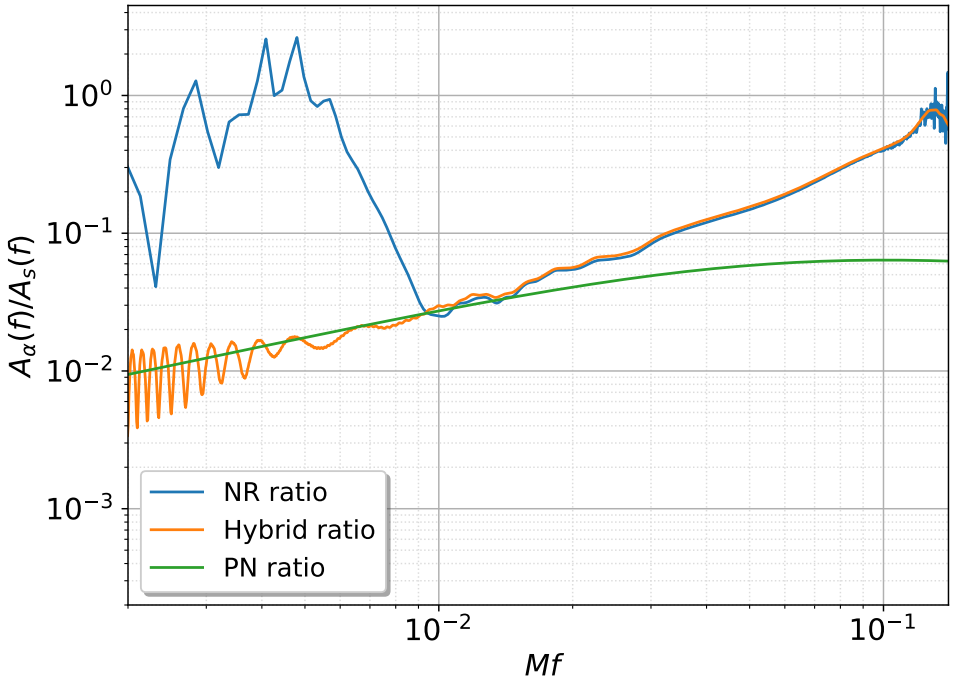

Figure 4.5: The ratios of the $(\ell = 2, m = 2)$ anti-symmetric over the symmetric amplitude of the $(q = 2, \chi = 0.7, \theta_{LS} = 90^o)$ signal. The PN ratio, $\kappa^{PN}(f)$, calculated in a co-precessing frame is compared against the hybrid ratio, $\kappa^{hyb}(f)$, and NR ratio, $\kappa^{NR}(f)$, computed in the frequency-domain QA frame.

model, we tried to choose the optimal candidate with the least number of free parameters. In Fig. 4.6, we present some of the higher order terms that we tested in order to find the most sufficient correction. From this investigation, we found that $n = 5$ was the optimal choice and that the addition of just one free parameter, b, captures well the behaviour of the NR ratio at the higher frequencies. Applying the selected correction to Eq. 4.34, the corrected PN ratio, $\kappa(f)$, can be written as

$$\kappa(f) = \kappa(f)^{PN}(1 + bv^5) \tag{4.35}$$

where bv^5 is the added NR calibrated correction. From Eq. 4.35, the ansatz of the ratio model takes the following form

$$\kappa(f) = \frac{21(v^2 + bv^7)(1 + \delta)\chi sin\theta}{2(42 + 84\pi v^3 + v^2(-107 + 55\nu) - 28v^3(1 + \delta - \nu)\chi cos\theta)}. \tag{4.36}$$

Similar to the PN ratio, κ^{PN}, the ratio model, κ, depends on the symmetric mass ratio, ν, the spin magnitude, χ, and the angle θ_{LS} of the system. As a result, given these three parameters of any configuration, from Eq. 4.35, we can compute the anti-symmetric to symmetric amplitude ratio, κ, as a function of frequency.

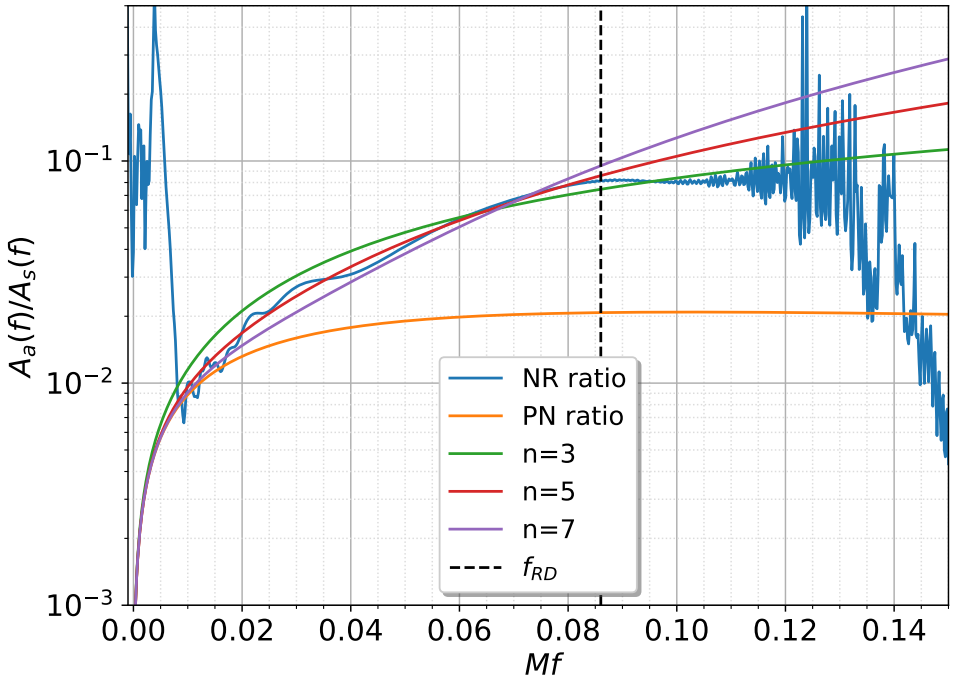

Figure 4.6: The NR ratio, $\kappa^{NR}(f)$, of the $(\ell = 2, m = 2)$ anti-symmetric over the symmetric amplitude of the $(q = 1, \chi = 0.4, \theta_{LS} = 60^o)$ NR waveform against the PN ratio, $\kappa^{PN}(f)$, and some of the tested ratio models. The considered ansatzes of the ratio model are computed by applying a *correction* to the PN ratio, $\kappa^{PN}(f)$, to increase its accuracy at higher frequencies. The ratio model, $\kappa(f)$, performs better compared to the other considered corrections.

To choose the appropriate frequency range for the modelling of the ratio, we considered numerous possible choices. Due to the inaccuracy of the NR data at the early inspiral and the presence of noise at the post-ringdown frequencies, we want to choose a frequency range where we can accurately model the NR ratio. Based on the NR data, we came to the conclusion that employing a fixed frequency range for all 80 NR simulations is not a viable option. To solve this, we have chosen a modelling frequency range that depends on the ringdown frequency, f_{RD} of the simulation. We considered different combinations and

we found that the frequency range $[f_{min} = (f_{RD} - 0.01)/5, f_{max} = f_{RD} - 0.002]$ ensures the highest level of accuracy of the modelling data.

In Fig. 4.7a, we show the results of the ratio model given by Eq. 4.36 along with the NR and PN ratio, κ^{NR} and κ^{PN}, for the selected configuration ($q = 1$, $\chi = 0.4$, $\theta_{LS} = 60^o$). The ratio model agrees well with the NR data up to the ringdown frequency f_{RD}. In the post-ringdown regime, the ratio model continues to increase while the NR ratio reaches a plateau.

However, from the perturbation theory, we expect the symmetric and anti-symmetric waveform amplitudes to have the same decay rate during the ringdown. In Ref. [173], it is explicated that the decay rate of the $(\ell = 2, m = 2)$ and $(\ell = 2, m = -2)$ multipoles is the same during the ringdown and is determined by the imaginary part of the complex ringdown frequency. As a result, the ratio of the anti-symmetric to symmetric amplitude should reach a plateau at frequencies $f \gtrsim f_{RD}$. Therefore, a final adjustment is made in order to set the ratio of the anti-symmetric and symmetric amplitudes, $\kappa(f)$, to the fixed value $\kappa(f \geq f_{RD}) = \kappa(f_{RD})$ that it reaches at the ringdown frequency. Furthermore, in order to avoid a sharp transition, we use a moving average algorithm such that

$$\kappa_n(f) = \frac{1}{(2k+1)} \sum_{i=n-k+1}^{n+k+1} \kappa(f_i), \quad n \in [k, N-k]. \tag{4.37}$$

We use a symmetric window of an equal number of points ($k = 40$) on either side of the frequency f to calculate the moving average. Here N is the length of the frequency series and the algorithm updates $\kappa(f)$ for $40 \leq n \leq N - 40$.

In Fig. 4.7a, we show the final ratio model, as given by Eq. 4.36, after implementing these corrections for the selected configuration ($q = 1$, $\chi = 0.4$, $\theta_{LS} = 60^o$). The final ratio model agrees well with the NR ratio during the entire IMR of the binary coalescence. Furthermore, during the ringdown, the ratio model reaches a plateau, as anticipated.

4.3 Amplitude model

The anti-symmetric amplitude, $A_a(f)$, can be constructed by rescaling the symmetric amplitude with the ratio $\kappa(f)$. The final amplitude model for the

anti-symmetric component can be written as

$$A_a(f) = \kappa(f) A_s(f) \tag{4.38}$$

where $\kappa(f)$ is the ratio model following as given by Eq. 4.36 decay rate correction and $A_s(f)$ is the amplitude of the symmetric component. The amplitude model estimates the anti-symmetric amplitude from the symmetric amplitude and it can in principle be used in any currently available frequency-domain waveform or model. As a result, we have created an efficient model that leverages the already available symmetric amplitude models.

The model is tuned to the 80 single-spin NR waveforms that consist the BAM catalogue. In Figs. 4.7a - 4.16, we present three different cases that show the performance of the amplitude model. In these examples, the symmetric amplitude that is rescaled as shown in Eq. 4.38, is computed from the NR data using Eqs. 4.4 and 4.15. The model exhibits a good agreement with the majority of the NR waveforms as it is shown in Figs. 4.7a and 4.13 where the ratio and the amplitude model of one of these cases are compared to the NR simulations.

However, for less than half of these simulations, the model is unable to fully reproduce all the features of the NR waveforms. In some cases, we noticed the presence of large oscillations in the IMR of the anti-symmetric amplitude of the NR waveforms that could not be captured by the model as is shown in Figs. 4.8a and 4.14. In these cases, the amplitude fit primarily goes through these oscillations.

In some other cases, the NR ratio of the amplitudes increases after the merger showing that the decay rate of the two amplitudes in the ringdown is not the same. An example is given in Figs. 4.10a - 4.16. However, due to the correction that was described in the previous section, the ratio model exhibits the expected behaviour. Therefore, the modelled anti-symmetric amplitude has the same decay rate as the symmetric amplitude as shown in Fig. 4.16.

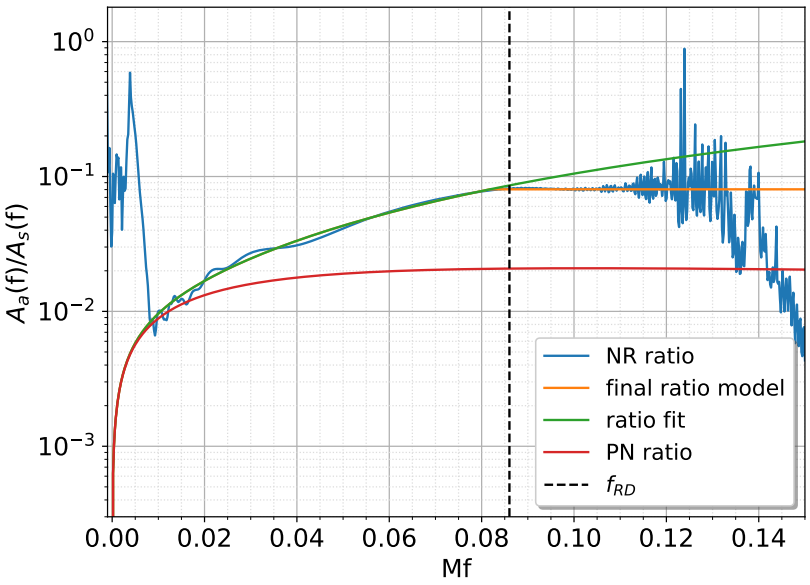

(a) The ratio model before (green) and following (orange) the decay rate correction against the NR ratio, $\kappa^{NR}(f)$, and the PN ratio, $\kappa^{PN}(f)$.

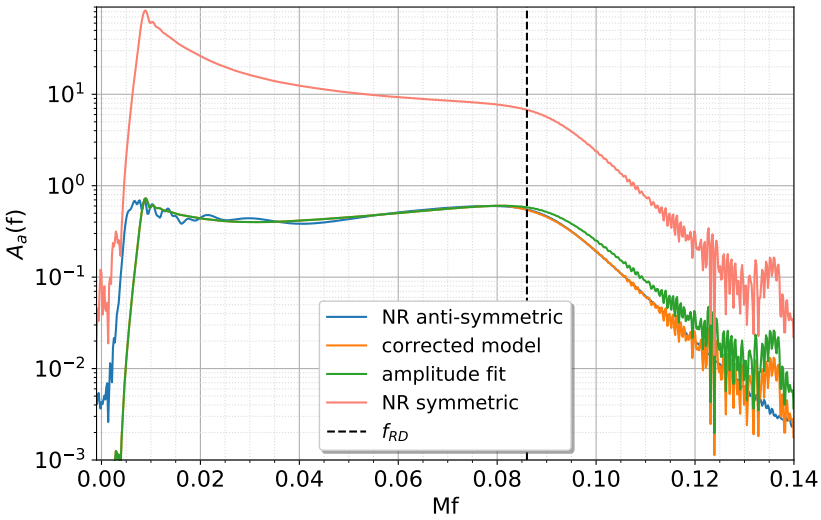

(b) The amplitude model before (green) and following (orange) the decay rate correction against the NR symmetric and anti-symmetric components of the waveform.

Figure 4.7: The two panels show the ratio and the multipole asymmetry amplitude model in the frequency-domain QA frame for the $(q = 1, \chi = 0.4, \theta_{LS} = 60^o)$ waveform. The initial fit performs well in this case up to the ringdown frequency f_{RD}. A correction has been applied to the final model (orange) to ensure its accuracy at frequencies $f \geq f_{RD}$.

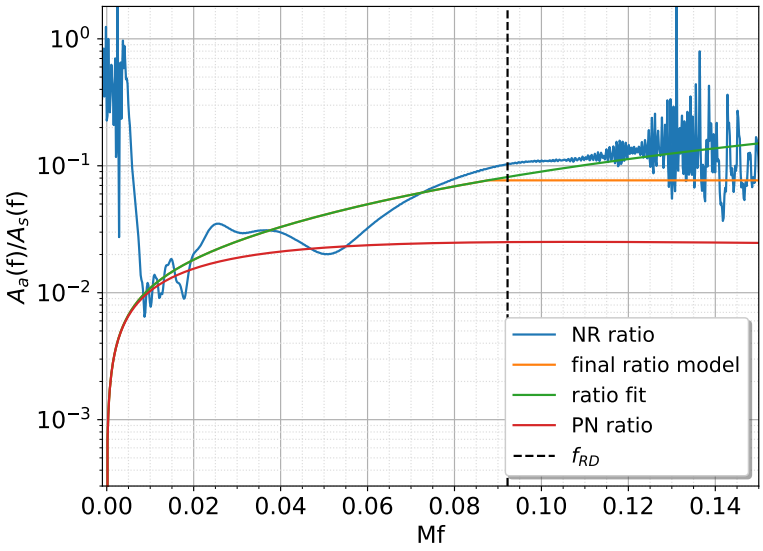

(a) The ratio model before (green) and following (orange) the decay rate correction against the NR ratio, $\kappa^{NR}(f)$, and the PN ratio, $\kappa^{PN}(f)$.

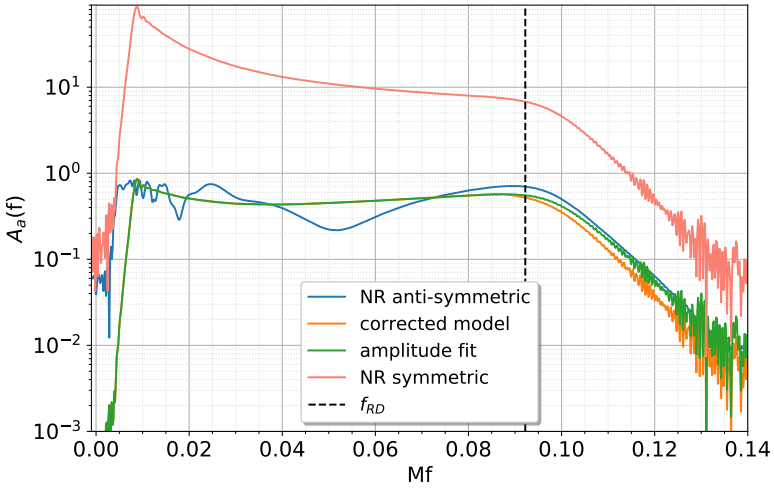

(b) The amplitude model before (green) and following (orange) the decay rate correction against the NR symmetric and anti-symmetric components of the waveform.

Figure 4.8: The two panels show the performance of the ratio and the multipole asymmetry amplitude model in the presence of large oscillations in the anti-symmetric amplitude for the $(q = 1, \chi = 0.8, \theta_{LS} = 30^o)$ waveform. The ratio and the amplitude model go through these oscillations. The ratio of the NR data is increasing at frequencies $f \geq f_{RD}$ instead of reaching a plateau. This is corrected in the final ratio model (orange) to ensure the model's accuracy.

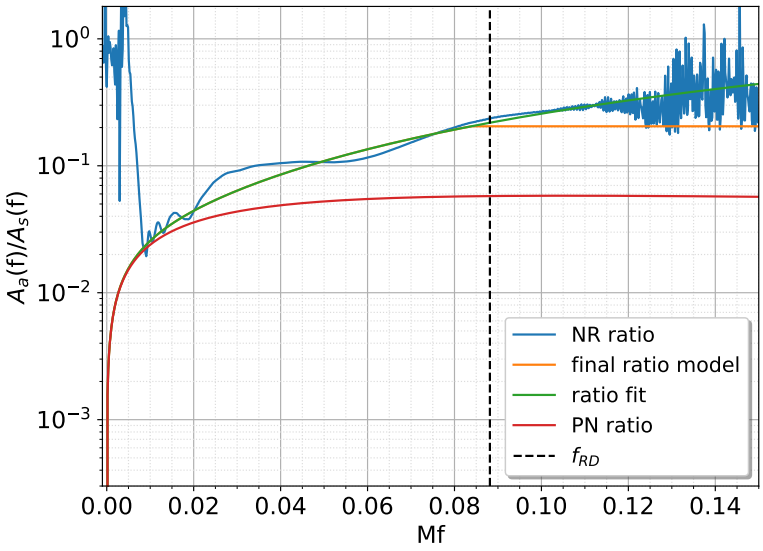

(a) The ratio model before (green) and following (orange) the decay rate correction against the NR ratio, $\kappa^{NR}(f)$, and the PN ratio, $\kappa^{PN}(f)$.

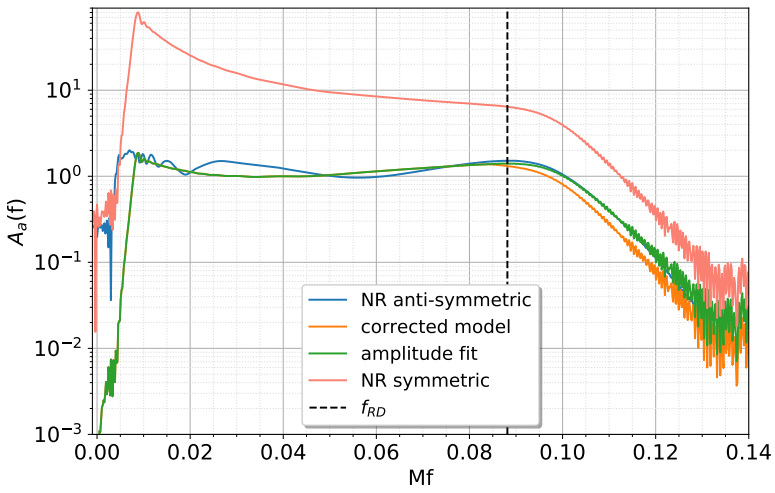

(b) The amplitude model before (green) and following (orange) the decay rate correction against the NR symmetric and anti-symmetric components of the waveform.

Figure 4.9: The two panels show the performance of the ratio and the multipole asymmetry amplitude model in the presence of small oscillations in the anti-symmetric amplitude for the $(q = 2, \chi = 0.8, \theta_{LS} = 60^o)$ waveform. The ratio and the amplitude model go through these oscillations. The ratio of the NR data is increasing at frequencies $f \geq f_{RD}$ rather than reaching a plateau. This is corrected in the final ratio model (orange) to ensure the model's accuracy.

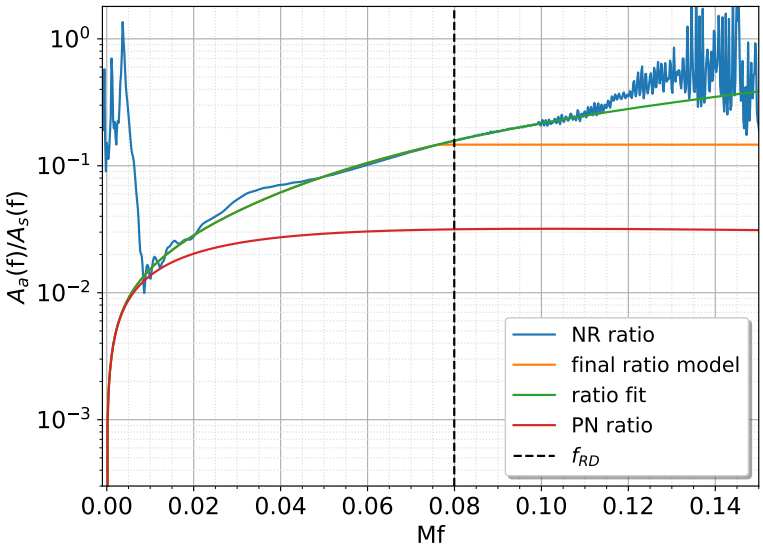

(a) The ratio model before (green) and following (orange) the decay rate correction against the NR ratio, $\kappa^{NR}(f)$, and the PN ratio, $\kappa^{PN}(f)$.

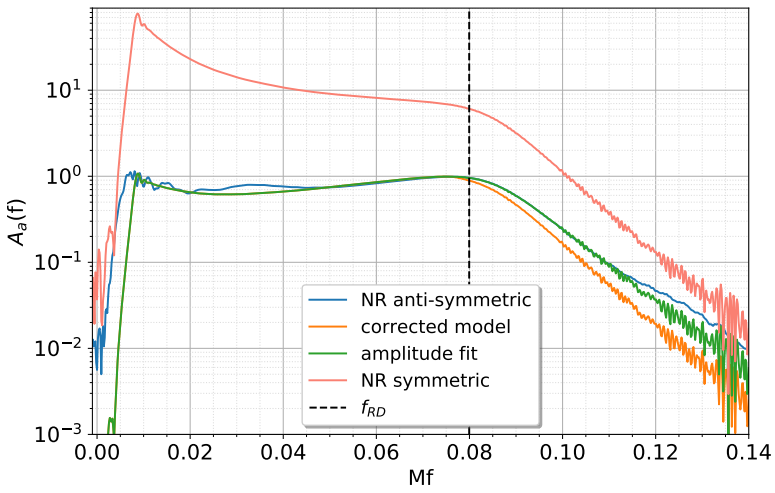

(b) The amplitude model before (green) and following (orange) the decay rate correction against the NR symmetric and anti-symmetric components of the waveform.

Figure 4.10: The two panels show the performance of the ratio and the multipole asymmetry amplitude model in a case where the amplitudes of the anti-symmetric and the symmetric NR ($q = 2, \chi = 0.4, \theta_{LS} = 90^o$) waveform have different decay rates. In this case, the amplitude's ratio is increasing at frequencies $f \geq f_{RD}$. This feature appears in some of the NR data and is corrected by applying a correction to the final model (orange).

4.4 Surface fit

As we have seen in the previous sections, the ratio model as given by Eq. 4.36, captures accurately the behaviour of the NR ratio at higher frequencies with only one free parameter, b. In Fig. 4.11, we show the values of the model's coefficient, b, as a function of the symmetric mass ratio, ν, for all the 80 NR simulations. From Fig. 4.11, the model's coefficient, b, is found to be independent of the spin, χ. Overall, there is no clear trend in the values of b with respect to spin, and we observe the present of some noise in the coefficients. Therefore, we can assume that the coefficient b remains independent of the spin χ and can be fitted across the two-dimensional ν, θ_{LS} parameter space by a surface of the form

$$b(\nu, \theta) = b_0 + b_1\nu + b_2\theta_{LS} + b_3\nu\theta_{LS} \tag{4.39}$$

where $b_0 = 18.0387$, $b_1 = 15.4509$, $b_2 = 55.1140$ and $b_3 = -203.6290$. From Eq. 4.39, we notice that b does not go to zero when θ_{LS} is 0^0 or 180^o. However, the presence of the $\sin\theta_{LS}$ term at the numerator of the ansatz of the ratio model in Eq. 4.36 ensures that the multipole asymmetry goes to zero for $\theta_{LS} = 0^o$ and $\theta_{LS} = 180^o$.

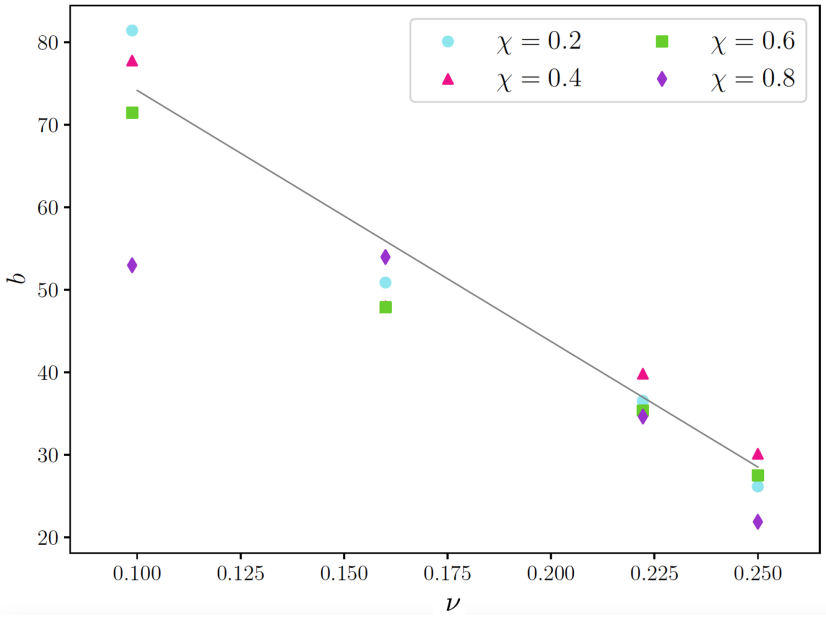

Figure 4.11: The b coefficient as a function of the symmetric mass ratio, ν, for a selected angle $\theta_{LS} = 90^o$ and all the available spin values, $\chi = [0.2, 0.4, 0.6, 0.8]$. The grey line shows the surface fit, $b(\nu, 90^\circ)$ from Eq. (4.39).

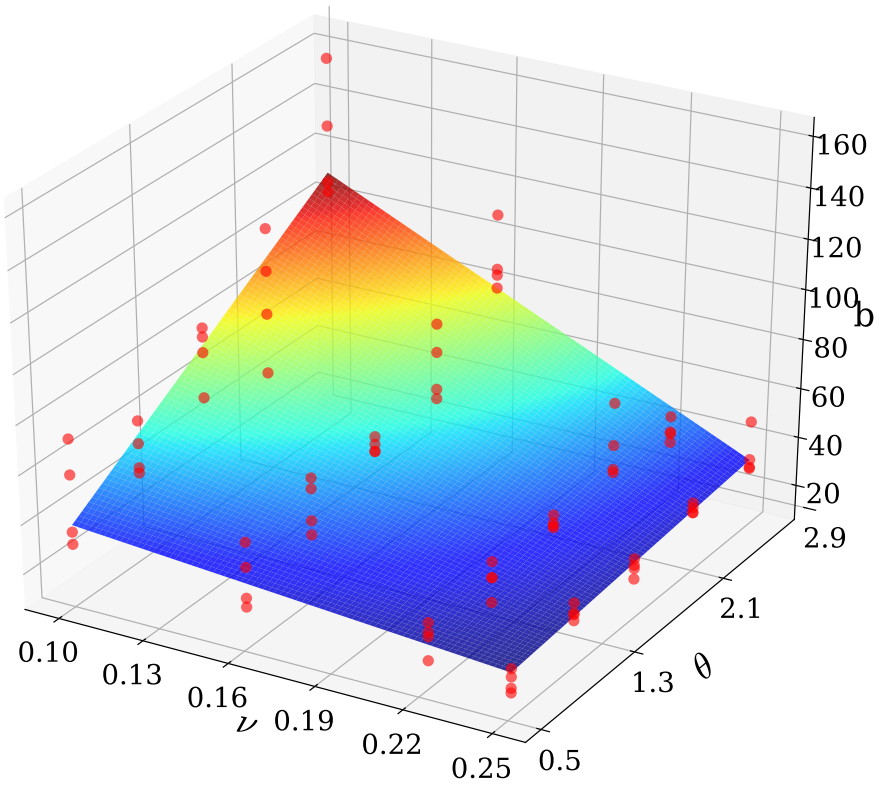

Figure 4.12: Surface $b(\nu, \theta_{LS}) = b_0 + b_1\nu + b_2\theta_{LS} + b_3\nu\theta_{LS}$ fit of the model's coefficient, b, to the two-dimensional parameter space ν, θ_{LS}. The red points denote the 80 computed b coefficients of the multipole asymmetry amplitude model.

The surface given by Eq. 4.39 fits sufficiently the coefficient's values that we have obtained from the modelling of the 80 NR configurations as it is shown in Fig. 4.12. Therefore, we can employ Eq. 4.39 to compute the values of the b coefficient and obtain the multipole asymmetry amplitude from Eq. 4.36. In Figs. 4.13 - 4.16, we show the anti-symmetric amplitude that we obtain using Eq. 4.39. For all the presented cases, the amplitude model that we compute using the surface fit performs well and the outcomes are in excellent agreement with the previous amplitude model results.

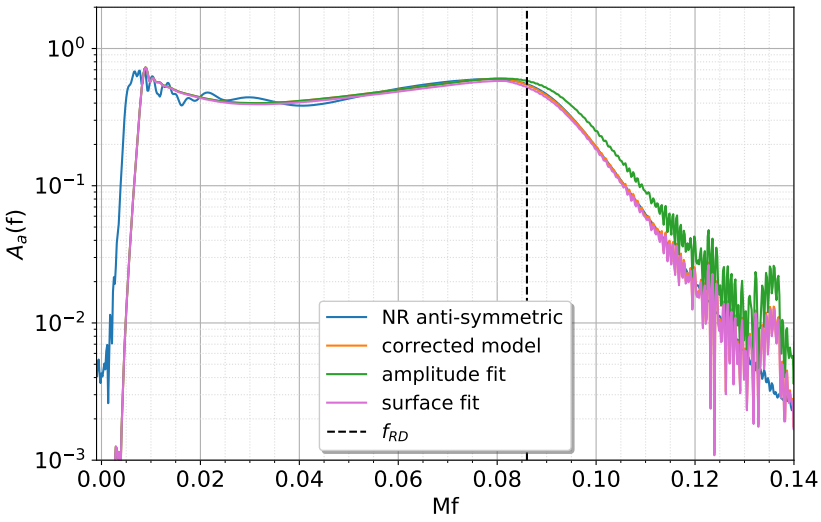

Figure 4.13: The anti-symmetric amplitude model computed from the surface fit given by Eq. 4.39 (purple) against the NR anti-symmetric amplitude (blue) and the amplitude model Eq. 4.38 before (green) and following (orange) the decay rate correction for the $(q = 1, \chi = 0.4, \theta_{LS} = 60^o)$ waveform. The amplitude model computed from the surface fit is in excellent agreement with the NR amplitude and the amplitude model following the decay rate correction.

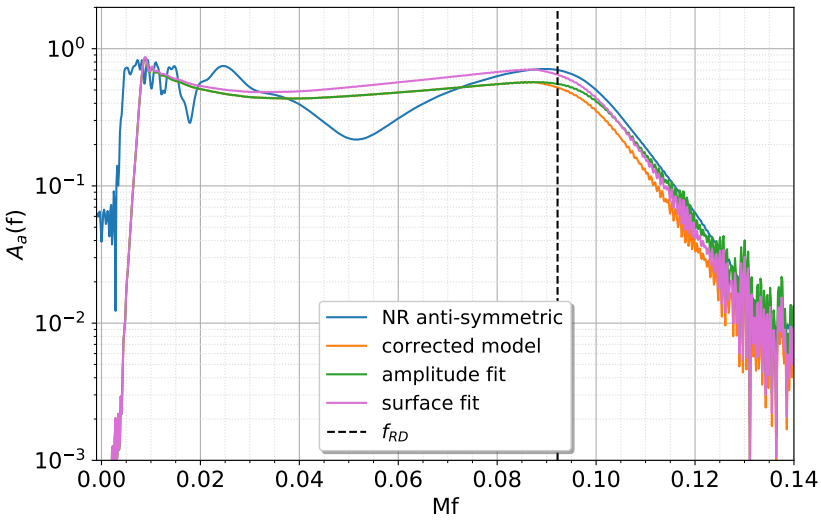

Figure 4.14: The performance of the final amplitude model in the presence of large oscillations for the $(q = 1, \chi = 0.8, \theta_{LS} = 30^o)$ waveform. A detailed description of the presented quantities is given in Fig. 4.13.

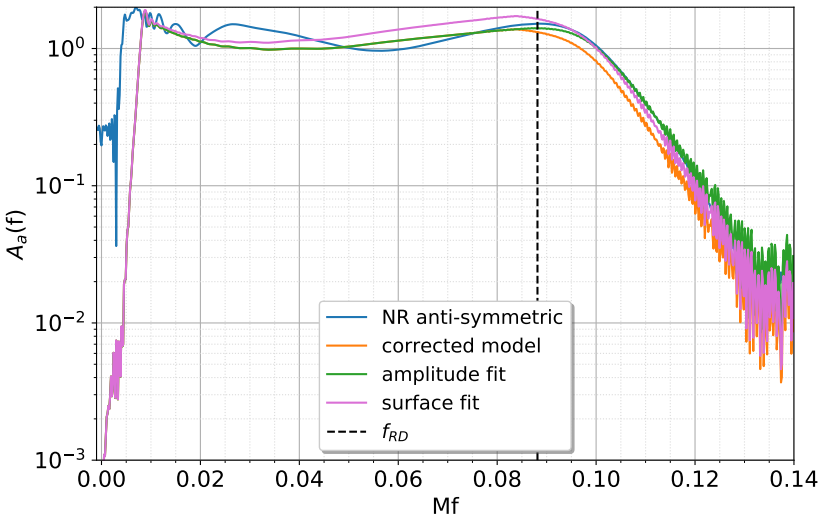

Figure 4.15: The performance of the final amplitude model in the presence of small oscillations for the $(q = 2, \chi = 0.8, \theta_{LS} = 60^o)$ waveform. A detailed description of the presented quantities is given in Fig. 4.13.

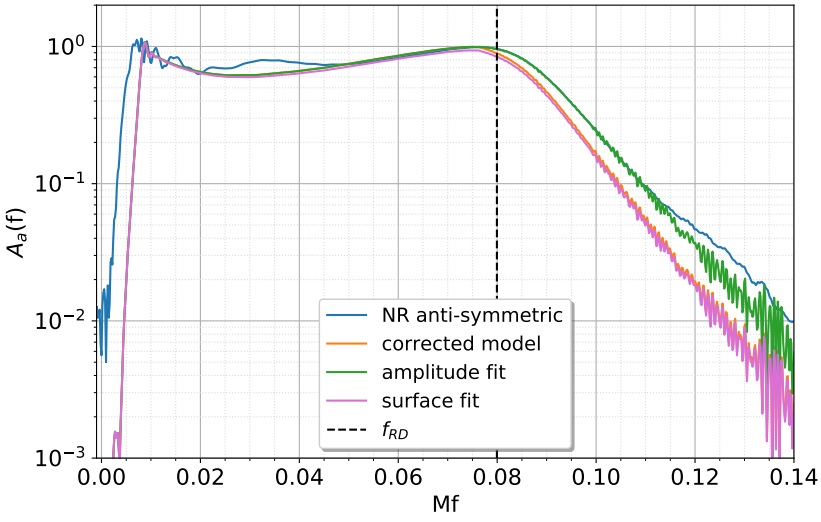

Figure 4.16: The performance of the final amplitude model for the $(q = 2, \chi = 0.4, \theta_{LS} = 90^o)$ waveform where the symmetric and anti-symmetric decay rates differ. A detailed description of the presented quantities is given in Fig. 4.13.

4.5 Phase model

For completion in this section we will give a brief overview of the phase model that was result of collaborative work (see *Collaborative work* at the start of the thesis). The anti-symmetric phase is equivalent to the orbital phase plus the precession angle during the inispiral, $\phi_s(f)/2 + \alpha(f)$, and in the ringdown it is equal to the symmetric phase. As we explained in Section 4.2.1, the model explicitly deals with the phase derivatives, and the phase derivative is defined by the piecewise function,

$$\phi'_a(f) = \begin{cases} \frac{1}{2}\phi'_s(f) + \alpha'(f) + A_0, & f \leq f_T \\ \phi'_s(f), & f_T \leq f < 0.15. \end{cases} \tag{4.40}$$

The phase derivative ansatz was calibrated to NR simulations by treating f_T as a free parameter. A choice of $f_T = 85\% f_{RD}$ was found to be appropriate across the parameter space. Applying a shift to the phase derivative is equivalent to an overall time shift of the waveform. We exploit this freedom by fixing the symmetric phase derivative minima to be 0 at f_{RD}. This imposes,

$$A_0 = \frac{1}{2}\phi'_s(f_T) - \alpha'(f_T). \tag{4.41}$$

The phase of the anti-symmetric waveform is obtained by integrating the two pieces,

$$\phi_a(f) = \begin{cases} \frac{1}{2}\phi_s(f) + \alpha(f) + A_0 * f + \phi_{A0}, & f \leq f_T \\ \phi_s(f) + \phi_{B0}, & f_T \leq f < 0.15, \end{cases} \tag{4.42}$$

where the integration constant ϕ_{B0} is determined by continuity at f_T

$$\phi_{B0} = \alpha(f_T) - \frac{\phi_s(f_T)}{2} + A_0 * f_T + \phi_{A0}. \tag{4.43}$$

The initial phase of the asymmetry is determined by the in-plane spin orientation, which also determines α. Therefore, the initial phase is set equal to the value of α at the reference frequency, $\phi_{A0} = \alpha(f_{\rm ref})$.

4.6 Model accuracy

A standard measure of waveform accuracy used extensively in the literature is the *match* of the waveform model with NR waveforms, defined as,

$$M(h_{NR}, h_M) = 4\,\mathrm{Re}\int_0^\infty \frac{\mathrm{h_{NR}(f)h_M^*(f)}}{\mathrm{S_n(f)}}\mathrm{df}, \tag{4.44}$$

where $h(f) = h_+(f) - ih_\times(f)$ is a complex frequency sequence constructed from the two polarizations of the waveform. As such, calculating matches of just the anti-symmetric waveform is not physically meaningful. Furthermore, a true measure of performance of precessing waveforms in data analysis can only be obtained by calculating matches of the full waveform in the inertial frame, making considerations for precession as well as extrinsic parameters. Therefore, matches of just the anti-symmetric waveform in the co-precessing frame provide some indication of the accuracy of one ingredient in the full waveform, but do not indicate the overall accuracy of the corresponding precessing waveform.

However, an inner product like that in Eq. 4.44 is a useful measure of agreement between two complex frequency series. Since a match-like calculation for the anti-symmetric contribution in the co-precessing frame cannot be interpreted in terms of either signal detection efficiency or parameter measurement accuracy, there is no reason to include the detector sensitivity, and so we will use a simpler inner product of the form,

$$\langle h_{NR}|h_M\rangle = \mathrm{Re}\int_{\mathrm{f_1}}^{\mathrm{f_2}} \mathrm{h_{NR}(f)h_M^*(f)df}, \tag{4.45}$$

where f_1 is the starting frequency of the NR waveform in geometric units, $Mf_1 = 0.02$, and $Mf_2 = 0.15$, after which point the amplitude of the NR waveform is below the noise floor of the data. We consider normalised waveforms, $\hat{h} = h/\sqrt{\langle h|h\rangle}$, so that the maximum value of the inner product is one. We used the standard implementation of this inner product in `pycbc` [174], a python software package for GW data analysis, for our match computations. We then consider the "mismatch" between the two waveforms,

$$\mathcal{M} = 1 - \frac{\langle h_{NR}|h_M\rangle}{\sqrt{\langle h_{NR}|h_{NR}\rangle\langle h_M|h_M\rangle}}. \tag{4.46}$$

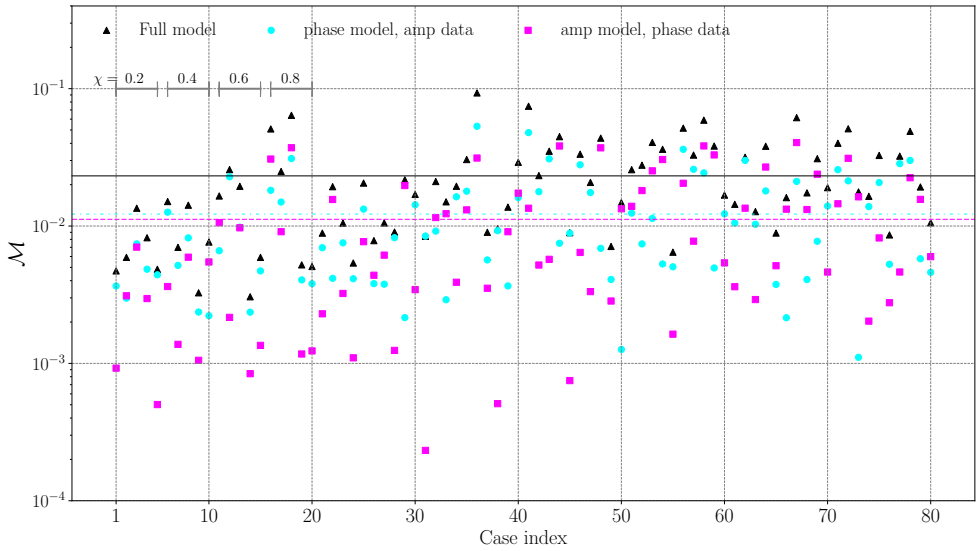

Figure 4.17: Mismatches of the anti-symmetric waveform model in the co-precessing frame with NR data. The black triangles show the mismatches for the combined amplitude and phase model while the magenta squares (cyan circles) show the mismatches for just the amplitude (phase) model with the phase (amplitude) constructed from NR data. The dashed magenta and cyan lines show the average mismatch for the amplitude and phase model, respectively; on average they are of comparable accuracy. The black solid line shows the average mismatch for the overall model. The x-axis denotes the case index of the NR simulation as usual i.e., five different $\theta_{\rm LS}$ for each spin magnitude shown in figure, for $q = 1$,2,4 and 8.

In Fig. 4.17 we show the mismatches of the anti-symmetric waveform constructed from our model with the 80 NR waveforms that were used to calibrate the model. To determine the accuracy of the individual components, we also computed matches of the amplitude (phase) model complemented by phase (amplitude) constructed from NR data, with the full anti-symmetric waveform constructed from NR data. The overall accuracy of both the models are comparable. We note that although the model was verified using the same waveforms as used for modelling, since the NR tuning was relatively simple — i.e., a single co-efficient in Eq. 4.35 fit to the four-parameter ansatz Eq. 4.39 across a two-dimensional parameter space — using a much smaller subset of waveforms would have produced a model of similar accuracy, and the simplicity of this model and the single-spin parameter space obviates any concerns about over-fitting or unexplored corners of parameter space.

To investigate the quality of the surface fit in Eq. 4.39, we also computed

mismatches for the amplitude model using fit coefficients b of Eq. 4.35. As is evident from Fig. 4.18, for most cases the performance is unchanged and for the handful of cases where the mismatch changes, the difference is not very significant. This further illustrates that capturing the non-linear dependence on spin magnitude is unlikely to make significant improvement to the amplitude model.

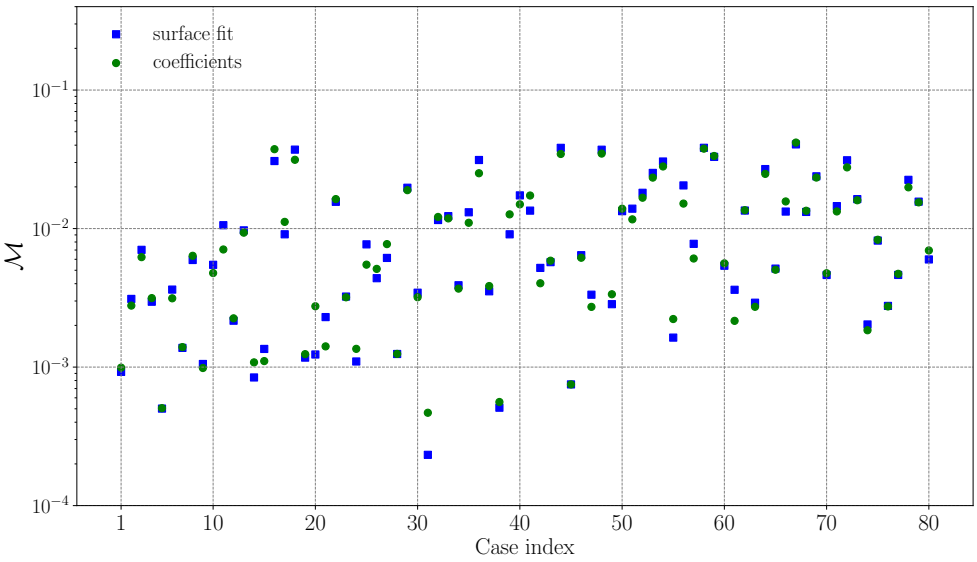

Figure 4.18: Mismatches (same as Fig. 4.17) showing comparison of the amplitude model constructed using the spin magnitude-independent surface fit of Eq. 4.35 (blue squares) with the amplitude model constructed from the true fit coefficients (green circles).

Note that the anti-symmetric waveform model is downstream from the symmetric waveform model as well as the precession angle models. Therefore, enhancement in performance of the overall model due to the addition of an asymmetry model must always be discussed in the context of the underlying symmetric, precessing waveform model. This is beyond the scope of present work and will be discussed in the context of the current generation frequency-domain precessing-binary `PhenomXPNR` model [137].

4.7 Conclusion

We have presented the first `Phenom` model for the ($\ell = 2, m = \pm 2$) multipoles asymmetry. We have developed a new efficient approach to model the

amplitude and phase of the multipole asymmetry employing any of the currently available symmetric models or waveform as the primary ingredient. We modelled the amplitude and the phase of the asymmetry separately in the frequency domain QA frame and we calibrated our mode using 80 NR single-spin simulations.

The amplitude is modelled by rescaling the symmetric contribution of the waveform using a ratio model. Rather than modelling directly the amplitude of the multipole asymmetry, we have developed a model of the ratio of the anti-synmetric over the symmetric amplitude that we then utilise to scale the symmetric waveform. To construct this model, we have calculated the PN expression of this ratio that is accurate at the early inspiral. Our ratio model is then created by adding a single higher order term as a correction to this expression creating a ratio model that is accurate throughout the IMR of the binary. This ratio model can be used to rescale any of the presently available symmetric models.

The development of the phase model was motivated by the behaviour of the asymmetry in the PN waveforms. The phase is constructing by combining the symmetric phase and the procession angle α. The phase is modelled during the inspiral by the sum of the symmetric phase and the precession angle α and is computed by the symmetric phase closer to the merger. Therefore, it can be modelled using only the symmetric phase and the procession angle α that are already modelled by the presently available waveform models.

The multipole asymmetry model has been implemented as part of higher-multipole extension to `PhenomPNR`, which is built on top of the `PhenomX` framework [4, 139, 142, 72]. This new `Phenom` waveform model that contains the multipole asymmetry is proposed for use in O4. It will be along with the NRSurogate the only models that contain the multipole asymmetry making possible the cross checking of the obtained results. Furthermore, we expect our model to produce robust results and measure the parameters of binaries that are outside the validity range of the surrogate.

Previous studies have shown the importance of including the multipole asymmetry in the waveform models to obtain accurate source measurements in the future observing runs. The modelling of the multipole asymmetry is particularly important for the future observing runs because the improved sensitivity of the detector will allow the detection of precessing systems. The presence of the multipole asymmetry will permit the accurate measurement of

the precession and the binaries spins.

This is a first model of the multipole asymmetry that can be further improved in the future to include two-spin effects, in-plane spin direction and higher modes. Furthermore, the current phase model is a first, effective approach that can be further improved in the future. Finally, it would be particularly interesting to perform a systematics study to quantify the model's accuracy across the parameter space.

Chapter 5

Conclusions and Future Directions

The rapidly increasing sensitivity of gravitational wave detectors expands our understanding of the universe and requires a parallel improvement of the waveform models. Accurate waveform models are essential for the measurement of the properties of the detected binaries. However, in some cases, the use of several approximations by these models can introduce systematic errors in the parameter estimation results.

In Chapter 3, our search of systematic errors introduced solely by the absence of multipole asymmetry in the waveform models demonstrated that its absence leads to significant biases in the estimation of the spins and tilt angles of precessing binary black hole systems with high SNR. In the same study, we also consider the highly precessing GW200129 signal [2, 3]. Our results showed that even at relatively low SNR, including the asymmetry in the model is essential in identifying this system as an unequal-mass binary with large in-plane spin. The presence of the multipole asymmetry in the waveform models is particularly important for the future detections as the sensitivity of the detectors is improved and signals will be recovered at higher SNR. Its absence could have a significant impact on population studies and the efforts to better understand the formation of the observed black holes that rely on the accurate measurement of the binary black hole parameters.

Based on these results, it becomes evident that the further improvement of the symmetric `Phenom` [64, 65, 66, 67, 68, 69, 70, 71, 72, 73, 74, 75, 4] and `EOBNR` [76, 77, 78, 79, 80, 81, 82] models will not be sufficient in order to accurately measure the parameters of the precessing detected systems without

including the multipole asymmetry in these models. Therefore, in Chapter 4, we proceed to model the asymmetry and present the first multipole asymmetry `Phenom` model where the amplitude and the phase of the asymmetry are modelled in the frequency-domain co-precessing frame. Our model is implemented into `PhenomPNR` [4] and it will become available during the $O4$ observing run.

Following the development of the asymmetry model and its implementation in `PhenomPNR`, the next step is to study the impact that our new model has on the accuracy of the parameter estimation results and test its performance with a series of parameter estimation runs. Furthermore, although our model should be increasing the accuracy of the `Phenom` models, it is a first approach in the modelling of the asymmetry and it can be further improved to ensure the accuracy of the models in the future runs.

A first step towards this direction is to include the sub-dominant modes of the asymmetry. As we have shown in Fig 4.1, the asymmetry of the sub-dominant modes is weak, however, in the future the modelling of the $(\ell = 3, |m| = 3)$ anti-symmetric component that is comparable to the $(\ell = 5, m = 5)$ multipole could increase the accuracy of the model. Furthermore, we are also producing a new series of simulations of two-spin systems that will be used to extend and improve the two-spin treatment of the `Phenom` models. Including the two-spin effects in our asymmetry model could also further improve its accuracy.

However, an important factor that we need to take into account in our efforts to further improve the asymmetry model is the way that the model is constructed. The model relies on the symmetric model used to compute the anti-symmetric amplitude and phase. As a result, we should also consider the accuracy and the limitations of the symmetric `Phenom` and `EOBNR` models.

Finally, we should also note that since the `Phenom` and `EOBNR` models are approximate models, as the detection of strongly precessing signals with even higher SNR will become possible, some of the used approximations might not hold. Therefore, it is also important to ensure the accuracy of the surrogate models in a wider area of the parameter space [83, 84, 85, 1, 86]. There are some promising approaches that could achieve this. Increasing the amount of the training data is computationally expensive, however, if this is possible, NR simulations developed in the areas of the parameter space where the accuracy of the models decreases could be used to build more accurate surrogate models. Another interesting approach to make the surrogate accurate for all the

possible binary masses is the hybridisation of the input waveforms with PN or EOB waveforms for the inspiral [1]. In addition, machine learning techniques such as deep neural networks have been used to create accurate and computationally fast surrogate models [175].

Bibliography

[1] Vijay Varma, *et al.* Surrogate models for precessing binary black hole simulations with unequal masses. *Phys. Rev. Research.*, 1:033015, 2019.

[2] Vijay Varma, *et al.* Evidence of Large Recoil Velocity from a Black Hole Merger Signal. *Phys. Rev. Lett.*, 128(19):191102, 2022.

[3] Mark Hannam *et al.* General-relativistic precession in a black-hole binary. *Nature*, 610(7933):652–655, 2022.

[4] Eleanor Hamilton, *et al.* Model of gravitational waves from precessing black-hole binaries through merger and ringdown. *Phys. Rev. D*, 104(12):124027, 2021.

[5] Eleanor Hamilton, *et al.* A catalogue of precessing black-hole-binary numerical-relativity simulations. *arXiv e-prints*, page arXiv:2303.05419, March 2023.

[6] Wikipedia, the free encyclopedia. Cumulative shift in the periastron period for psr b1913+16., 2004.

[7] Wikipedia, the free encyclopedia. Concept of ligo: A schematic diagram of a laser interferometer with light storage arms., 2012.

[8] B. P. Abbott, *et al.* Prospects for observing and localizing gravitational-wave transients with Advanced LIGO, Advanced Virgo and KAGRA. *Living Reviews in Relativity*, 23(1):3, September 2020.

[9] The LIGO Scientific Collaboration, *et al.* GWTC-3: Compact Binary Coalescences Observed by LIGO and Virgo During the Second Part of the Third Observing Run. *arXiv e-prints*, page arXiv:2111.03606, November 2021.

[10] B. P. Abbott, *et al.* Observation of Gravitational Waves from a Binary Black Hole Merger. *Physical Review Letters*, 116(6):061102, February 2016.

[11] B. P. Abbott, *et al.* GWTC-1: A Gravitational-Wave Transient Catalog of Compact Binary Mergers Observed by LIGO and Virgo during the First and Second Observing Runs. *Physical Review X*, 9(3):031040, July 2019.

[12] R. Abbott, *et al.* GWTC-2: Compact Binary Coalescences Observed by LIGO and Virgo during the First Half of the Third Observing Run. *Physical Review X*, 11(2):021053, April 2021.

[13] The LIGO Scientific Collaboration, *et al.* GWTC-2.1: Deep Extended Catalog of Compact Binary Coalescences Observed by LIGO and Virgo During the First Half of the Third Observing Run. *arXiv e-prints*, page arXiv:2108.01045, August 2021.

[14] A. Einstein. Näherungsweise Integration der Feldgleichungen der Gravitation. *Sitzungsberichte der Königlich Preußischen Akademie der Wissenschaften (Berlin), Seite 688-696.*, 1916.

[15] A. Einstein. Über Gravitationswellen. *Sitzungsberichte der Königlich Preußischen Akademie der Wissenschaften (Berlin), Seite 154-167.*, 1918.

[16] James B Hartle. Gravity: an introduction to einstein's general relativity, 2003.

[17] Bernard Schutz. *A first course in general relativity*. Cambridge university press, 2022.

[18] R. A. Hulse and J. H. Taylor. Discovery of a pulsar in a binary system. *The Astrophysical Journal*, 195:L51–L53, January 1975.

[19] Bradley W Carroll and Dale A Ostlie. *An introduction to modern astrophysics*. Cambridge University Press, 2017.

[20] J. M. Weisberg and J. H. Taylor. The Relativistic Binary Pulsar B1913+16: Thirty Years of Observations and Analysis. In F. A. Rasio and I. H. Stairs, editors, *Binary Radio Pulsars*, volume 328 of *Astronomical Society of the Pacific Conference Series*, page 25, July 2005.

[21] B. P. Abbott, *et al.* Observation of Gravitational Waves from a Binary Black Hole Merger. *Physical Review Letters*, 116(6):061102, February 2016.

[22] Kip S Thorne. Multipole expansions of gravitational radiation. *Reviews of Modern Physics*, 52(2):299, 1980.

[23] K Kokkotas. Gravitational waves. 2007.

[24] Curt Cutler and Kip S. Thorne. An Overview of Gravitational-Wave Sources. In Nigel T. Bishop and Sunil D. Maharaj, editors, *General Relativity and Gravitation*, pages 72–111, September 2002.

[25] B. S. Sathyaprakash and Bernard F. Schutz. Physics, Astrophysics and Cosmology with Gravitational Waves. *Living Reviews in Relativity*, 12(1):2, December 2009.

[26] K. Riles. Gravitational waves: Sources, detectors and searches. *Progress in Particle and Nuclear Physics*, 68:1–54, January 2013.

[27] Keith Riles. Searches for continuous-wave gravitational radiation. *Living Reviews in Relativity*, 26(1):3, December 2023.

[28] Junaid Aasi, *et al.* Advanced ligo. *Classical and quantum gravity*, 32(7):074001, 2015.

[29] Fet al Acernese, *et al.* Advanced virgo: a second-generation interferometric gravitational wave detector. *Classical and Quantum Gravity*, 32(2):024001, 2014.

[30] Yoichi Aso, *et al.* Interferometer design of the kagra gravitational wave detector. *Physical Review D*, 88(4):043007, 2013.

[31] Harald Lück, *et al.* The upgrade of geo 600. In *Journal of Physics: Conference Series*, volume 228, page 012012. IOP Publishing, 2010.

[32] Pau Amaro-Seoane, *et al.* Laser Interferometer Space Antenna. *arXiv e-prints*, page arXiv:1702.00786, February 2017.

[33] D. V. Martynov, *et al.* Sensitivity of the Advanced LIGO detectors at the beginning of gravitational wave astronomy. *Physical Review D*, 93(11):112004, June 2016.

[34] Peter R. Saulson. Gravitational wave detection: Principles and practice. *Comptes Rendus Physique*, 14(4):288–305, April 2013.

[35] B. P. Abbott, *et al.* A guide to LIGO-Virgo detector noise and extraction of transient gravitational-wave signals. *Classical and Quantum Gravity*, 37(5):055002, March 2020.

[36] Michele Maggiore. *Gravitational waves: Volume 1: Theory and experiments*. OUP Oxford, 2007.

[37] K. G. Arun, Alessandra Buonanno, Guillaume Faye, and Evan Ochsner. Higher-order spin effects in the amplitude and phase of gravitational waveforms emitted by inspiraling compact binaries: Ready-to-use gravitational waveforms. *Phys. Rev. D*, 79:104023, 2009. [Erratum: Phys.Rev.D 84, 049901 (2011)].

[38] Luc Blanchet. Gravitational radiation from post-newtonian sources and inspiralling compact binaries. *Living Reviews in Relativity*, 17(1):2, 2014.

[39] J. N. Goldberg, A. J. Macfarlane, E. T. Newman, F. Rohrlich, and E. C. G. Sudarshan. Spin-s Spherical Harmonics and d. *Journal of Mathematical Physics*, 8(11):2155–2161, November 1967.

[40] Bernd Brügmann, *et al.* Calibration of moving puncture simulations. *Physical Review D*, 77(2):024027, 2008.

[41] Ian Hinder, *et al.* Error-analysis and comparison to analytical models of numerical waveforms produced by the NRAR Collaboration. *Classical and Quantum Gravity*, 31(2):025012, January 2013.

[42] Patricia Schmidt, Mark Hannam, and Sascha Husa. Towards models of gravitational waveforms from generic binaries: A simple approximate mapping between precessing and nonprecessing inspiral signals. *Physical Review D*, 86(10):104063, November 2012.

[43] Theocharis A. Apostolatos, Curt Cutler, Gerald J. Sussman, and Kip S. Thorne. Spin-induced orbital precession and its modulation of the gravitational waveforms from merging binaries. *Physical Review D*, 49(12):6274–6297, June 1994.

[44] Lawrence E. Kidder. Coalescing binary systems of compact objects to (post)$^{5/2}$-Newtonian order. V. Spin effects. *Physical Review D*, 52(2):821–847, July 1995.

[45] Mark Hannam. Modelling gravitational waves from precessing black-hole binaries: progress, challenges and prospects. *General Relativity and Gravitation*, 46(9):1767, 2014.

[46] Duncan A. Brown, Andrew Lundgren, and R. O'Shaughnessy. Nonspinning searches for spinning black hole-neutron star binaries in ground-based detector data: Amplitude and mismatch predictions in the constant precession cone approximation. *Physical Review D*, 86(6):064020, September 2012.

[47] Patricia Schmidt, Mark Hannam, Sascha Husa, and P. Ajith. Tracking the precession of compact binaries from their gravitational-wave signal. *Physical Review D*, 84(2):024046, July 2011.

[48] R. O'Shaughnessy, J. Healy, L. London, Z. Meeks, and D. Shoemaker. Is J enough? Comparison of gravitational waves emitted along the total angular momentum direction with other preferred orientations. *Physical Review D*, 85(8):084003, April 2012.

[49] Patricia Schmidt, Frank Ohme, and Mark Hannam. Towards models of gravitational waveforms from generic binaries: II. Modelling precession effects with a single effective precession parameter. *Physical Review D*, 91(2):024043, January 2015.

[50] Theocharis A. Apostolatos, Curt Cutler, Gerald J. Sussman, and Kip S. Thorne. Spin-induced orbital precession and its modulation of the gravitational waveforms from merging binaries. *Physical Review D*, 49(12):6274–6297, June 1994.

[51] R. O'Shaughnessy, B. Vaishnav, J. Healy, Z. Meeks, and D. Shoemaker. Efficient asymptotic frame selection for binary black hole spacetimes using asymptotic radiation. *Physical Review D*, 84(12):124002, December 2011.

[52] Michael Boyle, Robert Owen, and Harald P. Pfeiffer. Geometric approach to the precession of compact binaries. *Physical Review D*, 84(12):124011, December 2011.

[53] Eleanor Hamilton and Mark Hannam. Inferring black-hole orbital dynamics from numerical-relativity gravitational waveforms. *Physical Review D*, 98(8):084018, October 2018.

[54] Manuela Campanelli, Carlos O. Lousto, Yosef Zlochower, and David Merritt. Maximum Gravitational Recoil. *Physical Review Letters*, 98(23):231102, June 2007.

[55] José A. González, Ulrich Sperhake, Bernd Brügmann, Mark Hannam, and Sascha Husa. Maximum Kick from Nonspinning Black-Hole Binary Inspiral. *Physical Review Letters*, 98(9):091101, March 2007.

[56] Frank Herrmann, Ian Hinder, Deirdre Shoemaker, Pablo Laguna, and Richard A. Matzner. Gravitational Recoil from Spinning Binary Black Hole Mergers. *The Astrophysical Journal*, 661(1):430–436, May 2007.

[57] Manuela Campanelli, Carlos Lousto, Yosef Zlochower, and David Merritt. Large Merger Recoils and Spin Flips from Generic Black Hole Binaries. *The Astrophysical Journal*, 659(1):L5–L8, April 2007.

[58] Milton Ruiz, Miguel Alcubierre, Darío Núñez, and Ryoji Takahashi. Multiple expansions for energy and momenta carried by gravitational waves. *General Relativity and Gravitation*, 40(8):1705–1729, August 2008.

[59] Michael Boylan-Kolchin, Chung-Pei Ma, and Eliot Quataert. Core Formation in Galactic Nuclei due to Recoiling Black Holes. *The Astrophysical Journal*, 613(1):L37–L40, September 2004.

[60] Piero Madau and Eliot Quataert. The Effect of Gravitational-Wave Recoil on the Demography of Massive Black Holes. *The Astrophysical Journal*, 606(1):L17–L20, May 2004.

[61] Noam I. Libeskind, Shaun Cole, Carlos S. Frenk, and John C. Helly. The effect of gravitational recoil on black holes forming in a hierarchical universe. *Monthly Notices of the Royal Astronomical Society*, 368(3):1381–1391, May 2006.

[62] José A. González, Mark Hannam, Ulrich Sperhake, Bernd Brügmann, and Sascha Husa. Supermassive Recoil Velocities for Binary Black-Hole Mergers with Antialigned Spins. *Physical Review Letters*, 98(23):231101, June 2007.

[63] Bernd Bruegmann, Jose A. Gonzalez, Mark Hannam, Sascha Husa, and Ulrich Sperhake. Exploring black hole superkicks. *Phys. Rev. D*, 77:124047, 2008.

[64] Mark Hannam, *et al.* Simple Model of Complete Precessing Black-Hole-Binary Gravitational Waveforms. *Physical Review Letters*, 113(15):151101, October 2014.

[65] Sascha Husa, *et al.* Frequency-domain gravitational waves from nonprecessing black-hole binaries. I. New numerical waveforms and anatomy of the signal. *Physical Review D*, 93(4):044006, February 2016.

[66] Sebastian Khan, *et al.* Frequency-domain gravitational waves from nonprecessing black-hole binaries. II. A phenomenological model for the advanced detector era. *Physical Review D*, 93(4):044007, February 2016.

[67] Lionel London, *et al.* First Higher-Multipole Model of Gravitational Waves from Spinning and Coalescing Black-Hole Binaries. *Physical Review Letters*, 120(16):161102, April 2018.

[68] Sebastian Khan, Katerina Chatziioannou, Mark Hannam, and Frank Ohme. Phenomenological model for the gravitational-wave signal from precessing binary black holes with two-spin effects. *Physical Review D*, 100(2):024059, July 2019.

[69] Jonathan E. Thompson, *et al.* Modeling the gravitational wave signature of neutron star black hole coalescences. *Physical Review D*, 101(12):124059, June 2020.

[70] Héctor Estellés, *et al.* Time domain phenomenological model of gravitational wave subdominant harmonics for quasi-circular non-precessing binary black hole coalescences. *arXiv e-prints*, page arXiv:2012.11923, December 2020.

[71] Sebastian Khan, Frank Ohme, Katerina Chatziioannou, and Mark Hannam. Including higher order multipoles in gravitational-wave models for precessing binary black holes. *Physical Review D*, 101(2):024056, January 2020.

[72] Cecilio García-Quirós, *et al.* Multimode frequency-domain model for the gravitational wave signal from nonprecessing black-hole binaries. *Physical Review D*, 102(6):064002, September 2020.

[73] Geraint Pratten, *et al.* Setting the cornerstone for a family of models for gravitational waves from compact binaries: The dominant harmonic for nonprecessing quasicircular black holes. *Physical Review D*, 102(6):064001, September 2020.

[74] Geraint Pratten, *et al.* Computationally efficient models for the dominant and subdominant harmonic modes of precessing binary black holes. *Physical Review D*, 103(10):104056, May 2021.

[75] Héctor Estellés, *et al.* Phenomenological time domain model for dominant quadrupole gravitational wave signal of coalescing binary black holes. *Physical Review D*, 103(12):124060, June 2021.

[76] Andrea Taracchini, *et al.* Prototype effective-one-body model for nonprecessing spinning inspiral-merger-ringdown waveforms. *Physical Review D*, 86(2):024011, July 2012.

[77] Yi Pan, *et al.* Inspiral-merger-ringdown waveforms of spinning, precessing black-hole binaries in the effective-one-body formalism. *Physical Review D*, 89(8):084006, April 2014.

[78] Andrea Taracchini, *et al.* Effective-one-body model for black-hole binaries with generic mass ratios and spins. *Physical Review D*, 89(6):061502, March 2014.

[79] Alejandro Bohé, *et al.* Improved effective-one-body model of spinning, nonprecessing binary black holes for the era of gravitational-wave astrophysics with advanced detectors. *Physical Review D*, 95(4):044028, February 2017.

[80] Roberto Cotesta, *et al.* Enriching the symphony of gravitational waves from binary black holes by tuning higher harmonics. *Physical Review D*, 98(8):084028, October 2018.

[81] Andrew Matas, *et al.* Aligned-spin neutron-star-black-hole waveform model based on the effective-one-body approach and numerical-relativity simulations. *Physical Review D*, 102(4):043023, August 2020.

[82] Serguei Ossokine, *et al.* Multipolar effective-one-body waveforms for precessing binary black holes: Construction and validation. *Physical Review D*, 102(4):044055, August 2020.

[83] Jonathan Blackman, *et al.* A Surrogate model of gravitational waveforms from numerical relativity simulations of precessing binary black hole mergers. *Physical Review D*, 95(10):104023, May 2017.

[84] Jonathan Blackman, *et al.* Numerical relativity waveform surrogate model for generically precessing binary black hole mergers. *Physical Review D*, 96(2):024058, July 2017.

[85] Vijay Varma, Davide Gerosa, Leo C. Stein, François Hébert, and Hao Zhang. High-Accuracy Mass, Spin, and Recoil Predictions of Generic Black-Hole Merger Remnants. *Physical Review Letters*, 122(1):011101, January 2019.

[86] Vijay Varma, *et al.* Surrogate model of hybridized numerical relativity binary black hole waveforms. *Physical Review D*, 99(6):064045, March 2019.

[87] Thibault Damour. Introductory Lectures on the Effective One Body Formalism. *International Journal of Modern Physics A*, 23(8):1130–1148, January 2008.

[88] Thibault Damour. The General Relativistic Two Body Problem and the Effective One Body Formalism. In Jiří Bičák and Tomáš Ledvinka, editors, *General Relativity, Cosmology and Astrophysics*, volume 177, page 111. 2014.

[89] Frans Pretorius. Simulation of binary black hole spacetimes with a harmonic evolution scheme. *Classical and Quantum Gravity*, 23(16):S529–S552, August 2006.

[90] M. Campanelli, C. O. Lousto, P. Marronetti, and Y. Zlochower. Accurate Evolutions of Orbiting Black-Hole Binaries without Excision. *Physical Review Letters*, 96(11):111101, March 2006.

[91] John G. Baker, Joan Centrella, Dae-Il Choi, Michael Koppitz, and James van Meter. Gravitational-Wave Extraction from an Inspiraling Configu-

ration of Merging Black Holes. *Physical Review Letters*, 96(11):111102, March 2006.

[92] Sebastian Khan, Frank Ohme, Katerina Chatziioannou, and Mark Hannam. Including higher order multipoles in gravitational-wave models for precessing binary black holes. *Physical Review D*, 101(2):024056, January 2020.

[93] Serguei Ossokine *et al.* Multipolar Effective-One-Body Waveforms for Precessing Binary Black Holes: Construction and Validation. *Phys. Rev. D*, 102(4):044055, 2020.

[94] P. Ajith *et al.* Inspiral-merger-ringdown waveforms for black-hole binaries with non-precessing spins. *Phys. Rev. Lett.*, 106:241101, 2011.

[95] B. P. Abbott, *et al.* Effects of waveform model systematics on the interpretation of GW150914. *Classical and Quantum Gravity*, 34(10):104002, May 2017.

[96] S. Khan, K. Chatziioannou, M. Hannam, and F. Ohme. Phenomenological model for the gravitational-wave signal from precessing binary black holes with two-spin effects. *arXiv e-prints*, September 2018.

[97] Kipp Cannon, *et al.* Toward early-warning detection of gravitational waves from compact binary coalescence. *The Astrophysical Journal*, 748(2):136, 2012.

[98] John Veitch, *et al.* Parameter estimation for compact binaries with ground-based gravitational-wave observations using the lalinference software library. *Physical Review D*, 91(4):042003, 2015.

[99] Thomas Bayes. Lii. an essay towards solving a problem in the doctrine of chances. by the late rev. mr. bayes, frs communicated by mr. price, in a letter to john canton, amfr s. *Philosophical transactions of the Royal Society of London*, (53):370–418, 1763.

[100] Lee S. Finn. Detection, measurement, and gravitational radiation. *Physical Review D*, 46(12):5236–5249, December 1992.

[101] Curt Cutler and Éanna E. Flanagan. Gravitational waves from merging compact binaries: How accurately can one extract the binary's parameters from the inspiral waveform\? *Physical Review D*, 49(6):2658–2697, March 1994.

[102] Emily Baird, Stephen Fairhurst, Mark Hannam, and Patricia Murphy. Degeneracy between mass and spin in black-hole-binary waveforms. *Physical Review D*, 87(2):024035, January 2013.

[103] George EP Box and George C Tiao. *Bayesian inference in statistical analysis*. John Wiley & Sons, 2011.

[104] John Skilling. Nested sampling for general bayesian computation. 2006.

[105] J. Veitch and A. Vecchio. Bayesian coherent analysis of in-spiral gravitational wave signals with a detector network. *Physical Review D*, 81(6):062003, March 2010.

[106] Gregory Ashton, *et al.* BILBY: A User-friendly Bayesian Inference Library for Gravitational-wave Astronomy. *The Astrophysical Journal Supplement Series*, 241(2):27, April 2019.

[107] Nelson Christensen and Renate Meyer. Using markov chain monte carlo methods for estimating parameters with gravitational radiation data. *Physical Review D*, 64(2):022001, 2001.

[108] Duncan A. Brown. *Searching for Gravitational Radiation from Binary Black Hole MACHOs in the Galactic Halo*. PhD thesis, -, May 2007.

[109] Nicholas Metropolis, Arianna W. Rosenbluth, Marshall N. Rosenbluth, Augusta H. Teller, and Edward Teller. Equation of State Calculations by Fast Computing Machines. *The Journal of Chemical Physics*, 21(6):1087–1092, June 1953.

[110] Thomas W Baumgarte and Stuart L Shapiro. *Numerical relativity: solving Einstein's equations on the computer*. Cambridge University Press, 2010.

[111] Bernd Brügmann, Wolfgang Tichy, and Nina Jansen. Numerical simulation of orbiting black holes. *Physical review letters*, 92(21):211101, 2004.

[112] Sascha Husa, José A. González, Mark Hannam, Bernd Brügmann, and Ulrich Sperhake. Reducing phase error in long numerical binary black hole evolutions with sixth-order finite differencing. *Classical and Quantum Gravity*, 25(10):105006, May 2008.

[113] Lawrence E Kidder, Mark A Scheel, Saul A Teukolsky, Eric D Carlson, and Gregory B Cook. Black hole evolution by spectral methods. *Physical Review D*, 62(8):084032, 2000.

[114] Dieter R. Brill and Richard W. Lindquist. Interaction Energy in Geometrostatics. *Physical Review*, 131(1):471–476, July 1963.

[115] Mark Hannam, Sascha Husa, Frank Ohme, Bernd Brügmann, and Niall O Murchadha. Wormholes and trumpets: Schwarzschild spacetime for the moving-puncture generation. *Physical Review D*, 78(6):064020, 2008.

[116] Steven Brandt and Bernd Brügmann. A Simple Construction of Initial Data for Multiple Black Holes. *Physical Review Letters*, 78(19):3606–3609, May 1997.

[117] Jeffrey M. Bowen and James W. York. Time-asymmetric initial data for black holes and black-hole collisions. *Phys. Rev. D*, 21:2047–2056, Apr 1980.

[118] Marcus Ansorg, Bernd Brügmann, and Wolfgang Tichy. Single-domain spectral method for black hole puncture data. *Physical Review D*, 70(6):064011, September 2004.

[119] Masaru Shibata and Takashi Nakamura. Evolution of three-dimensional gravitational waves: Harmonic slicing case. *Physical Review D*, 52(10):5428–5444, November 1995.

[120] Thomas W. Baumgarte and Stuart L. Shapiro. Numerical integration of einstein's field equations. *Phys. Rev. D*, 59:024007, Dec 1998.

[121] Marsha J. Berger and Joseph Oliger. Adaptive Mesh Refinement for Hyperbolic Partial Differential Equations. *Journal of Computational Physics*, 53(3):484–512, March 1984.

[122] Ezra Newman and Roger Penrose. An Approach to Gravitational Radiation by a Method of Spin Coefficients. *Journal of Mathematical Physics*, 3(3):566–578, May 1962.

[123] Sascha Husa, Mark Hannam, José A. González, Ulrich Sperhake, and Bernd Brügmann. Reducing eccentricity in black-hole binary evolutions with initial parameters from post-Newtonian inspiral. *Physical Review D*, 77(4):044037, February 2008.

[124] L. London. *nrutils*, 2015.

[125] B. P. Abbott, *et al.* GW151226: Observation of Gravitational Waves from a 22-Solar-Mass Binary Black Hole Coalescence. *Physical Review Letters*, 116(24):241103, June 2016.

[126] Chinmay Kalaghatgi and Mark Hannam. Investigating the effect of in-plane spin directions for precessing binary black hole systems. *Phys. Rev. D*, 103(2):024024, 2021.

[127] Antoni Ramos-Buades, Patricia Schmidt, Geraint Pratten, and Sascha Husa. Validity of common modeling approximations for precessing binary black holes with higher-order modes. *Phys. Rev. D*, 101(10):103014, 2020.

[128] LIGO Scientific Collaboration. *LIGO Algorithm Library.* doi.org/10.7935/GT1W-FZ16, 2018.

[129] Andrew Gelman and Donald B Rubin. Inference from iterative simulation using multiple sequences. *Statistical science*, 7(4):457–472, 1992.

[130] Patricia Schmidt, Ian W Harry, and Harald P Pfeiffer. Numerical relativity injection infrastructure. *arXiv preprint arXiv:1703.01076*, 2017.

[131] Milton Ruiz, Ryoji Takahashi, Miguel Alcubierre, and Dario Nunez. Multipole expansions for energy and momenta carried by gravitational waves. *Gen. Rel. Grav.*, 40:2467, 2008.

[132] R. Abbott *et al.* GWTC-3: Compact Binary Coalescences Observed by LIGO and Virgo During the Second Part of the Third Observing Run. 11 2021.

[133] Curt Cutler and Eanna E. Flanagan. Gravitational waves from merging compact binaries: How accurately can one extract the binary's parameters from the inspiral wave form? *Phys. Rev.*, D49:2658–2697, 1994.

[134] Eric Poisson and Clifford M. Will. Gravitational waves from inspiraling compact binaries: Parameter estimation using second postNewtonian wave forms. *Phys. Rev.*, D52:848–855, 1995.

[135] P. Ajith. Addressing the spin question in gravitational-wave searches: Waveform templates for inspiralling compact binaries with nonprecessing spins. *Phys. Rev. D*, 84:084037, 2011.

[136] Antoni Ramos-Buades, *et al.* Seobnrv5phm: Next generation of accurate and efficient multipolar precessing-spin effective-one-body waveforms for binary black holes. *arXiv preprint arXiv:2303.18046*, 2023.

[137] Jonathan E. Thompson, *et al.* Higher-multipole frequency-domain model of gravitational waves from precessing binaries with numerical-relativity calibrated precession. 2023. in preparation.

[138] Lionel London, *et al.* First Higher-Multipole Model of Gravitational Waves from Spinning and Coalescing Black-Hole Binaries. *Physical Review Letters*, 120(16):161102, April 2018.

[139] Geraint Pratten *et al.* Computationally efficient models for the dominant and subdominant harmonic modes of precessing binary black holes. *Phys. Rev. D*, 103(10):104056, 2021.

[140] Sascha Husa, *et al.* Frequency-domain gravitational waves from nonprecessing black-hole binaries. I. New numerical waveforms and anatomy of the signal. *Phys. Rev. D*, 93(4):044006, 2016.

[141] Sebastian Khan, *et al.* Frequency-domain gravitational waves from nonprecessing black-hole binaries. II. A phenomenological model for the advanced detector era. *Phys. Rev. D*, 93(4):044007, 2016.

[142] Geraint Pratten, *et al.* Setting the cornerstone for a family of models for gravitational waves from compact binaries: The dominant harmonic for nonprecessing quasicircular black holes. *Phys. Rev. D*, 102(6):064001, 2020.

[143] Cecilio García-Quirós, *et al.* Multimode frequency-domain model for the gravitational wave signal from nonprecessing black-hole binaries. *Phys. Rev. D*, 102(6):064002, 2020.

[144] Michael Boyle, Robert Owen, and Harald P. Pfeiffer. Geometric approach to the precession of compact binaries. *Physical Review D*, 84(12):124011, December 2011.

[145] P. Ajith *et al.* A Template bank for gravitational waveforms from coalescing binary black holes. I. Non-spinning binaries. *Phys. Rev. D*, 77:104017, 2008. [Erratum: Phys.Rev.D 79, 129901 (2009)].

[146] L. Santamaria *et al.* Matching post-Newtonian and numerical relativity waveforms: systematic errors and a new phenomenological model for non-precessing black hole binaries. *Phys. Rev. D*, 82:064016, 2010.

[147] Mark Hannam, Sascha Husa, Frank Ohme, and P. Ajith. Length requirements for numerical-relativity waveforms. *Phys. Rev. D*, 82:124052, 2010.

[148] Frank Ohme, Mark Hannam, and Sascha Husa. Reliability of complete gravitational waveform models for compact binary coalescences. *Phys. Rev. D*, 84:064029, 2011.

[149] Ilana MacDonald, Samaya Nissanke, and Harald P. Pfeiffer. Suitability of post-Newtonian/numerical-relativity hybrid waveforms for gravitational wave detectors. *Classical and Quantum Gravity*, 28(13):134002, July 2011.

[150] P. Ajith *et al.* The NINJA-2 catalog of hybrid post-Newtonian/numerical-relativity waveforms for non-precessing black-hole binaries. *Class. Quant. Grav.*, 29:124001, 2012. [Erratum: Class.Quant.Grav. 30, 199401 (2013)].

[151] J. Aasi *et al.* The NINJA-2 project: Detecting and characterizing gravitational waveforms modelled using numerical binary black hole simulations. *Class. Quant. Grav.*, 31:115004, 2014.

[152] Mark Hannam, Sascha Husa, Frank Ohme, Doreen Müller, and Bernd Brügmann. Simulations of black-hole binaries with unequal masses or

nonprecessing spins: Accuracy, physical properties, and comparison with post-Newtonian results. *Physical Review D*, 82(12):124008, December 2010.

[153] Michael Purrer, Sascha Husa, and Mark Hannam. An efficient iterative method to reduce eccentricity in numerical-relativity simulations of compact binary inspiral. *Physical Review D*, 85(12):124051, June 2012.

[154] Piotr Jaranowski and Gerhard Schäfer. Erratum: Third post-Newtonian higher order ADM Hamilton dynamics for two-body point-mass systems [Phys. Rev. D 57, 7274 (1998)]. *Physical Review D*, 63(2):029902, December 2000.

[155] T. Damour, P. Jaranowski, and G. Schafer. Dimensional regularization of the gravitational interaction of point masses. *Physics Letters B*, 513(1-2):147–155, July 2001.

[156] Thibault Damour, Piotr Jaranowski, and Gerhard Schafer. Poincare invariance in the ADM Hamiltonian approach to the general relativistic two-body problem. *Physical Review D*, 62(2):021501, July 2000.

[157] Luc Blanchet and Guillaume Faye. General relativistic dynamics of compact binaries at the third post-Newtonian order. *Physical Review D*, 63(6):062005, March 2001.

[158] Vanessa C. de Andrade, Luc Blanchet, and Guillaume Faye. Third post-Newtonian dynamics of compact binaries: Noetherian conserved quantities and equivalence between the harmonic-coordinate and ADM-Hamiltonian formalisms. *Classical and Quantum Gravity*, 18(5):753–778, March 2001.

[159] Luc Blanchet and Bala R. Iyer. Third post-Newtonian dynamics of compact binaries: equations of motion in the centre-of-mass frame. *Classical and Quantum Gravity*, 20(4):755–776, February 2003.

[160] Luc Blanchet. Gravitational-wave tails of tails. *Classical and Quantum Gravity*, 15(1):113–141, January 1998.

[161] Luc Blanchet, Bala R. Iyer, and Benoit Joguet. Gravitational waves from inspiraling compact binaries: Energy flux to third post-Newtonian order. *Physical Review D*, 65(6):064005, March 2002.

[162] Luc Blanchet, Thibault Damour, Gilles Esposito-Farèse, and Bala R. Iyer. Gravitational Radiation from Inspiralling Compact Binaries Completed at the Third Post-Newtonian Order. *Physical Review Letters*, 93(9):091101, August 2004.

[163] B. M. Barker and R. F. O'Connell. Derivation of the Equations of Motion of a Gyroscope from the Quantum Theory of Gravitation. *Physical Review D*, 2(8):1428–1435, October 1970.

[164] B. M. Barker and R. F. Oconnell. Effect of the gyro's quadrupole moment on the relativity gyroscope experiment. *Physical Review D*, 11(4):711–715, February 1975.

[165] B. M. Barker and R. F. Oconnell. The gravitational interaction: spin, rotation, and quantum effects - a review. *General Relativity and Gravitation*, 11(2):149–175, October 1979.

[166] Thibault Damour. Coalescence of two spinning black holes: An effective one-body approach. *Physical Review D*, 64(12):124013, December 2001.

[167] Eric Poisson. Gravitational waves from inspiraling compact binaries: The quadrupole-moment term. *Physical Review D*, 57(8):5287–5290, April 1998.

[168] Luc Blanchet, Alessandra Buonanno, and Guillaume Faye. Higher-order spin effects in the dynamics of compact binaries. II. Radiation field. *Physical Review D*, 74(10):104034, November 2006.

[169] Guillaume Faye, Luc Blanchet, and Alessandra Buonanno. Higher-order spin effects in the dynamics of compact binaries. I. Equations of motion. *Physical Review D*, 74(10):104033, November 2006.

[170] Thibault Damour, Piotr Jaranowski, and Gerhard Schäfer. Hamiltonian of two spinning compact bodies with next-to-leading order gravitational spin-orbit coupling. *Physical Review D*, 77(6):064032, March 2008.

[171] Alessandra Buonanno, Yanbei Chen, and Thibault Damour. Transition from inspiral to plunge in precessing binaries of spinning black holes. *Physical Review D*, 74(10):104005, November 2006.

[172] Kashif Alvi. Energy and angular momentum flow into a black hole in a binary. *Physical Review D*, 64(10):104020, November 2001.

[173] Emanuele Berti, Vitor Cardoso, and Andrei O. Starinets. TOPICAL REVIEW: Quasinormal modes of black holes and black branes. *Classical and Quantum Gravity*, 26(16):163001, August 2009.

[174] Alex Nitz, *et al.* gwastro/pycbc: Pycbc release 1.18.1, May 2021.

[175] Lucy M. Thomas, Geraint Pratten, and Patricia Schmidt. Accelerating multimodal gravitational waveforms from precessing compact binaries with artificial neural networks. *Physical Review D*, 106(10):104029, November 2022.